JUSTUS-LIEBIG-UNIVERSITÄT GIESSEN Philipps Universität Marburg THM TECHNISCHE HOCHSCHULE MITTELHESSEN

FORSCHUNGSCAMPUS MITTELHESSEN

Development of a New Primary Standard for the Dose Measurement Quantity Air Kerma in X-ray Diagnostics

Dissertation

Zur

Erlangung des akademischen Grades der Doktorin der Ingenieurwissenschaften (Dr.-Ing.)

Dem Promotionszentrum für Ingenieurwissenschaften

am Forschungscampus Mittelhessen

vorgelegt von

Jessica Gschweng

M. Sc.

Aus Bietigheim-Bissingen

Braunschweig, 24.02.2026

Begutachtung durch:

Prof. Dr. Klemens Zink und Prof. Dr. Christoph Bert

Abstract

Mammography is the main screening modality for the early detection of breast cancer. However, the use of ionizing x-ray radiation may also increase the risk of cancer. This highlights the importance of quality assurance of mammography devices. In acceptance and constancy tests diagnostic dosimeters are used to measure air kerma, a quantity describing the kinetic energy transferred from indirect ionizing radiation to charged particles in air. To ensure reliable and traceable measurements, these dosimeters must be calibrated regularly. The Physikalisch-Technische Bundesanstalt (PTB), the national metrology institute of Germany, realizes the unit gray for the quantity air kerma using free-air ionization chambers (FACs) as primary standards. Due to the increasing demand for calibrations with a primary standard in the x-ray energy range below 50 keV, as used in mammography, a new air kerma primary standard, called MAKS (Mammography Air Kerma Standard), was developed within the scope of this work.

The objective of this work was the development a FAC for low-energy x-rays. Monte Carlo and finite element method (FEM) simulations were systematically employed to optimize the FAC geometry with the aim of minimizing required correction factors and reducing associated uncertainties. Based on these simulations, engineering tolerances for individual components were derived. MAKS was subsequently manufactured at PTB using high-precision, state-of-the-art techniques. In the following MAKS was characterized. Monte Carlo simulations were used to determine correction factors for diaphragm effects k_{dia}, photon scattering k_{sc}, radial electron losses k_{eloss}, and inadequate charged particle equilibrium k_{cpe}. FEM simulations were applied to determine the collecting length and collecting volume, as well as the correction factor for electric field distortion k_{d}. The default polarizing voltage and correction factors for ion recombination k_{s}, polarity effects k_{pol}, and photon attenuation in air k_{att} were determined experimentally. An uncertainty budget for air kerma measurements with MAKS was established. Finally, MAKS was compared with the existing PTB primary standard PK100, developed in the 1950s.

The correction factors required for MAKS are closer to unity than those of the PK100. In particular, shortening the air path length between the reference plane at the diaphragm and the center of the collecting volume reduced the air attenuation correction, which is especially significant at low x-ray energies, by approximately 40 %. This design choice, however, introduces challenges due to electric field distortion and an increased contribution to the air kerma from particles produced by interactions with the diaphragm. Both effects were successfully reduced by optimizing the FAC geometry, resulting in correction factors k_{d} and k_{dia} close to unity. High precision manufacturing has reduced the combined standard uncertainty of air kerma measurements from 0.52 % for the PK100 to 0.38 % for MAKS.

Despite successful characterization, a comparison between MAKS and PK100 revealed a systematic and significant deviation of approximately 1.4 % in the determined air kerma. Extensive investigations did not identify any systematic error in the measurements with MAKS. Consequently, further work is required prior to establishing MAKS as an air kerma primary standard. This includes long-term stability studies, reproduction of the most critical component – the collecting electrode, international comparisons with other established primary standards, and a re-evaluation of the collecting length and correction factors of the PK100. The latter is expected to be limited by incomplete historical documentation on the PK100. Nevertheless, the results of this work contribute valuable insights into the realization of air kerma for low-energy x-rays using FACs and support the further advancement of primary dosimetry in diagnostic radiology.

Zusammenfassung

Die Mammographie ist das wichtigste Screening-Verfahren zur Früherkennung von Brustkrebs. Allerdings kann die Verwendung ionisierender Röntgenstrahlung auch das Krebsrisiko erhöhen, was die Bedeutung der Qualitätssicherung von Mammographiegeräten unterstreicht. Im Rahmen von Abnahme- und Konstanzprüfungen werden Diagnostikdosimeter zur Messung der Luftkerma eingesetzt, also der durch indirekt ionisierende Strahlung auf geladene Teilchen in Luft übertragenen kinetischen Energie. Für zuverlässige und rückführbare Messergebnisse müssen Diagnostikdosimeter regelmäßig kalibriert werden. Deutschlands nationales Metrologieinsitut, die Physikalisch-Technische Bundesanstalt (PTB), stellt die Einheit Gray der Luftkerma mithilfe von Freiluft-Ionisationskammern (FACs) dar. Aufgrund des steigenden Bedarfs an Kalibrierungen im Röntgenenergiebereich unter 50 keV, wie in der Mammographie verwendet, wurde im Rahmen dieser Arbeit ein neues Luftkerma-Primärnormal, genannt MAKS (engl. Mammography Air Kerma Standard), entwickelt.

Ziel dieser Arbeit war die Entwicklung und systematische Optimierung der Geometrie einer FAC für niederenergetische Röntgenstrahlung. Monte-Carlo-Simulationen und Simulationen auf Basis der Finite-Elemente-Methode (FEM) wurden eingesetzt, um erforderliche Korrektionsfaktoren sowie deren Unsicherheiten zu minimieren und Fertigungstoleranzen festzulegen. MAKS wurde an der PTB hochpräzise gefertigt und anschließend charakterisiert. Mittels Monte-Carlo-Simulationen wurden Korrektionsfaktoren für Blendeneffekte k_{dia}, Photonenstreuung k_{sc}, radiale Elektronenverluste k_{eloss} und unzureichendes Sekundärelektronengleichgewicht k_{cpe} ermittelt. Zur Bestimmung der Sammellänge und des Korrektionsfaktors der elektrischen Feldverzerrung k_{d} wurden FEM-Simulationen durchgeführt. Die Standardpolarisationsspannung und die Korrektionsfaktoren für Ionenrekombination k_{s}, Polaritätseffekte k_{pol} und Photonenschwächung in Luft k_{att} wurden experimentell bestimmt. Außerdem wurde in Unsicherheitsbudget für Luftkerma-Messungen mit MAKS erstellt. Abschließend erfolgte ein Vergleich von MAKS mit dem bisherigen PTB-Primärnormal PK100 aus den 1950er-Jahren.

Die erforderlichen Korrektionsfaktoren für MAKS sind insgesamt näher bei 1 als die der PK100. Insbesondere die Verkürzung der Länge des Luftwegs zwischen der Referenzebene der Blende und der Mitte des Messvolumen reduzierte die Luftschwächungskorrektion um etwa 40 %, was besonders bei niedrigen Röntgenenergien von Bedeutung ist. Eine verkürzte Luftweglänge erhöht jedoch die Verzerrung des elektrischen Feldes und den Beitrag zur Luftkerma von Teilchen, die durch Wechselwirkungen mit der Blende entstehen. Beide Effekte konnten durch eine gezielte Optimierung der FAC-Geometrie erfolgreich minimiert werden, sodass die entsprechenden Korrektionsfaktoren für die elektrische Feldverzerrung k_{d} und die Blendeneffekte k_{dia} nahe bei 1 liegen. Durch die hochpräzise Fertigung von MAKS konnte die kombinierte Standardunsicherheit der Luftkerma-Messungen im Vergleich zur PK100 von 0,52 % auf 0,38 % reduziert werden.

Trotz erfolgreicher Charakterisierung zeigte ein Vergleich zwischen MAKS und der PK100 eine systematische und signifikante Abweichung von etwa 1,4 % in der bestimmten Luftkerma. In umfangreichen Untersuchungen konnte kein systematischer Fehler in den Messungen mit MAKS identifiziert werden. Vor der Etablierung von MAKS als neues Primärnormal sind daher weitere Arbeiten erforderlich. Diese umfassen insbesondere Langzeitstabilitätsstudien, die Reproduktion der kritischsten Komponente – der Messelektrode –, internationale Vergleiche mit weiteren etablierten Primärnormalen sowie eine Neuberechnung der Sammellänge und der Korrektionsfaktoren der PK100. Dennoch bietet diese Arbeit wertvolle Einblicke in die Realisierung der Luftkerma für niederenergetische Röntgenstrahlung mithilfe von Freiluft-Ionisationskammern und leistet einen Beitrag zur Weiterentwicklung der Primärdosimetrie in der Röntgendiagnostik.

Table of Contents

1 Introduction 1

1.1 Theoretical Background 1

1.1.1 Air Kerma 1

1.1.2 Free-air Ionization Chambers 2

1.1.3 Correction Factors 3

1.2 Established Primary Standards 5

1.3 Development Process 7

2 Summary of Publications 8

2.1 Optimum Air Path Length 8

2.2 Finite-element Modelling of the Electric Field 9

2.3 Diaphragm Design 10

3 Commissioning of the New Primary Standard 11

3.1 Characterization and Comparison: Materials and Methods 11

3.1.1 MAKS 11

3.1.2 Monte Carlo and FEM Simulations 12

3.1.3 Measurement Setup 14

3.1.4 Uncertainty Estimation 16

3.2 Characterization and Comparison: Results 18

3.3 Characterization and Comparison: Discussion 20

3.3.1 Assessment of Potential General Systematic Errors 20

3.3.2 Assessment of Potential Systematic Errors in Correction Factors 21

3.3.3 Assessment of Potential Systematic Errors in the Collecting Volume 23

4 Discussion 27

5 Conclusion 30

References i

Appendix iv

1 Introduction

Mammography is an important screening test for the early detection of breast cancer. With regular imaging, breast tumors can be detected and treated at an early stage [1]. However, at the same time, the x-ray radiation used in mammography may itself increase the risk of cancer [2]. This highlights the importance of thorough quality assurance of the mammography equipment used. Acceptance and constancy testing are essential to limit radiation exposure for the patient while ensuring image quality.

As part of acceptance and consistency tests, diagnostic dosimeters are used to measure the air kerma. The air kerma is the fundamental quantity in dosimetry for x-ray diagnostics. It describes the kinetic energy transferred during the interaction of indirect ionizing radiation with air. Many operational and application-related dose quantities are derived from the air kerma. In radiation protection dosimetry, these include quantities such as the ambient dose equivalent or the personal dose equivalent. In medical diagnostics, examples include the air kerma area product and air kerma length product, used in radiography and computed tomography, and the mean glandular dose, used in mammography.

To ensure reliable measurement results, diagnostic dosimeters must be calibrated regularly. This calibration is part of an unbroken chain of calibrations, which ensures that the measurement results of a diagnostic dosimeter are traceable to a reference. Metrological traceability ensures that measurement results from different devices, laboratories and times are comparable. A primary standard is the highest level of metrological reference. It directly measures the physical quantity, in this case the air kerma, based on fundamental physical laws. Primary standards are highly accurate, but rare. In practice, secondary standards are calibrated against a primary standard in specialized calibration laboratories. These secondary standards are used to calibrate diagnostic dosimeters. Each step in this chain - from the primary standard to the secondary standard to the diagnostic dosimeter – contributes additional measurement uncertainty. This highlights that the uncertainty of air kerma measurements with the primary standard should be as low as possible.

The Physikalisch-Technische Bundesanstalt (PTB) is Germany's national metrology institute. It is responsible for the realization and dissemination of the unit gray for the dose quantity air kerma and operates primary standards for this purpose. In recent years, the demand for calibrations using an air kerma primary standard for x-rays with energies below 50 keV, the energy range used in mammography, has increased significantly. This increase is due to the growing variety of anode and filter combinations used in modern mammography devices. In response to this need, the present work aims to develop a new air kerma primary standard for low-energy x-rays.

1.1 Theoretical Background

PTB employes free-air ionization chambers (FACs) as primary standards to realize the unit of the air kerma free-in-air. The interaction of x-rays with the air inside the FAC produces ions, which are collected and measured as charge. The air kerma can be calculated from the measured ionization charge by applying various correction factors.

1.1.1 Air Kerma

Kerma (kinetic energy released per unit mass) is defined in ICRU Report 90 [3]. The air kerma K_{air} results from the mean sum of the initial kinetic energy of charged particles $\mathrm{d}E_{\mathrm{tr}}$ liberated by uncharged particles in an air mass $\mathrm{d}m_{\mathrm{air}}$ and is given by

$$K_{\mathrm{air}} = \frac{\mathrm{d}E_{\mathrm{tr}}}{\mathrm{d}m_{\mathrm{air}}}. \tag{1}$$

The unit of the air kerma is given in J/kg or in gray (Gy). For a fluence of uncharged particles ϕ with an energy E, the air kerma K_{air} results from the mass energy transfer coefficient for air $\frac{\mu_{\mathrm{tr}}}{\rho_{\mathrm{air}}}$, thus

$$K_{\mathrm{air}} = \phi E \frac{\mu_{\mathrm{tr}}}{\rho_{\mathrm{air}}}. \tag{2}$$

A fraction g_{air} of the kinetic energy of the charged particles is lost through radiation processes such as bremsstrahlung, annihilation and fluorescence radiation. The collision air kerma $K_{\mathrm{col,air}}$ excludes these radiation losses:

$$K_{\mathrm{col,air}} = \phi E \frac{\mu_{\mathrm{en}}}{\rho_{\mathrm{air}}} = \phi E \frac{\mu_{\mathrm{tr}}}{\rho_{\mathrm{air}}}(1 - g_{\mathrm{air}}) = K_{\mathrm{air}}(1 - g_{\mathrm{air}}). \tag{3}$$

Exposure X describes the mean charge of the ions $\mathrm{d}q$, which are generated by the charged particles liberated in a mass $\mathrm{d}m_{\mathrm{air}}$ of dry air and is a measurable quantity. The correlation between exposure X and the collision air kerma $K_{\mathrm{col,air}}$ is given by

$$X = \frac{\mathrm{d}q}{\mathrm{d}m_{\mathrm{air}}} \approx \frac{e}{W_{\mathrm{air}}} K_{\mathrm{col,air}}, \tag{4}$$

where e is the elementary charge and W_{air} is the mean energy expended to generate an ion pair in dry air. Equation (4) represents an approximate equality because the exposure X accounts for the total charge from electrons or ions released by incident photons, while W_{air} considers only the charge generated as these electrons slow down. At lower photon energies, the difference between these quantities becomes significant and must be corrected, as described later. According to ICRU Report 90 [3], the recommended value for W_{air} is 33.97 eV, with a relative standard uncertainty of 0.35 %.

Equation (4) shows that air kerma can be derived from a measurement of exposure. The definition of exposure requires measuring the total charge liberated by photons in a known mass of air, which is difficult to achieve in practice. A free-air ionization chamber (FAC) therefore measures an equivalent charge under conditions of charged-particle equilibrium. Charged-particle equilibrium means that the number of charged particles entering a volume of air equals the number leaving it.

1.1.2 Free-air Ionization Chambers

The most commonly used type of FAC is the parallel-plate FAC [4], as shown in Figure 1. This FAC consists of a shielding housing and an entrance diaphragm made of a highly attenuating material, such as tungsten. Inside the FAC there are two parallel electrodes: a high-voltage electrode and a ground electrode. A high voltage is applied so that an electric field is created between the electrodes. The ground electrode consists of the collecting electrode and the guard electrode surrounding it. To generate a uniform electric field between the two electrodes, an additional guard system is required. This is usually realized with a system of guard rings or wires, positioned between the electrodes. An electric potential is applied to each of these guard rings or wires using a voltage divider so that the electric potential between the high-voltage and ground electrode gradually decreases.

When x-rays enter the FAC through the entrance diaphragm, the photons interact with the air inside the FAC, generating secondary electrons. These generate ion pairs through ionization, which are collected as charge. The determination of the air kerma in the reference plane at the downstream edge of the diaphragm requires the conversion of the measured ionization charge Q. Rewriting equations (3) and (4) leads to the following expression for the air kerma K_{air}:

$$K_{\mathrm{air}} = \frac{W_{\mathrm{air}}}{e}\frac{Q}{m_{\mathrm{air}}}\frac{1}{(1-\bar{g}_{\mathrm{air}})}\prod_i k_i, \tag{5}$$

where k_i are correction factors that must be applied to compensates for systematic errors arising from the FAC geometry and experimental setup conditions.

The air mass m_{air} is determined from the collecting volume V of the air density ρ_{air}. The collecting volume V is defined by the aperture radius r of the entrance diaphragm and the collecting length l_{col}:

$$m_{\mathrm{air}} = V\rho_{\mathrm{air}} = \pi r^2 l_{\mathrm{col}}\rho_{\mathrm{air}}. \tag{6}$$

The collecting length l_{col} is commonly calculated from the FAC geometry, using the length of the collecting electrode and half of the air gaps between the collecting and guard electrode. However, this calculation does not take the influence of the electric field into account. Therefore, the actual collecting length can differ from the nominal geometric value. A detailed description of how the collecting length is determined from the electric field inside the FAC is provided in section 3.1.2.

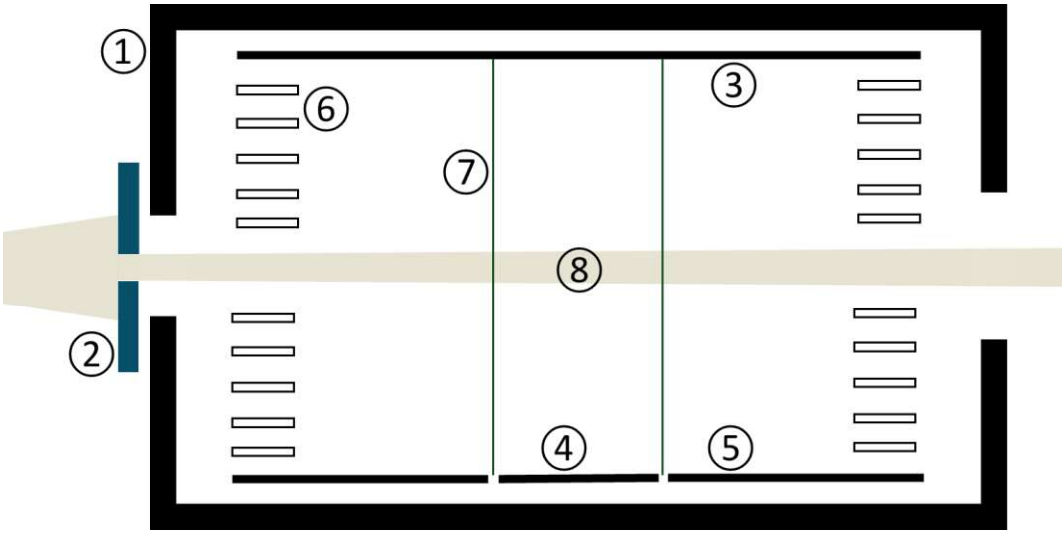

Figure 1: Schematic drawing of a free-air ionization chamber with housing ①, diaphragm ②, high-voltage electrode ③, collecting electrode ④, guard electrode ⑤, guard rings ⑥ and electric field lines ⑦ defining the collecting volume ⑧.

1.1.3 Correction Factors

The correction factor for air density k_{ρ} corrects an air kerma measurement with air pressure p and temperature T at the time of measurement to reference conditions with $p_0 = 1013.25\ \mathrm{hPa}$ and $T_0 = 293.15\ \mathrm{K}$. The correction factor k_{ρ} is given by

$$k_{\rho} = \frac{p_0 T}{p T_0}. \tag{7}$$

The humidity correction factor k_{h} is required because the air inside a FAC is humid, but the air kerma refers to dry air. Data for the humidity correction factor k_{h} is given in ICRU Report 90 [3].

The correction factor $k_{\mathrm{ii}}k_W$ is the product of the correction factors k_{ii} and k_W. The correction factor k_{ii} corrects the dose contribution of the initial ion pair that is created during the first interaction of a photon with the air inside the FAC. This is necessary because W_{air} denotes the mean energy expended by an electron during deceleration to produce an ion pair. The correction factor k_W corrects the deviation of W_{air} at low energies compared to its value at higher energies. Monoenergetic values for $k_{\mathrm{ii}}k_W$ are listed in ICRU Report 90 [3]. Monoenergetic correction factors can be converted into spectral

correction factors by averaging with the x-ray spectrum of a specific radiation quality, as described by Grimbergen et al. [5].

The polarity correction factor k_{pol} is applied if the ionization charge measured with the FAC changes when the polarity of the applied polarizing voltage is reversed. The correction factor k_{pol} can be determined by measurements at both polarities. For measurements carried out at positive polarity, k_{pol} results from the ionization currents I^+ and I^- measured at positive and negative polarity as

$$k_{\mathrm{pol}} = \frac{I^+ + I^-}{2I^+}. \tag{8}$$

The correction factor k_{s} corrects for ion recombination. This is necessary because the generated ions partially recombine, which reduces the ionization charge. A distinction is made between initial recombination and volume recombination. Initial recombination is the recombination of electron-ion-pairs immediately after their generation within the track of a single ionizing particle. It is proportional to the inverse of the applied polarizing voltage V and independent of the dose rate. Volume recombination is the recombination of electron-ion-pairs during the drift to the electrodes. It is proportional to $\frac{1}{V^2}$ and dependent on the dose rate, as the volume recombination increases with the concentration of ions. The determination of k_{s} is based on the method introduced by Niatel [6] and the calculation according to De Almeida and Niatel [7] and Boutillon [8]. The following equation applies for k_{s}:

$$k_{\mathrm{s}} = \frac{I_{\mathrm{S}}}{I_{\mathrm{V}}} = 1 + \frac{p_{\mathrm{si}}}{V} + \frac{p_{\mathrm{sv}}}{V^2}, \tag{9}$$

where I_{S} is the saturation current (maximum current without recombination) and I_{V} is the measured ionization current. V is the applied polarizing voltage. p_{si} is a parameter that describes the initial recombination, and p_{sv} is a parameter that describes the volume recombination. The initial and volume recombination parameters can be determined from measurements of the ionization current at different dose rates, using two different polarizing voltages, as described in more detail in section 3.1.3.

The correction factor for air attenuation k_{att} is required to correct the photon attenuation in air between the reference plane, at the downstream edge of the diaphragm of the FAC, and the middle of the collecting volume. This distance is called the air path length (APL) of the FAC. For a given APL, k_{att} can be calculated from the attenuation coefficient in air $\mu_{\mathrm{air}}(E)$ for a photon energy E as follows

$$k_{\mathrm{att}} = e^{\mu_{\mathrm{air}}(E)APL}. \tag{10}$$

For a given photon fluence spectrum of a specific radiation quality, k_{att} is calculated from the fluence-weighted mean attenuation coefficient:

$$k_{\mathrm{att}} = e^{\overline{\mu_{\mathrm{air}}}APL}. \tag{11}$$

To calculate k_{att} according to equation (11), the photon fluence spectra must be known. PTB measures the x-ray spectra with spectrometry as described by Ketelhut et al [9]. Due to the potentially large uncertainties in k_{att} arising from uncertainties in the x-ray spectra and in the attenuation coefficients at low energies, it may be preferable to determine k_{att} experimentally rather than by calculation. Different possibilities for the experimental determination of k_{att} are described by Burns and Büermann [4]. At PTB, k_{att} is determined experimentally by the displacement method, as explained in section 3.1.3. The use of Monte Carlo simulations of radiation transport is another option for determining k_{att}. However, this method is also limited at low energies by the uncertainties of the x-ray spectra and the attenuation coefficients. Although the air path length is defined geometrically, the effective air path

length depends on the air density at the time of a measurement. Therefore, $k_{\mathrm{att,ref}}$, determined for reference conditions, must be converted to $k_{\mathrm{att,meas}}$ for the measurement conditions using the air density correction factor k_{ρ} (see equation (7)):

$$k_{\mathrm{att,meas}} = k_{\mathrm{att,ref}}^{\frac{1}{k_{\rho}}}. \tag{12}$$

The correction factor for diaphragm effects k_{dia} corrects dose contributions of particles that interact with the diaphragm or are created by interactions with the diaphragm. This correction is necessary because, by definition, air kerma accounts only for the kinetic energies of the initial secondary electrons produced in the air at the reference plane. Interactions of photons with the diaphragm produce secondary particles, which are not considered part of the air kerma. Their dose contributions must therefore be corrected. The interactions that are included in the correction factor k_{dia} are transmission through the diaphragm, scattering with the diaphragm and emission of fluorescence photons. Monte Carlo simulations are used to determine k_{dia}.

Another correction factor that is required to correct the dose contributions of unwanted secondary particles is the scattering correction factor k_{sc}. This corrects the dose contributions of photons scattered in air. Fluorescence photons, which are produced during the interaction of photons with the air inside the FAC, are also secondary particles that are not part of the air kerma. Their dose contribution is also considered in the correction factor k_{sc}. The correction factor k_{sc} is determined by the use of Monte Carlo simulations.

The correction factors k_{eloss} and k_{cpe} can also be determined using Monte Carlo simulations. The correction factor k_{eloss} corrects electron losses in the radial direction (perpendicular to the beam axis). This correction is required when secondary electrons reach the electrodes without having fully lost their energy through ionization. The correction factor for the lack of charged particle equilibrium k_{cpe} corrects the electron loss in the axial direction (along the beam axis). This correction becomes necessary if the distance between the reference plane and the collecting volume is too small to ensure that the number of secondary electrons entering the collecting volume equals those leaving it.

The correction factor for electric field distortion k_{d} considers that the electric field inside the FAC is not completely uniform despite the guard electrode and the guard ring or guard wire system. Although the nominal collecting length is defined geometrical by the length of the collecting electrode, the effective collecting length is determined by the electric field lines ending at the collecting electrode. If the electric field lines are deformed, for example by curving outwards, the collecting volume is altered. This effect can be quantified using finite element method (FEM) simulations and expressed as the correction factor k_{d}.

1.2 Established Primary Standards

National metrology institutes operate FACs as air kerma primary standards in the x-ray energy range up to 50 keV. These primary standards were compared with each other as part of the international key comparison BIPM.RI(I)-K2 [10–25]. It is noteworthy that the FACs employed exhibit considerable variation in their geometric design. Consequently, the required correction factors also vary, as most of these corrections are explicitly dependent on the FAC geometry. Against this background, a fundamental question arises: is there a FAC geometry in which the correction factors are as close as possible to unity? This would potentially reduce sources of error and large measurement uncertainties.

PTB currently operates three FACs as air kerma primary standards, each used in different x-ray energy ranges [26]. The PK100, developed in the 1950s, is designed as a parallel plate chamber. The air path

length of the PK100 is 97.2 mm and the electrode separation is 234 mm. The ground electrode has 6 collecting electrodes. Various diaphragms with apertures diameters between 6 mm and 20 mm can be used. A polarizing voltage of 6000 V is applied to the high-voltage electrode. To uniform the electric field, the PK100 uses a guard wire system consisting of 77 graphitized nylon threads, connected via the resistors of a voltage divider. The PK100 is used for calibrations for x-ray energies up to 100 keV. PK100 is not specifically optimized for operation in the lower energy x-ray range up to 50 keV. Table 1 shows the correction factors and associated uncertainties for the PK100 for the CCRI reference radiation qualities used for BIPM.RI(I)-K2 key comparison. Including the uncertainty of the collecting volume (0.06 %), the measured ionization charge (0.03 %), the positioning of the FAC (0.01 %), the correction factor k_{ρ} (0.03 %) and the uncertainty of W_{air} (0.35 %) the combined standard uncertainty of air kerma measurements with the PK100 is 0.52 %.

Table 1: Correction factors and uncertainties for the PK100 (first collecting electrode) [16].

	CCRI 10 kV	CCRI 30 kV	CCRI 25 kV	CCRI 50 kVb	CCRI 50 kVa	*u* [%]
Humidity k_{h}	0.9980	0.9980	0.9980	0.9980	0.9980	0.03
Initial ionization and energy dependence of W_{air} $k_{\mathrm{ii}}k_W$	0.9953	0.9964	0.9967	0.9977	0.9980	0.11
Polarity k_{pol}	1.0000	1.0000	1.0000	1.0000	1.0000	0.07
Ion recombination k_{s}	$k_{\mathrm{s}} = 1.0005 * (1 + 2.86 * 10^{7} \frac{1}{A} I_{\mathrm{V}})$ (13)					0.11
Air attenuation k_{att}[a]	1.2294	1.0468	1.0321	1.0090	1.0047	0.21
Diaphragm effects k_{dia}	0.9999	0.9993	0.9990	0.9974	0.9964	0.07
Scattering k_{sc}	0.9852	0.9889	0.9900	0.9929	0.9939	0.05
Electron loss k_{eloss}	1.0000	1.0000	1.0000	1.0000	1.0000	0.05
Guard wire attenuation k_{ap}	1.0341	1.0084	1.0059	1.0014	1.0007	0.21
Field distortion k_{d}	0.9910	0.9910	0.9910	0.9910	0.9910	0.10
$1 - \bar{g}_{\mathrm{air}}$	0.9997	0.9997	0.9997	0.9997	0.9997	0.01

[a] related to reference temperature and air pressure

Due to the stronger attenuation of low-energy photons, the air attenuation and guard wire attenuation corrections are comparatively large. For PTB's new air kerma primary standard, which is specifically designed for the energy range up to 50 keV, these corrections should be minimized. To reduce the air attenuation, the air path length of the FAC must be shortened. The guard wire attenuation can be eliminated if a guard ring system is used to uniform the electric field instead of the guard wire system. However, both of these changes also affect other correction factors, so that optimizing the FAC geometry represents a trade-off between competing objectives.

The aim of this work is to apply a systematic methodology to determine the geometry dependence of the correction factors as early as the design phase of a new FAC. By investigating the relationships between geometric parameters and the individual correction factors in detail, these factors can be specifically weighed against each other to identify an overall optimal geometry. A geometry is considered optimal if all correction factors are as close to unity as possible while simultaneously exhibiting the lowest possible uncertainties. Defining appropriate engineering tolerances is particularly important for the uncertainty analysis.

1.3 Development Process

The development process of the new PTB air kerma primary standard presented in this work followed a multi-stage approach that considered both the physical requirements and the practical conditions of use. The starting point was the analysis of established primary standards from various metrology institutes and the identification of their advantages and limitations. In particular, the PK100, the currently used primary standard for low-energy x-rays of PTB from the 1950s, as well as the primary standards of the Czech Metrology Institute (CMI) and the Bureau International des Poids et Measures (BIPM) from the 2010s were examined. On this basis, a first functional and technical preliminary design of the new PTB primary standard was created: a parallel plate FAC specialized for low-energy x-rays as used in mammography, hereafter called MAKS (Mammography Air Kerma Standard).

The next step was to specify the dimensions of MAKS. The aim was to optimize the geometry of MAKS so that the correction factors for the determination of the air kerma for the specific application range of x-ray energies below 50 keV are as close as possible to 1. The main focus was on the optimization of the air path length of MAKS (as described in *Optimum Air Path Length* [27]), but also the collecting electrode length, the electrode separation, the housing and the diaphragm geometry (as described in *Diaphragm Design* [28] were optimized. The optimal dimensions of MAKS were determined using Monte Carlo simulations in EGSnrc [29]. In systematic simulation studies, the geometry of MAKS was varied with respect to different components, and the resulting effects on the correction factors k_{dia}, k_{sc}, k_{eloss}, k_{cpe} and k_{att} were investigated.

To optimize the geometry of MAKS with regard to the correction factor for the electric field distortion k_{d}, which does not depend on the interactions of the radiation, additional FEM simulations were carried out in COMSOL Multiphysics® 6.1 [30]. Here, all components affecting the electric field were systematically varied to evaluate their influence on k_{d}, thereby enabling the identification of an optimal design (as described in *Finite-element Modelling of the Electric Field* [31]).

The systematic approach applied in both the MC and FEM simulations enabled the derivation of engineering tolerances for various components of MAKS.

An initial design was then created in Solidworks, a 3D CAD software. In cooperation with PTB's department for *Scientific Instrumentation*, the initial draft was refined into a comprehensive technical design. In addition to the physically relevant components, the design also included practical elements such as a stand with rotary and sliding tables, various components required for positioning and aligning MAKS, and a 3D-printed housing with handles and brackets for a temperature sensor.

MAKS was manufactured with highest precision in PTB's *Manufacturing Department* in full compliance with all specified engineering tolerances, including micrometer-level tolerances for the most critical components. Several individual components were produced externally when the requirements exceeded the capabilities of in-house manufacturing.

After production, MAKS was characterized. In the first step, the geometry of MAKS was measured with high accuracy. The models of MAKS used in the MC and FEM simulations were then adapted using the measured dimensions and the correction factors k_{dia}, k_{sc}, k_{eloss}, k_{cpe} and k_{d} were determined. Initial measurements with MAKS were carried out to verify the measurement setup, to assess the plausibility and reproducibility of the measured ionization charge, and to ensure that there was no wall transmission of the radiation. The chamber voltage of MAKS and the correction factors k_{att}, k_{s} and k_{pol} were subsequently determined experimentally. The characterization of MAKS also included the preparation of an uncertainty budget. Following the successful characterization, a comparison was made with an existing PTB primary standard, the PK100.

2 Summary of Publications

Each publication produced as part of this work answers a question which arose during the development of the new PTB air kerma primary standard. They all pursue the goal of optimizing the geometry of the FAC with regard to the specialization of the new primary standard to the x-ray energy range below 50 keV, as used in mammography. In this context, optimization means minimizing the necessary corrections and their uncertainties.

The publication on the *Optimum Air Path Length* [27] describes how the correction for photon attenuation in air, expressed by the correction factor k_{att}, is minimized. This is necessary because air attenuation is the largest correction required at low-energy x-rays. In addition, this publication shows the limitations of averaging monoenergetic correction factors with an x-ray spectrum, which allows a better estimation of the uncertainties of the spectral correction factors.

To minimize the air attenuation, the air path length of the FAC must be shortened. However, this results in a shorter guard electrode, which has a negative effect on the uniformity of the electric field within the FAC. The publication on the *Finite-element Modelling of the Electric Field* [31] therefore describes how the electric field can be analyzed using FEM simulations and how the geometry must be adapted in order to achieve a minimum correction of the electric field distortion, expressed by the correction factor k_{d}. Furthermore, this publication presents a method for quantitatively determining the uncertainty of k_{d} from the engineering tolerances using FEM, thus offering the possibility of minimizing it.

Shortening of the air path length also means that more particles resulting from interactions of the x-rays with the diaphragm reach the collecting volume and contribute to the ionization charge. This corresponds to an increase in the required correction for diaphragm effects, expressed by the correction factor k_{dia}. To address this, the publication on the *Diaphragm Design* [28] describes how the diaphragm geometry can be optimized to minimize this correction. Simplifying the diaphragm geometry also facilitates manufacturing and may consequently reduce the uncertainty of k_{dia}.

The author of this dissertation, Jessica Gschweng, conducted the majority of the work presented in the publications independently. This includes the development and conceptualization of the research projects, methodological commissioning, data collection, evaluation, analysis, and interpretation of the results, as well as the preparation and revision of the manuscripts. The formulation of research questions and interpretation of results were discussed with the co-author, Stefan Pojtinger, throughout the process. The co-author also provided suggestions for structuring the manuscripts and provided editorial feedback. An AI-based PTB-internal language tool for translation based on DeepL was used for linguistic refinement to improve grammar and clarity.

2.1 Optimum Air Path Length

The publication entitled “Free-air ionization chambers for the measurement of air kerma in low-energy x-rays—optimum air path length and the limitations of averaging monoenergetic correction factors” (DOI: 10.1088/1681-7575/adc39d) by Jessica Gschweng and Stefan Pojtinger [27] was published in April 2025 in the journal Metrologia.

This publication addresses the two main difficulties encountered when specializing an air kerma primary standard to x-ray energies below 50 keV, as used in mammography. The first difficulty is that the photon attenuation between the reference plane and the collecting volume is pronounced at low x-ray energies. The second difficulty is that mammography devices from different manufacturers have a wide variety of anode material and filter combinations, leading to a wide range of radiation qualities.

This requires a method to determine spectral correction factors for different radiation qualities without time-consuming measurements. The objectives of this work were therefore to determine the optimum air path length of PTB's new air kerma primary standard for minimizing photon attenuation in air and to evaluate the limits of the method of averaging monoenergetic correction factors with an x-ray spectrum. These tasks were accomplished with the aid of Monte Carlo simulations.

The results of this work showed that the air attenuation correction for FACs without an optimized air path length (APL is often e.g. 100 mm) of other NMIs is up to 20 % or more for a 10 kV x-ray spectrum. By minimizing the air path length, a reduction to 10 % or less is possible. However, minimization is limited to 45 mm because of the secondary electron equilibrium that must be maintained and because of the electrons that are generated by interactions with the diaphragm may reach the collecting volume. Furthermore, this work confirmed that the method of averaging monoenergetic correction factors with an x-ray spectrum is efficient, and time-saving compared to complex measurements or simulations. However, this method can lead to significant errors if an inappropriate spectrum is used for averaging. For the averaging method, the x-ray spectrum in the collecting volume must be known. This differs from the x-ray spectrum at the reference plane as determined by spectrometry. The change in the x-ray spectra is caused primarily by attenuation, but also by scattering. The smaller the required corrections between the reference plane and the collecting volume, the smaller the change in the x-ray spectrum, the more robust the averaging method.

Overall, the results of this work clearly demonstrate the importance of keeping the correction factors close to 1 to avoid potential errors and large uncertainties, and how Monte Carlo simulations can be used to determine a suitable FAC design that achieves this.

2.2 Finite-element Modelling of the Electric Field

The publication entitled “Development of the new PTB air kerma primary standard—optimization of the geometry for minimal electric field distortions and assessment of the associated uncertainties using the finite element method” (DOI: 10.1088/1681-7575/ae033e) by Jessica Gschweng and Stefan Pojtinger [31] was published in September 2025 in the journal Metrologia.

This publication addresses the investigation of the electric field within a FAC used as a primary air kerma standard. As discussed in the study on the *Optimum Air Path Length* [27], minimizing photon attenuation in air for a FAC designed for low-energy x-rays requires shortening the air path length. However, this also shortens the guard electrode, which negatively affects the uniformity of the electric field. Moreover, no systematic method has yet been presented for quantitatively determining the uncertainty of the electric field distortion correction factor k_{d}. Typically, the uncertainty of k_{d} is estimated conservatively, for example as 0.1 % for the PK100. The aim of this work was to determine how to achieve the most uniform electric field within the FAC. FEM simulations were employed for this analysis. Furthermore, FEM simulations were used to assess the influence of engineering tolerances on the correction factor k_{d}, in order to derive its associated uncertainty.

The results of this work demonstrated that the assumption that the electric field distortion is minimal when half the polarizing voltage is applied to the housing does not generally hold. Instead, the correction factor k_{d} can be approached to 1 through geometric adjustments of the FAC. However, it should be noted that such adjustments may also affect other correction factors. In addition, the study identified specific FAC components that have a significant influence on the uncertainty of k_{d}. Engineering tolerances were specified for these components, and the uncertainty of k_{d} was quantified as 0.04 %.

Overall, this publication shows how FEM simulations can be used to design the FAC geometry to minimize electric field distortion and to quantify the uncertainty of k_{d} based on engineering tolerances.

2.3 Diaphragm Design

The publication entitled "Optimal geometric design of the diaphragm of a free-air ionization chamber for low-energy x-rays" (DOI: 10.37392/RAPPROC.2025.04) by Jessica Gschweng and Stefan Pojtinger [28] was published in January 2026 in the peer-reviewed RAP conference proceeding.

The established primary standards of various metrology institutes use different diaphragm geometries. This publication addresses the influence of the diaphragm geometry on the correction factor for diaphragm effects k_{dia}. As discussed in the study on the *Optimum Air Path Length* [27], minimizing photon attenuation in air for a FAC designed for low-energy x-rays requires shortening the air path length. However, reducing the distance between the diaphragm and the collecting volume increases the number of particles produced by interactions with the diaphragm that reach the collecting volume and thus contribute to the measured ionization charge. The aim of this work was to optimize the diaphragm thickness and the aperture shape so that the required correction of diaphragm effects is minimized. The investigation of the relationship between the diaphragm geometry and k_{dia} was carried out using Monte Carlo simulations.

The results of this work show that the diaphragm must be thick enough to prevent transmission of radiation through the diaphragm body. However, the diaphragm must be as thin as possible, as a larger thickness increases the surface of the aperture and thus leads to more scattering at the diaphragm. In addition, the work shows that the use of a complex conical aperture is not significantly advantageous but involves increased manufacturing effort.

Overall, this publication shows that a 1 mm thin diaphragm with a cylindrical aperture should be used for a low-energy air kerma primary standard. The simplicity of the geometry leads to a correspondingly simple manufacturing process, which reduces uncertainty.

3 Commissioning of the New Primary Standard

The commissioning of the new FAC, called MAKS, is the last step of this work before the new PTB air kerma primary standard can be introduced. The commissioning first includes the characterization. This includes the precise measurement of the geometry of MAKS and the determination of the default polarization voltage, the collecting volume, the correction factors and associated uncertainties. This is followed by a comparison with an existing primary standard, the PTB's PK100 (described in section 1.2).

3.1 Characterization and Comparison: Materials and Methods

The determination of the correction factors and the comparison with the PK100 was carried out for the CCRI reference radiation qualities for a tungsten anode x-ray tube as used in the key comparison BIPM.RI(I)-K2 [32] and as shown Table 2.

Table 2: Characteristics of CCRI reference radiation qualities realized at PTB.

Radiation Quality	Tube Voltage [kV]	Filtration [mm Al]	1st HVL [mm Al]
CCRI 10 kV	10	-	0.032
CCRI 30 kV	30	0.208	0.139
CCRI 25 kV	25	0.373	0.230
CCRI 50 kVb	50	1.0	1.178
CCRI 50 kVa	50	4.0	2.353

3.1.1 MAKS

MAKS (see Figure 2) is a high-precision parallel-plate FAC. The high-voltage electrode and the ground electrode are made of aluminum and are separated by 61.9 mm. The ground electrode consists of a guard electrode and a collecting electrode. The collecting electrode is 15 mm long and 70 mm wide. There is an air gap of 1 mm between the guard electrode and the collecting electrode. The center of the collecting electrode is 60.4 mm from the reference plane at the downstream edge of the diaphragm. The inner surfaces of the electrodes are gold-plated to prevent oxidation of the aluminum and to ensure stable electrical conductivity over decades. Between the electrodes there are 15 aluminum guard rings. Each of these guard rings is connected to a resistor of a voltage divider, allowing a decreasing electric potential to be applied from the high-voltage electrode to the ground electrode. High-precision ceramic disks serve as spacers and isolators between the guard rings. The housing of MAKS is composed of three layers. The outer layer is a 3D-printed plastic housing equipped with handles, while the inner layer consists of a 1 mm-thick stainless-steel shell. Between these layers, a lead layer is included for radiation shielding. Its thickness is 2 mm at the front (the side facing the x-ray tube) and 1 mm elsewhere. There are openings at the front and rear of the housing for the beam entrance and exit. The diaphragm holder is located inside the housing. 1 mm thick tungsten diaphragms with apertures of 8 mm, 10 mm, 12 mm, or 15 mm diameter, can be inserted into this holder.

MAKS is mounted on a tripod, which is height-adjustable and equipped with two turntables for angular adjustments. MAKS is aligned with the beam axis using two caps with a central hole of 1.5 mm diameter. The caps are screwed onto the front and rear openings of the housing. Alignment is performed with a laser adjusted to the beam axis. The axis of MAKS is considered aligned with the beam axis when the laser passes through both holes.

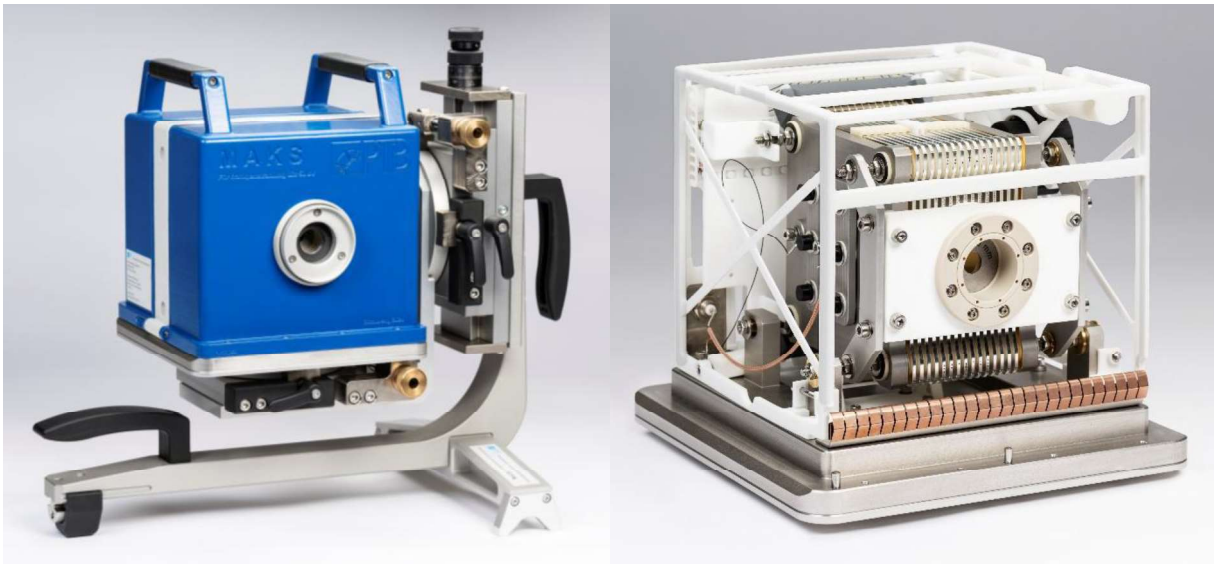

Figure 2: PTB's new free-air ionization chamber, MAKS. The left image shows MAKS mounted on a height-adjustable tripod with two turntables for angular adjustment. The right image shows the interior of MAKS, including the diaphragm in its holder, the parallel pair of electrodes and the guard rings.

3.1.2 Monte Carlo and FEM Simulations

As part of the characterization, various correction factors for MAKS were determined using Monte Carlo and FEM simulations.

The determination of k_{dia}, k_{sc}, k_{eloss} and k_{cpe} was carried out for the radiation qualities listed in Table 2 using Monte Carlo simulations. The program EGSnrc [29] was used for this purpose. With the user code egs_fac [33] these correction factors were calculated as follows

$$k_{\mathrm{dia}} = \frac{E1}{E\mathrm{g}}, \tag{14}$$

$$k_{\mathrm{sc}} = \frac{E2}{E1}, \tag{15}$$

$$k_{\mathrm{eloss}} = \frac{E3}{E2}, \tag{16}$$

$$k_{\mathrm{cpe}} = \frac{E4}{E3}. \tag{17}$$

$E\mathrm{g}$ denotes the total energy deposited in the collecting volume. $E1$ is the energy deposited in the collecting volume without any contributions from particles that have interacted with the diaphragm. $E2$ additionally excludes energy contributions that arise from the interaction of secondary photons. $E3$ corrects $E2$ for energy losses or gains through the side faces of the collecting volume and $E4$ corrects $E3$ for energy losses or gains through the front or back faces of the collecting volume.

The EGSnrc user code g [34] was used to calculate the fraction $\bar{g}_{\mathrm{air}}$ lost through radiative processes.

An EGSnrc model of MAKS was created for the Monte Carlo simulations. The radiation source used was a point source emitting photons of a specific x-ray spectrum. The x-ray spectrum was obtained from spectrometric measurements of the unfiltered x-ray spectrum [9], which was subsequently mathematically filtered according to Table 2 using PTB's in-house Python module bueSpec [35]. The Monte Carlo parameters used for the radiation transport simulations are listed in Table 3.

Table 3: Parameters applied for the Monte Carlo simulations according to [36].

Parameter	Description	Ref.
Code	EGSnrc release version 2021	[29]
Timing	PTB computing cluster (CPU) Approx. 10^7-10^8 histories per hour	
Cross-sections	mcdf-xcom	
Transport parameters	electron cutoff 0.512 MeV, photon cutoff 0.001 MeV	
Variance reduction	Photon splitting, Russian Roulette	[37]
Histories	10^{11} histories per simulation	
Statistical accuracy sought	$\leq$ 0.01 %	
Postprocessing	OriginPro 2023b	

The correction factor k_{d}, which is independent of the radiation quality, was determined using 3D FEM simulations. FEM simulations were also used to determine the collecting length. In both cases, the electrostatic interface of COMSOL Multiphysics® 6.3 [38] was used.

The geometric collecting length is defined by the collecting electrode length plus half the air gaps between the collecting and guard electrode. However, precise measurements of the geometry of MAKS have shown that the chamfers on the collecting and guard electrodes are not symmetrical. Due to this chamfer asymmetry, the geometrically determined collecting length does not correspond to the electrically relevant collecting length. This latter length must therefore be determined using FEM simulations. Specifically, the FEM simulations are used to identify the electric field lines on both sides of the collecting electrode that are farthest from the center of MAKS yet still terminate at the collecting electrode. These electric field lines define the collecting length l_{col} (see sketch in Figure 3) used to calculate the collecting volume according to equation (6).

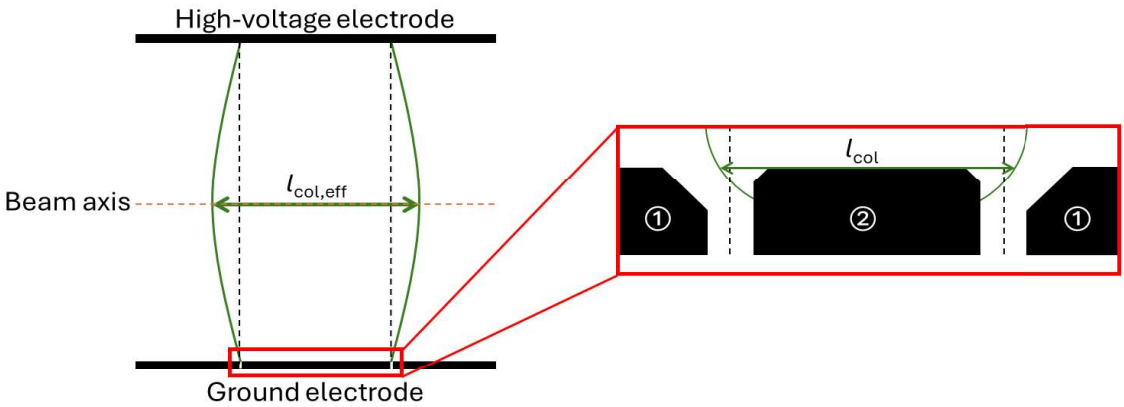

Figure 3: Schematic representation of the collecting length l_{col} at the level of the collecting ② and guard ① electrodes and of the effective collecting length $l_{col,eff}$ at the beam axis. Both are defined by the electric field lines.

The effective collecting length $l_{\mathrm{col,eff}}$ at the height of the beam axis can then be determined from the intersection points of these electric field lines with the beam axis. The correction factor for electric field distortion k_{d} is subsequently calculated as follows:

$$k_{\mathrm{d}} = \frac{l_{\mathrm{col}}}{l_{\mathrm{col,eff}}}. \tag{18}$$

3.1.3 Measurement Setup

The default polarization voltage of MAKS, as well as the correction factors k_{pol}, k_{s} and k_{att}, were determined experimentally. In addition, a comparison between MAKS and the PK100 was made. The measurement setups were adapted to the specific objectives of each experiment. Unless stated otherwise, the following conditions applied to all measurements:

- X-ray tube: Y.TU 160-D02 (Comet Yxlon), tungsten anode, inherent filtration of 0.8 mm beryllium
- Distance from source to MAKS reference point: 500 mm
- Radiation field size diameter at reference plane: 50 mm
- MAKS aperture diameter: 10 mm
- Default MAKS polarizing voltage: 2000 V
- X-ray tube currents: 4.2 mA (CCRI 10 kV), 1.4 mA (CCRI 30 kV), 4.4 mA (CCRI 25 kV), 3.5 mA (CCRI 50 kVb), 16 mA (CCRI 50 kVa)
- Radiation quality: CCRI reference radiation qualities according to Table 2
- Measurement time: 5 × 60 s, additional a self-run before and after to subtract leakage currents

The measured ionization charge was corrected to reference air density according to equation (7) and normalized to the charge measured with the monitor ionization chamber to compensate for fluctuations in the x-ray tube output.

The default polarizing voltage at which MAKS should be operated was determined experimentally. The radiation qualities CCRI 10 kV and CCRI 50 kVa and tube currents of 30 mA (CCRI 10 kV) and 45 mA (CCRI 50 kVa) were used. Voltages of 500 V, 700 V, 900 V, 1100 V, 1300 V, 1500 V, 1700 V, 1900 V, 2100 V, 2500 V and 3000 V were successively applied to MAKS, and an air density-corrected ionization charge was measured. The measurements were carried out for both polarities of the applied voltage, and the results were averaged. The averaged ionization charges were normalized to the monitor chamber signal and then plotted as a function of the applied voltage in order to determine the default MAKS polarizing voltage. This results in a saturation curve. At low voltages, incomplete charge collection due to ion recombination results in an increasing signal with increasing voltage, while at higher voltages the collected charge approaches a plateau as recombination losses become negligible. Consequently, a default polarizing voltage in the plateau region must be chosen.

The correction factor k_{pol} was determined using the radiation qualities CCRI 10 kV and CCRI 50 kVa. Measurements were carried out with MAKS for tube currents of 5 mA, 10 mA, 15 mA, 20 mA, 25 mA, 30 mA (CCRI 10 kV only), 35 mA and 45 mA (CCRI 50 kVa only) at both polarities of the applied polarizing voltage of 2000 V. For each measurement condition the determination of k_{pol} was conducted according to equation (8). k_{pol} was then calculated as the mean value from all measurements.

The correction factor k_{s} was determined using the radiation qualities CCRI 10 kV and CCRI 50 kVa. Measurements of the ionization current were carried out with MAKS at both polarities of the applied voltages V and $\frac{V}{n}$. The default polarizing voltage V was 2000 V. The factor n was chosen as 2.5 (n_1) and 2 (n_2) to reduce the voltage sufficiently to observe the effect of ion recombination. Assuming that $I_{\mathrm{V}} \approx I_S$, the following equation applies [8]:

$$\frac{I_{\mathrm{V}}}{I_{\mathrm{V/n}}} = 1 + (n-1)\frac{p_{\mathrm{si}}}{V} + (n^2-1)\frac{p_{\mathrm{sv}}}{V^2} I_{\mathrm{V}}. \tag{19}$$

To determine k_s, the ionization currents for the polarizing voltages V and $\frac{V}{n}$ were measured at tube currents of 5 mA, 10 mA, 15 mA, 20 mA, 25 mA, 30 mA (CCRI 10 kV only), 35 mA and 45 mA (CCRI 50 kVa only) and the ratio $\frac{I_V}{I_{V/n}}$ was plotted as a function of I_V for each n. By applying two linear fits, the initial and volume recombination parameters, p_{si} and p_{sv}, were derived for the cases with $n = n_1$ and $n = n_2$. The mean values of the initial and volume recombination parameters were used to determine k_s depending on I_V according to equation (9).

The correction factor k_{att} was determined using the displacement method. For this method, the diaphragm of MAKS was removed from its housing, and an external tungsten diaphragm with 5.5 mm aperture diameter was mounted in front of MAKS (see Figure 4).

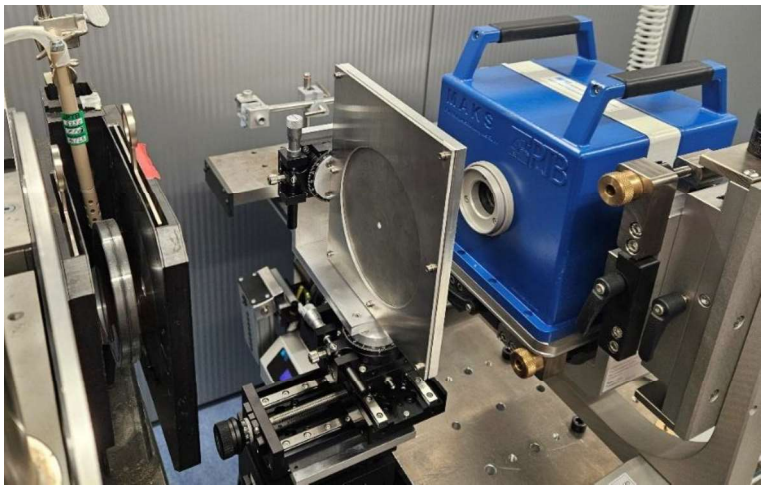

Figure 4: Experimental setup for the determination of the correction factor k_{att} using an external tungsten diaphragm mounted in front of MAKS.

This external diaphragm was placed at a distance of 350 mm from the x-ray tube. Two measurements were carried out. In one measurement, MAKS was in position z (500 mm source-MAKS-distance) along the beam axis and in the other measurement, MAKS was moved forward towards the x-ray tube to position $z - \mathrm{APL}$ (439.6 mm source-MAKS-distance). Since the distance by which MAKS was displaced corresponds to its air path length, k_{att} can be calculated directly from the quotient of the ionization currents I measured at the two positions z and $z - \mathrm{APL}$ as

$$k_{att} = \left(\frac{I_{z-\mathrm{APL}}}{I_z}\right)^{\overline{k_\rho}}. \tag{20}$$

k_{att} depends on the air path length, which is defined geometrically. However, the effective air path length and the effective distance by which MAKS is displaced in the method described above depend on the air density during the measurement. To obtain k_{att} for the reference air density, an air density correction using the air density correction factor $\overline{k}_\rho$ must be applied in equation (20). Since equation (20) is based on two measurements performed at different times, $\overline{k}_\rho$ is calculated as the mean value of the two measurements. The described measurement procedure was repeated five times and k_{att} was determined as the mean. The external diaphragm was removed and replaced once after each run.

After determining all correction factors, a comparison was made between MAKS and the PK100 for the CCRI reference radiation qualities. MAKS and the PK100 were each set up at a distance of 500 mm from the x-ray tube. The field size at the reference plane was 50 millimeters. Diaphragms with apertures of 10 mm were used for MAKS and PK100. The measurements carried out with this setup are hereafter

referred to as M_0. To enable a comparison between MAKS and PK100 for a variable measurement setup, additional measurements were performed. In these measurements, the diaphragm of MAKS with 15 mm aperture was used, the field size was increased to 83 mm, and the dose rate was maximized. Tube currents of 30 mA (CCRI 10 kV, CCRI 30 kV) and 45 mA (CCRI 25 kV, CCRI 50 kVb, CCRI 50 kVa) were used to maximize the dose rate. The air kerma is calculated from the measured ionization charge according to formula (5) using all the correction factors given in Table 1 and Table 6. For the comparison the air kerma determined with MAKS ($K_{\mathrm{MAKS,norm}}$) or the PK100 ($K_{\mathrm{PK100,norm}}$) were normalized to the monitor ionization chamber charge.

3.1.4 Uncertainty Estimation

The reliable determination of air kerma with a FAC operated as a primary standard requires a comprehensive and transparent evaluation of the associated measurement uncertainty. Consequently, the uncertainty estimation follows the principles and recommendations of the *Guide to the Expression of Uncertainty in Measurement* [39], considering all relevant influence quantities contributing to the air kerma determination. The combined standard uncertainty of the air kerma determined with MAKS arises from several individual contributions, including the uncertainty of the measured ionization charge (0.03 %), the positioning of the FAC (0.01 %), the uncertainty of $1 - \bar{g}_{\mathrm{air}}$ (0.01 %) and W_{air} (0.35 %), as well as the uncertainties associated with the collecting volume and the various correction factors. The determination of the uncertainties of the collecting volume and the correction factors is described in detail in the following sections.

For the determination of the correction factor k_{ρ}, the air pressure in the laboratory is measured with a tolerance of 2 Pa, and the temperature inside the FAC is measured with a tolerance of 0.15 K. The air pressure and temperature are assumed to be uniformly distributed within these tolerance intervals.

The Type B uncertainty of the collecting volume is composed of the uncertainties of the aperture diameter and the measured geometric collecting length. The uncertainty of the aperture diameter arises from the form deviation of the aperture roundness. For the diaphragm with a nominal aperture diameter of 10 mm, the form deviation is 0.004 mm. The aperture diameter is assumed to be uniformly distributed within this form deviation. The uncertainty of the geometric collecting length consists of two contributions. The geometric collecting length is measured using a coordinate measuring machine with a measurement tolerance of 0.001 mm at three positions: on the beam axis and at ±5 mm offset, representing the geometric collecting length at the edges of the 10 mm aperture. The mean value of the geometric collecting length is assumed to be uniformly distributed between the maximum and minimum measured values. In addition, the measurement tolerance of the coordinate measuring machine is included in the uncertainty of the geometric collecting length.

The uncertainty of the correction factor k_{h} is a Type B uncertainty and is determined based on the values reported in ICRU 90 [3]. The relative humidity in the PTB laboratory, where the measurements of this work were performed, is controlled within the range of 30 % to 60 %. The actual humidity is assumed to be uniformly distributed within this range.

For the estimation of the Type B uncertainty of the correction factor $k_{\mathrm{ii}}k_w$, values reported by Takata and Begum [40] and by Buhr et al. [41], also given in ICRU Report 90 [3], are used. Spectral $k_{\mathrm{ii}}k_w$ values for the CCRI reference radiation qualities are derived from the reported monoenergetic $k_{\mathrm{ii}}k_w$ values. The uncertainty of $k_{\mathrm{ii}}k_w$ is derived from the spread of the available published datasets and calculated from the root mean square deviation, using the ICRU 90 values as reference.

The uncertainty of k_{s} includes the Type A contribution from the standard error of the parameters of the linear fits performed in Origin. In addition, a Type B uncertainty is considered, as the initial and

recombination parameters used for the determination of k_s were calculated as mean values of two cases ($n = n_1$ and $n = n_2$). These mean values are assumed to be uniformly distributed within the range defined by the two cases.

The Type A uncertainty of k_{pol} is calculated from repeated experimental determinations and expressed as the relative standard error of the mean.

The uncertainty of k_{att} comprises both a Type A and a Type B contribution. The Type A uncertainty arises from repeated experimental determinations and is expressed as the relative standard error of the mean. The Type B uncertainty is derived from the engineering tolerance of the air path length of MAKS (0.1 mm). Data generated in the study on the *Optimum Air Path Length* [27] using Monte Carlo simulations are used to determine the corresponding k_{att} values for the limit resulting from the engineering tolerance, which then define the upper and lower bounds within which k_{att} is uniformly distributed. Since k_{att} increases steeply at low energies, small deviations in the measurement setup or inaccuracies in the manufacturing significantly affect the uncertainty of k_{att} for CCRI 10 kV reference radiation quality. Therefore, the uncertainty of k_{att} for CCRI 10 kV is considered separately from that of the higher-energy radiation qualities.

The uncertainties of the correction factors k_{dia}, k_{sc}, k_{eloss} and k_{cpe} determined by Monte Carlo simulations, comprise several contributions, predominantly of Type B. These contributions arise from engineering tolerances, the statistical uncertainty of the Monte Carlo simulations, the choice of photon cross sections, the method used to average the monoenergetic correction factors with the x-ray spectrum, and the results of the sensitivity analysis of the used x-ray spectrum. The relevant engineering tolerances differ for each correction factor (see Table 4). Using data from the studies on the *Optimum Air Path Length* [27] and the *Diaphragm Design* [28], the limits within which the correction factors are assumed to be uniformly distributed can be established based on the given engineering tolerances. For k_{dia}, the uncertainty budget additionally accounts for the material composition of the diaphragm.

Table 4: Engineering tolerances contributing to the uncertainty of the correction factors.

Correction Factor	Geometry Parameter	Engineering Tolerance
k_{dia}	Diaphragm thickness	0.1 mm
	Aperture diameter	0.1 mm
	Aperture angle	1 °
	Air path length	0.1 mm
	Electrode separation	0.1 mm
k_{sc}	Air path length	0.1 mm
	Electrode separation	0.1 mm
k_{eloss}	Electrode separation	0.1 mm
k_{cpe}	Air path length	0.1 mm

To account for the choice of photon cross sections as a Type B uncertainty, Monte Carlo simulations were performed using both the XCOM and the renormalized MCDF-XCOM photon cross sections. The resulting correction factors are assumed to be uniformly distributed between the two sets of values. The uncertainty contribution arising from the averaging of monoenergetic correction factors with the x-ray spectrum is taken from the data reported in the study on the *Optimum Air Path Length* [27]. A sensitivity analysis was conducted to evaluate the impact of small inaccuracies in the x-ray spectrum

on the correction factors. For this purpose, correction factors were determined for two different x-ray spectra: measured with spectrometry and generated with SpekPy. The results of these calculations define the limits of a rectangular distribution, within which the correction factors are assumed to be uniformly distributed.

The Type B uncertainty of k_{d} arises from the engineering tolerances of multiple components of MAKS, as detailed in the study on the *Finite-element Modelling of the Electric Field* [31].

3.2 Characterization and Comparison: Results

To determine the air kerma with MAKS according to equation (5), the collecting volume must be defined. It results from the aperture diameter and the collecting length, following equation (6). Using FEM simulations, the collecting length was determined to be 16.062 mm. Table 5 shows the collecting volumes and associated uncertainties for the various diaphragms of MAKS.

Table 5: Collecting volumes and associated uncertainties of MAKS for different diaphragms.

Aperture Diameter [mm]	Collecting Volume [mm^3]	u [%]
8.0024	807.85	0.02
10.0054	1262.87	0.03
11.9970	1815.66	0.02
15.1050	2878.27	0.03

The default polarizing voltage for MAKS was determined by measuring the ionization charge while increasing the applied polarizing voltage. Figure 5 shows the measured ionization charge, normalized to the monitor chamber signal, plotted as a function of the applied polarization voltage. Based on the observed results, a default polarizing voltage of 2000 V was chosen for MAKS.

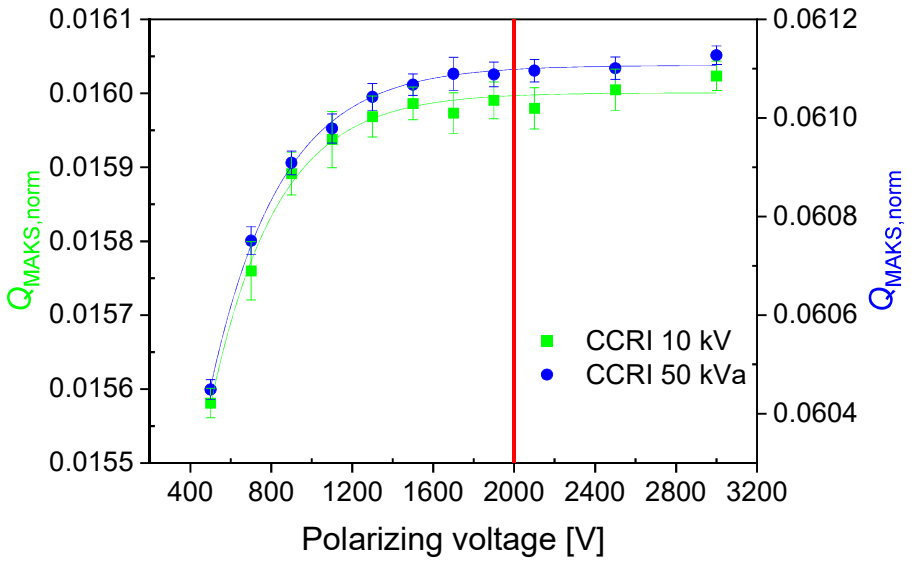

Figure 5: Measured ionization charge with MAKS, normalized to the monitor chamber signal, as a function of the applied polarization voltage. A default polarizing voltage of 2000 V was chosen for MAKS.

The correction factors determined for MAKS and their uncertainties are listed in Table 6. Figure A. 1 in the Appendix shows the linear fits for determining the initial and volume recombination parameters of the ion recombination correction factor k_{s} according to the method described above. The combined standard uncertainty of an air kerma measured with MAKS is 0.38 % for the CCRI 10 kV and 0.37 % for the other CCRI reference radiation qualities.

Table 6: Correction factors and associated uncertainties of MAKS.

	CCRI 10 kV	CCRI 30 kV	CCRI 25 kV	CCRI 50 kVb	CCRI 50 kVa	*u* [%]
Air density k_{ρ}			According to equation (7)			0.03
Humidity k_{h}	0.9980	0.9980	0.9980	0.9980	0.9980	0.04
Initial ionization and energy dependence of W_{air} $k_{\mathrm{ii}}k_{W}$	0.9953	0.9964	0.9967	0.9977	0.9980	0.10
Polarity k_{pol}	0.9998	0.9998	0.9998	0.9998	0.9998	0.01
Ion recombination k_{s}			$k_{\mathrm{s}} = 1.0000 + 4.16 * 10^{6} \frac{1}{\mathrm{A}} I_{\mathrm{V}}$ (21)			0.01[a]
Air attenuation k_{att}[b]	1.1428	1.0297	1.0204	1.0057	1.0028	0.01 0.05[c]
Diaphragm effects k_{dia}	0.9999	0.9989	0.9984	0.9970	0.9964	0.03
Scattering k_{sc}	0.9928	0.9949	0.9953	0.9967	0.9971	0.01
Electron loss k_{eloss}	1.0000	1.0000	1.0000	1.0000	1.0002	0.01
Charged particle equilibrium k_{cpe}	1.0000	1.0000	1.0000	1.0000	1.0000	0.01
Field distortion k_{d}	0.9989	0.9989	0.9989	0.9989	0.9989	0.04
$1 - \bar{g}_{\mathrm{air}}$	1.0000	1.0000	1.0000	1.0000	1.0000	0.01

[a] applies up to I_{V} = 500 pA

[b] related to reference temperature and air pressure

[c] for CCRI 10 kV

Figure 6 shows the ratios of the air kerma, normalized to the monitor chamber signal, measured with MAKS and the PK100 for the measurement setup M_0 and the measurement setups with the 15 mm aperture, the 83 mm radiation field and the maximized dose rate. The mean ratio of $K_{\mathrm{MAKS,norm}}/K_{\mathrm{PK100,norm}}$ across all CCRI reference radiation qualities is 1.014. Considering the correlations in the type B uncertainties of W_{air}, k_{h} and $k_{\mathrm{ii}}k_{W}$, and the uncertainty of the monitor ionization chamber

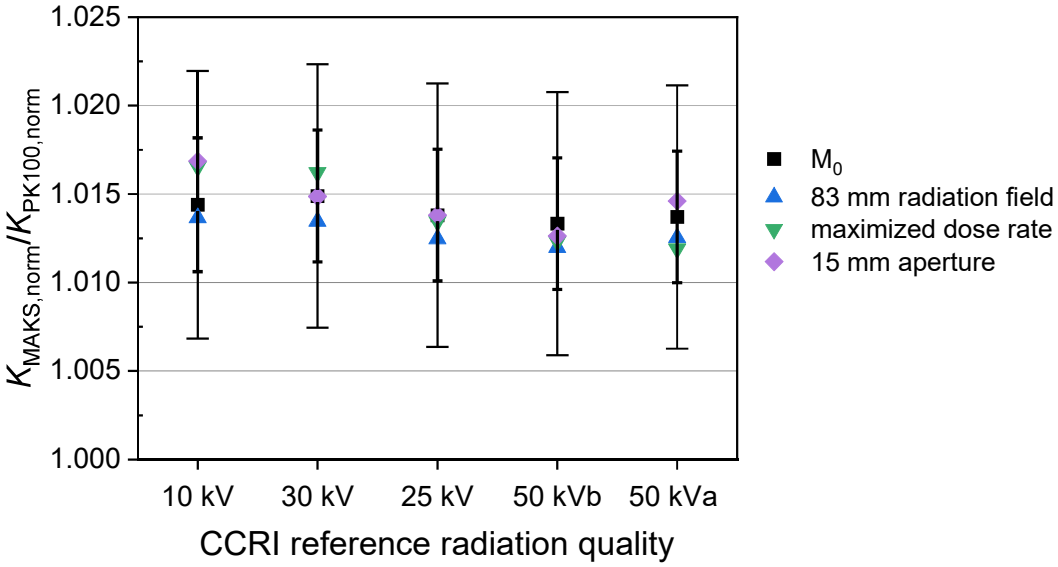

Figure 6: Ratios of air kerma K measured with MAKS and PK100 (each normalized to the monitor chamber signal) for the reference measurement setup M_0, the setup with 15 mm aperture, 83 mm radiation field, and maximized dose rate. Error bars showing standard (k = 1) and expanded (k = 2) uncertainties are included for M_0 only. For the other setups they are omitted to preserve visual clarity; their magnitude is identical.

charges (0.02 %) the combined uncertainty of $K_{\mathrm{MAKS,norm}}/K_{\mathrm{PK100,norm}}$ is 0.38 % for CCRI 10 kV and 0.37 % for the other CCRI reference radiation qualities. The ratios $K_{\mathrm{MAKS,norm}}/K_{\mathrm{PK100,norm}}$ for the measurement setups with the 83 mm radiation field, the maximized dose rate and the 15 mm aperture are within the combined standard uncertainty (k = 1) for the ratio $K_{\mathrm{MAKS,norm}}/K_{\mathrm{PK100,norm}}$ of the reference measurement setup M_0. For none of the measurement setups investigated is $K_{\mathrm{MAKS,norm}}$ equal to $K_{\mathrm{PK100,norm}}$ within the expanded uncertainty (k = 2).

3.3 Characterization and Comparison: Discussion

As part of the commissioning of MAKS, a detailed characterization and a comparison with the established air kerma primary standard PK100 was carried out. The first step in the characterization was a high-precision measurement of the geometry of MAKS. In addition, the default polarization voltage at which MAKS is to be operated was determined. This was followed by the determination of all parameters required for the conversion of a measured ionization charge to the air kerma. These parameters include the collecting length, the collecting volume, the correction factors and the associated uncertainties.

The characterization was successfully completed. All specified engineering tolerances were met. The default polarization voltage was set to 2000 V. The collecting length was determined by FEM simulation to 16.062 mm. If the geometrically determined collecting length of 15.979 mm were used to calculate the collecting volume, this would lead to an overestimation of the air kerma by 0.52 %. This clearly demonstrates that evaluating the collecting length by means of FEM simulation is essential. The correction factors determined by measurement or simulation are, as expected, as close as possible to unity and their uncertainties as low as possible. This is discussed in more detail in Section 4. However, the comparison with the PK100 revealed a discrepancy. On average, the air kerma determined with MAKS is approximately 1.4 % higher than that measured with the PK100. This systematic deviation is independent of radiation quality, dose rate, field size, and aperture diameter. Since the observed difference exceeds the expanded measurement uncertainty (k = 2), it is statistically significant. The following section examines potential systematic errors associated with MAKS and evaluates their contribution to the observed difference between MAKS and the PK100.

3.3.1 Assessment of Potential General Systematic Errors

An offset in the MAKS measurement signal caused by the electrometer, the voltage source, or other measurement devices can be ruled out, as all measurements were performed under identical conditions and using identical measurement equipment as with the PK100. Although there is a leakage current that causes an offset in the MAKS measurement signal, it is determined before and after each measurement and the measurement is corrected accordingly. The leakage current is three orders of magnitude lower than the measurement signal.

Another potential source of offset in the MAKS measurement signal is radiation transmission through the walls of MAKS or its diaphragm. The thickness of the wall, in particular the lead layer, and the thickness of the diaphragm were conservatively designed in advance of the manufacture of MAKS using Monte Carlo simulations. An increase in the measurement signal due to radiation transmitted through the wall or diaphragm would show an energy-dependent behavior. Since the difference between MAKS and the PK100 is energy-independent, the existence of such an error can already be ruled out. However, this was confirmed experimentally. For this purpose, air kerma measurements were carried out for CCRI 50 kVa with a 1 mm thin tungsten diaphragm without aperture for a large radiation field of 167 mm diameter at the reference plane. The signal from MAKS for this measurement

corresponds to less than 0.1 % of the signal from the measurement with a diaphragm with 10 mm aperture. An increase in the measurement signal of 1.4 % due to transmission through the wall or the diaphragm is therefore excluded. If the opening in the wall on the front side was additionally sealed with lead, this relative signal was reduced to less than 0.01 %. Thus, scattered radiation through the diaphragm holder between the housing and the diaphragm is responsible for the measured 0.1 % of the signal. This is considered in the correction factor for diaphragm effects k_{dia}.

The possibility that scattered radiation entering MAKS from behind could increase the measurement signal can also be excluded by the measurements with the diaphragm without an aperture. A second test, in which the exit hole was sealed with lead or covered by stacked lead bricks, produced no measurable change in the reference measurement M_0.

To further investigate the cause of the observed difference between MAKS and PK100, experiments were carried out to systematically investigate the influence of the positioning accuracy of MAKS. For this purpose, MAKS was rotated by up to 4 ° around the lateral and vertical axis so that the axis of MAKS was no longer aligned with the x-ray tube axis. In a further experiment, the FAC was rotated by 90 ° around the longitudinal axis and placed on its side (see Figure 7), with the axis still aligned with the beam direction. In addition, vertical, lateral and longitudinal shifts of up to 4 mm were made. The results (Appendix Figure A. 2) showed that only the longitudinal shift (shift along the beam direction) led to a significant change in the measured ionization charge. This can be explained by the inverse square law, according to which the intensity of a beam decreases proportionally to the square of the distance from the source. The rotations as well as vertical and lateral shifts had only a negligible effect on the signal. Therefore, inaccurate positioning or an incorrect definition of the axis of MAKS cannot account for the observed difference between MAKS and the PK100.

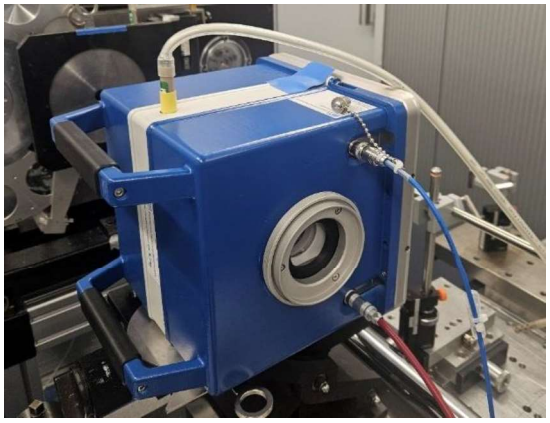

Figure 7: MAKS rotated by 90 ° around its longitudinal axis.

3.3.2 Assessment of Potential Systematic Errors in Correction Factors

The occurrence of systematic errors in the correction factors that could explain the difference between MAKS and the PK100 is discussed below for each individual correction factor.

The correction factor for humidity k_{h} as well as the correction factor for the initial ion pair and the deviation of the W_{air} value for low x-ray energy $k_{\mathrm{ii}}k_w$ are literature values and are identical for MAKS and the PK100. Systematic errors in k_{h} and $k_{\mathrm{ii}}k_w$ can therefore be ruled out as the cause of the observed difference between MAKS and the PK100.

The correction factor for air density k_{ρ} is calculated and applied directly by the measurement software used for each measurement. The equipment for measuring temperature and air pressure is identical for MAKS and PK100 measurements. It should also be noted that MAKS has two possible positions for

placing the temperature sensor. Measurements have shown that the difference to the PK100 is independent of the location of the temperature sensor. A possible error in the measurement of the temperature or pressure and the calculation or application of the k_ρ can therefore not explain the difference between MAKS and the PK100.

The correction factor for ion recombination k_s was determined experimentally for MAKS using a well-established method. The determined uncertainty of k_s is sufficiently small. k_s is a correction factor whose value is always greater than or equal to 1. MAKS was designed so that k_s is close to unity. In the event of an error in the experimental determination, k_s would exceed 1. This would result in a further increase in the air kerma determined with MAKS and would further increase the difference to the PK100. Consequently, the discrepancy between MAKS and PK100 cannot be explained by a possible incorrect determination of k_s.

The polarity correction factor k_{pol} was determined experimentally for MAKS using a well-established method. For MAKS, k_{pol} is nearly unity. Its uncertainty, determined by repeated measurements, is small enough to rule out a possible error in k_{pol} as the cause of the difference between MAKS and the PK100.

The correction factor for air attenuation k_{att} was determined experimentally using a well-established method, ensuring low uncertainty. While k_{att} can be significantly greater than 1, it is strongly energy-dependent. To account for a 1.4 % difference at CCRI 10 kV, the air path length of MAKS would have had to be overestimated by more than 5 mm, as shown by the data from the study on the *Optimum Air Path Length* [27]. Considering the tight engineering tolerances, such a large error can be ruled out. Moreover, even a 5 mm overestimation would have only a negligible effect on k_{att} at CCRI 50 kV. It can therefore be concluded that the 1.4 % higher air kerma measured by MAKS compared to the PK100 cannot be attributed to an error in determining k_{att}.

The correction factors for radial electron losses k_{eloss} and inadequate charged particle equilibrium k_{cpe} were determined using Monte Carlo simulation and are unity in the considered x-ray energy range. Both correction factors are related to the range of the secondary electrons in air. For a 50 keV electron, this range is approximately 41 mm. The air path length of MAKS, with a length of 60.4 mm, is sufficiently large to ensure charge particle equilibrium. With 61.9 mm, the electrode separation is large enough to ensure that the secondary electrons release all their energy before they reach the electrodes. If the air path length or the electrode separation were not selected correctly, k_{eloss} and k_{cpe} would be greater than 1. The increased air kerma of MAKS compared to the PK100 could therefore not be explained by a possible error in the choice or measurement of the air path length and the electrode separation or in the simulation of k_{eloss} and k_{cpe}.

In contrast, the correction factors for scattering k_{sc} and diaphragm effects k_{dia} are smaller than 1. Both were also determined using Monte Carlo simulations. Underestimating scattering processes in air or the interaction of the x-rays with the diaphragm in the simulation would lead to an overestimation of the air kerma. However, both correction factors are close to unity, with only minor uncertainties. The air path length and the electrode separation of MAKS are smaller than those of the PK100, resulting in a smaller volume of air through which the radiation passes. It is therefore expected that less scattering in air needs to be corrected for with MAKS, which is reflected in the correction factor k_{sc}. The geometry of the diaphragm was designed according to the data from the study on the *Diaphragm Design* [28] to minimize interactions of the radiation with the diaphragm, as confirmed by the calculated values for k_{dia}. Furthermore, both correction factors are energy-dependent. As the x-ray energy decreases, the probability that particles from interactions at the diaphragm reach the collecting

volume also decreases, causing k_{dia} to approach 1 at low energies. The correction factor k_{sc}, on the other hand, approaches 1 with increasing x-ray energy, as the probability of scattered Compton photons interacting within the collecting volume decreases. Therefore, a potential systematic error in either k_{dia} or k_{sc} cannot account for the constant difference observed between MAKS and PK100 over the energy range up to 50 keV.

The correction factor k_{d} is energy-independent. In addition, the study on the *Finite-element Modelling of the Electric Field* [31] demonstrated the sensitivity of the electric field within a FAC to geometric inaccuracies. A comparable sensitivity is described by Kessler [42]. Kessler found that a planarity tolerance of 0.05 mm between the collecting and guard electrodes leads to significant energy-independent deviations of the determined air kerma from the reference value, whereas a tolerance of 0.005 mm is sufficient to avoid such deviations. In MAKS, the planarity tolerance is 0.001 mm, and the tolerances of other components affecting the electric field were also chosen to be sufficiently tight to prevent systematic errors. Nevertheless, a method was developed to validate the electric field within MAKS, as calculated by FEM; this validation is described later.

3.3.3 Assessment of Potential Systematic Errors in the Collecting Volume

The air kerma determined with MAKS is inversely proportional to the collecting volume. If the collecting volume of MAKS were underestimated, this would result in a systematic, energy-independent overestimation of the air kerma. The collecting volume was calculated from the aperture diameter and the collecting length. In the following, possible systematic errors, which could explain an air kerma overestimated by 1.4 %, caused by the diaphragm or the collecting length are discussed.

For the 10 mm diaphragm, an aperture diameter 0.07 mm too small would result in a collecting volume that is 1.4 % smaller. The MAKS diaphragms were manufactured and measured with the highest precision. The form deviation of the roundness for the 10 mm diaphragm is only 0.004 mm, making an error of 0.07 mm in the aperture diameter impossible. Nevertheless, a potential systematic error in the air kerma determined with MAKS, caused by systematic errors in the diaphragm, was experimentally investigated. Figure 6 already showed that the difference between MAKS and PK100 is independent of the aperture diameter. To test whether the position of the diaphragm within the housing introduces an error, several measurements were carried out with MAKS in which the diaphragm position was varied. On the one hand, the diaphragm was shifted by approximately 1 mm across the beam direction. On the other hand, the diaphragm was deliberately tilted in the diaphragm holder. In addition, a 3D-printed diaphragm holder was developed, allowing the diaphragm to be screwed onto the housing from the front (see Figure 8). The diaphragm of MAKS and also the diaphragm of the PK100 were mounted in this diaphragm holder for an air kerma measurement. Monte Carlo simulations were performed to determine the correction factors for the setup with the external diaphragm.

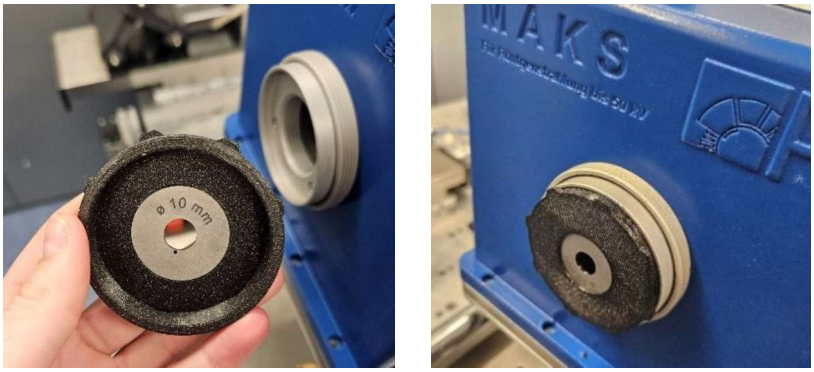

Figure 8: 3D-printed diaphragm holder allowing the diaphragm to be screwed onto the housing of MAKS from the front.

Figure 9 shows the results of the measurements investigating potential errors associated with the diaphragm. The ratio of the air kerma measured with MAKS and the PK100 is within the uncertainty of the measurement M_0 for both the shifted and the tilted diaphragm. The external mounting of the diaphragm of MAKS and the PK100 did not lead to significantly different measurement results for any CCRI reference radiation quality, except for CCRI 10 kV. For CCRI 10 kV, the air kerma values measured with MAKS show better agreement with those measured with the PK100. However, this is because k_{att} was determined by simulation rather than experimentally for this measurement setup to obtain a time-efficient estimate. The results show that simulation-based determination of k_{att} is not suitable in this x-ray energy range. This example illustrates the impact of a systematic error in the determination of an energy-dependent correction factor. Finally, these measurements confirm that the air kerma determined with MAKS is not affected by any systematic error associated with the diaphragm.

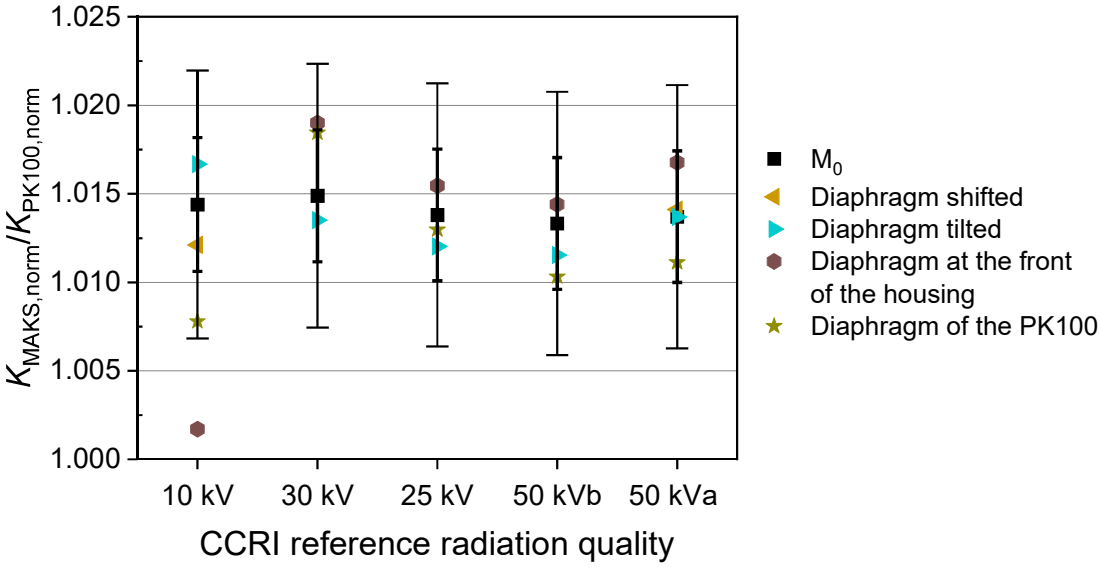

Figure 9: Ratios of air kerma K measured with MAKS and PK100 (each normalized to the monitor chamber signal) for the reference measurement setup M_0 and the setups with modified diaphragms. Error bars showing standard (k = 1) and expanded (k = 2) uncertainties are included for M_0 only to preserve visual clarity.

To produce a 1.4 % reduction in the collecting volume, the collecting length would have to be underestimated by 0.22 mm. An error of this magnitude in the measured geometric collecting length can be excluded given the measuring tolerance of the coordinate measuring machine, which is 0.001 mm. However, the collecting length is determined not only by geometry but also by the electric field within MAKS, which is evaluated using FEM simulations. Consequently, the electric field of MAKS was subsequently analyzed for potential systematic errors.

First, the resistances of the voltage divider were remeasured, and the contacting of the guard rings was checked. No issues were detected. Second, the method of using the FEM simulation to represent the electric field within MAKS was validated. This was carried out using the short-circuit experiment described by Gschweng and Pojtinger [43]. One of the resistors of MAKS was short-circuited in order to manipulate the electric field. The ionization charge for the CCRI reference radiation qualities was determined with the modified MAKS (resistor was short-circuited) five times and set in relation to the results of measurement M_0 without short-circuiting. In the FEM simulation, this short-circuit experiment was also simulated and the ratio of the effective collecting length at the level of the beam axis for the case with and without short-circuit was calculated. Figure A. 3 from the Appendix shows the corresponding ratios from measurement and simulation. In the simulation, the short-circuiting of the resistor resulted in a relative increase in the effective collecting length of 0.62 %. In the measurement,

the short-circuiting of the resistor resulted in an increase in the measured ionization charge of 0.64 % on average across all CCRI reference radiation qualities. The good agreement between the relative change in the measurement signal and the FEM-simulated effective collecting length confirms the applicability of the FEM simulation for representing changes in the electric field of MAKS.

In addition, the short-circuit experiment shows that the air kerma would not be increased by 1.4 % even if one resistor had failed completely. Therefore, other potential sources of systematic error associated with the electric field were examined. The data from the study on the *Finite-element Modelling of the Electric Field* [31] show that an offset of 0.1 mm between the collecting and guard electrode would lead to a relative change in the collecting length of 1.4 %. However, the planarity between the collecting and guard electrode was ensured in compliance with the specified engineering tolerance of 0.001 mm. In addition to the planarity between the collecting and guard electrode, the positions of the electrodes and the guard rings within the plate stack are also crucial for the electric field. These positions were maintained with an engineering tolerance of 0.015 mm. To assess the influence of deviations from this tolerance, the screws holding the plate stack together were loosened, and the plates were slightly shifted. No significant change in the measured ionization charge was observed under this setup. An error in the collecting length could also result from an electric potential difference between the collecting and guard electrode. However, an existing electric potential difference was not measured. Nevertheless, measurements were performed to assess how an electric potential difference affects the measurement signal of MAKS. FEM simulations showed that an electric potential of the collecting electrode approximately 1.5 V higher than that of the guard electrode leads to a collecting length that is 1.4 % shorter. To generate this electric potential difference, a 1.5 V battery was connected between the collecting electrode and the electrometer (see Figure 10).

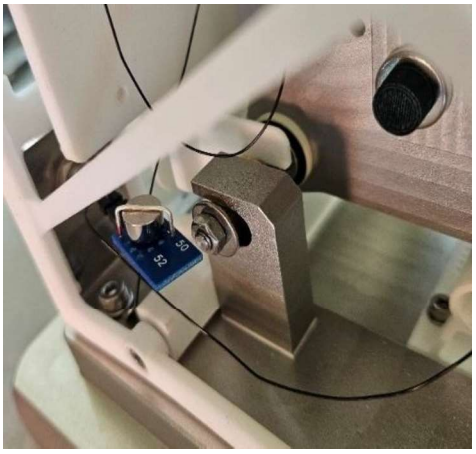

Figure 10: Experimental setup with a 1.5 V battery connected between the collecting electrode and the electrometer to generate an electric potential difference between the collecting and the guard electrode.

Figure 11 shows how the ratio of the air kerma determined with MAKS and PK100 changes when the battery is inserted with both polarity orientations. The battery generates an electric potential difference between the collecting and guard electrode, which alters the electric field of MAKS. As a result, the collecting length becomes shorter or longer, leading to a corresponding decrease or increase in the collecting volume. As anticipated from the FEM simulations, increasing the electric potential of the collecting electrode by 1.5 V results in a 1.4 % reduction in the measurement signal of MAKS. The battery experiment therefore further confirms the suitability of FEM simulations for determining changes in the electric field of MAKS.

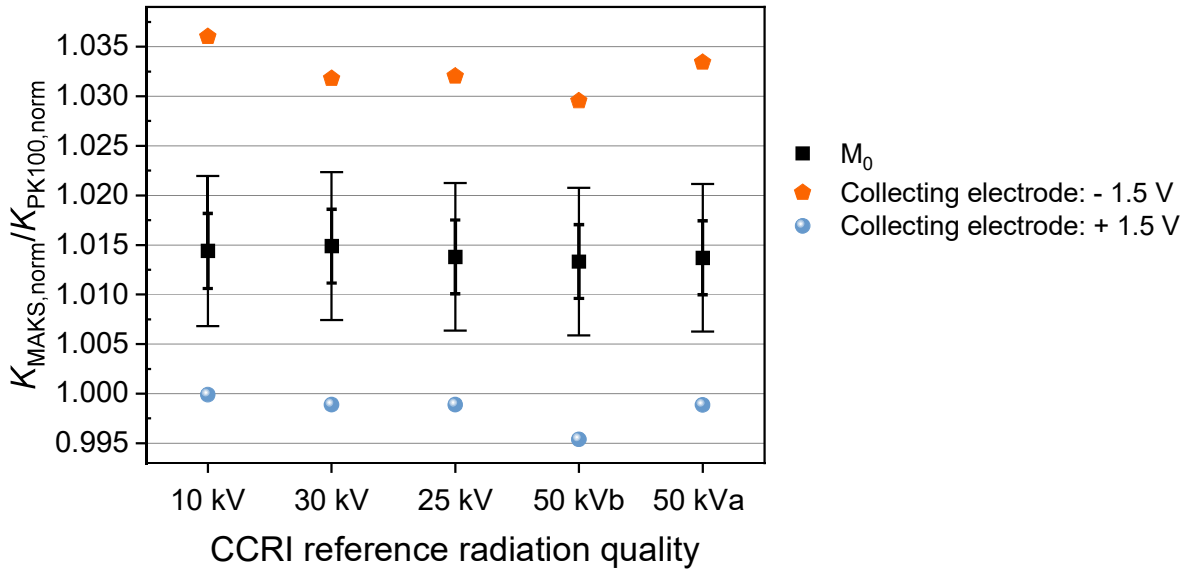

Figure 11: Ratios of air kerma K measured with MAKS and PK100 (each normalized to the monitor chamber signal) for the reference measurement setup M_0 and for increased and decreased electric potentials of the collecting electrode. Error bars showing standard (k = 1) and expanded (k = 2) uncertainties are included for M_0 only. For the other setups they are omitted to preserve visual clarity; their magnitude is identical.

The short-circuit and battery experiments demonstrated twice that an FEM simulation can be used to represent a change in the electric field of MAKS. However, it was not possible to make a statement about the absolute accuracy of the simulated electric field. Therefore, an approach was developed that allows the validation of an absolute parameter of the electric field by comparison with a corresponding measurement. Due to the capacitor-like structure of MAKS, a comparison of the capacitances is possible. The capacitance C of MAKS results from

$$C = \frac{Q_\mathrm{e}}{V}. \tag{22}$$

The electric charge Q_e is the charge of the capacitor induced by the applied default polarization voltage $V = 2000\ \mathrm{V}$. It should not be confused with the ionization charge, which is measured to determine the air kerma. The capacitance of MAKS was determined experimentally five times and was also determined by using FEM simulations. Initially, the experimentally determined capacitance was significantly higher than the simulated capacitance. By insulating the cable and inserting aluminum foil into the gap between the guard electrode and the housing (see Figure A. 4 in the Appendix), the influence of existing parasitic capacitances could be minimized. After adapting MAKS, the results from measurement and simulation were almost identical, with an average value of $C = 166.67\ \mathrm{fF}$ for the measurement and $C = 166.81\ \mathrm{fF}$ for the FEM simulation. The good agreement between the capacitances from measurement and FEM simulation confirms that the electric field distribution is correctly reproduced in the simulation. Consequently, the electric field lines used to determine the collecting length and k_d are accurately represented in the FEM Simulation.

The presented validation confirms that the collecting length and the correction factor k_d is determined correctly and not is not affected by a systematic error that could explain the difference between MAKS and the PK100.

4 Discussion

The development of the new air kerma primary standard for dosimetry in x-ray diagnostics followed a systematic and precise approach. The aim of the development was to specialize the new primary standard for the x-ray energy range below 50 keV. The process encompassed all phases, ranging from initial concept development to dimensioning and the definition of engineering tolerances using Monte Carlo and FEM simulations, and finally to the commissioning of the newly developed free-air ionization chamber, called MAKS. The detailed and systematic methodology used for dimensioning MAKS and its individual components, as well as the high-precision manufacturing of MAKS, are particularly noteworthy. As a result, the correction factors required to calculate the air kerma from the measured ionization charge were closer to unity compared with those of the established PTB primary standard, PK100, thereby generally reducing potential sources of error and large uncertainties.

Reducing the air path length from 97.2 mm (PK100) to 60.4 mm (MAKS) results in a significant reduction of the largest correction at low x-ray energies, namely the air attenuation correction, by approximately 40 %. For the CCRI 10 kV reference radiation quality, this means that k_{att} was reduced from 1.2294 (PK100) to 1.1482 (MAKS). In addition, the uncertainty of k_{att} for MAKS is significantly lower, at 0.05 % (CCRI 10 kV) or 0.01 %, than that of PK100, which is 0.21 %. This improvement is due to the optimization of the measurement setup for determining k_{att}, which was carried out as part of a master's thesis.

By dispensing with the guard wires used in the PK100, the guard wire attenuation correction factor and its associated uncertainty contribution of 0.21 % are eliminated for MAKS.

The reduction of the electrode separation from 234 mm (PK100) to 61.9 mm (MAKS) and the adequate selection of the default polarization voltage for MAKS results in a minimization of ion recombination losses. This means that the required ion recombination correction is reduced to a minimum. The ion recombination correction factor k_{s} required for MAKS is below 1.001 for ionization currents of up to 250 pA. For the PK100, k_{s} is over 1.007 for this current. In addition, the uncertainty of k_{s} was reduced by more than an order of magnitude, from 0.11 % to 0.01 %, compared with the PK100.

In addition, minimizing the air path length and the electrode separation of MAKS results in a reduced scattering correction. Although the correction factor k_{sc} is already close to unity for PK100, the scattering correction for MAKS is only half as large as that for PK100. The uncertainty of k_{sc} was reduced by a factor of five, from 0.05 % (PK100) to 0.01 % (MAKS).

Despite the desired minimization of the air path length and the electrode separation, these dimensions were chosen so that k_{eloss} and k_{cpe} remain 1. With the PK100, the uncertainty of k_{eloss} is 0.05 %, whereas with MAKS it is only 0.01 % for k_{eloss} and k_{cpe}.

Minimizing the air path length of MAKS increases correction for diaphragm effects. First, the shorter air path length reduces the distance that particles generated by interactions with the diaphragm must travel to reach the collecting volume and a larger fraction of these particles reach the collecting volume. Second, the diaphragm is located inside MAKS rather than at the front of the housing. As a result, particles resulting from interactions with both the housing aperture and the diaphragm holder also contribute to the measured ionization charge. These must be corrected for with the diaphragm correction factor k_{dia}. Despite these two limitations, k_{dia} for MAKS is as close to unity as for the PK100, which was achieved by optimizing the diaphragm geometry. It was also possible to reduce the uncertainty of k_{dia} from 0.07 % (PK100) to 0.03 % (MAKS).

Minimizing the air path length results in a shortening of the guard electrode, which increases distortions in the electric field. In contrast, minimizing the electrode separation increases electric field uniformity. In the present work, an approach was developed to adjust the correction factor k_{d} to unity using FEM simulations. This approach involves the geometric optimization of the MAKS components that shape the electric field. With a k_{d} value of 0.9989, this objective was achieved for MAKS. The PK100 has six collecting electrodes with different values for k_{d} (see Table 7). These values were determined under the assumption that k_{d} should be unity for the fourth collecting electrode, as it is geometrically in the center of the PK100. The values for k_{d} for the remaining collecting electrodes were determined from the ratios of the measured ionization currents relative to the ionization current of the fourth collecting electrode. However, this assumption and method warrant critical assessment. On the one hand, the fourth collecting electrode is not positioned symmetrically in the geometric center of the PK100. Furthermore, no information is available about the lengths of the collecting electrodes and the separating air gaps, the chamfers of the electrodes, the planarity of the electrodes to each other and other engineering tolerances. The present work has shown that these parameters are crucial for the electric field and k_{d}. Against this background, the simplifying assumption for the fourth collecting electrode is highly questionable. This is further illustrated by the fact that k_{d} of the fifth collecting electrode deviates more from unity than that of the sixth collecting electrode. However, according to the mentioned assumption, a collecting electrode located closer to the center would be expected to exhibit lower electric field distortion and thus a k_{d} closer to unity. Consequently, no absolute values for k_{d} can be determined from the ratios of the ionization currents measured with the various collecting electrodes. The uncertainty of k_{d} stated for the PK100 (0.1 %) is a rough estimate. In contrast, the uncertainty of k_{d} for MAKS (0.04 %) was determined on the basis of detailed calculations, considering the tight engineering tolerances achieved through high-precision manufacturing.

Table 7: Collecting electrodes of the PK100 and their corresponding correction factors for electric field distortion k_d.

Collecting electrode	1	2	3	4	5	6
k_{d}	0.9910	0.9938	0.9969	1.0000	0.9905	0.9934

In addition to reducing the required corrections and their associated uncertainties, MAKS offers several practical advantages over the PK100. MAKS is characterized by a compact design and a low weight of less than 10 kg and is portable. The tripod and positioning aids enable both axial and height adjustment of MAKS. Furthermore, the documentation covering the entire development of MAKS is complete and detailed. In contrast, the documentation for the PK100 contains significant gaps: records of dimensions, materials, engineering tolerances, and uncertainty determinations are lacking.

The determination of the air kerma with MAKS is stable and reproducible. However, the air kerma determined with MAKS shows a significant difference to the air kerma determined with the PK100. This difference is independent of measurement parameters such as radiation quality, radiation field size, aperture diameter of MAKS and dose rate. The existence of systematic errors associated with the correction factors, which could explain this difference, was ruled out. The correction factors are either given by literature values, experimentally confirmed, unity with small uncertainties or energy-dependent. A potential systematic error due to an incorrectly assumed size of the collecting volume was also ruled out. The aperture of the diaphragm and the collecting electrode length were measured with high accuracy. In addition, measurements with MAKS are insensitive to different diaphragm constellations. The correct representation of the electric field within MAKS using FEM simulations was validated several times. In this context, the comparison between the capacitance of MAKS determined

experimentally and that obtained from FEM simulations should be highlighted as a highly effective method of validation.

In summary, no clear explanation was found for the observed difference between the air kerma determined with MAKS and the PK100. There is currently no evidence to suggest that systematic errors occur in measurements using MAKS. A potential systematic error in air kerma measurements with the PK100 arises from the questionable method used to determine the correction factor k_{d}. Furthermore, the collecting length of the PK100 was determined exclusively via the geometry and not by considering the electric field. Due to the incomplete documentation of the geometry of the PK100, an analysis of the electric field and a reliable redetermination of k_{d} and the collecting length is not possible. It was further observed that, while the difference between MAKS and the PK100 is independent of the diaphragm selected for MAKS, it depends on the diaphragm chosen for the PK100. For the CCRI reference radiation qualities, the measured air kerma deviates by up to 0.9 % when the PK100 diaphragm with 20 mm aperture is used instead of the one with 10 mm aperture (see Table 8). This behavior may indicate that the PK100 diaphragms are not manufactured or dimensionally characterized with sufficient accuracy, resulting in an imprecise definition of the collecting volume of the PK100 and potentially introducing errors in the correction factor for diaphragm effects, k_{dia}. Since the deviation is particularly pronounced for the 10 kV spectrum, an additional contribution from an inaccurate determination of the guard wire attenuation correction factor, k_{ap}, cannot be excluded.

Table 8: Relative deviation of air kerma determined with the PK100 when using a 20 mm diaphragm instead of a 10 mm diaphragm.

CCRI reference radiation quality	10 kV	30 kV	25 kV	50 kVb	50 kVa
Relative air kerma deviation [%]	0.94	0.55	0.32	0.38	0.63

However, the fact that the PK100 already participated successfully in the BIPM.RI(I)-K2 Key Comparisons in 1999 [44], 2014 [45] and 2024 [16] contradicts the hypothesis of a systematic error in air kerma measurements with the PK100.

5 Conclusion

The present work was carried out against the background of a constantly increasing demand for calibrations with an air kerma primary standard of PTB in the x-ray energy range below 50 keV, especially in the field of mammography. In the context of this project, the development of the novel free-air ionization chamber MAKS was successfully completed. This FAC is intended to serve as PTB's new air kerma primary standard for the x-ray energy range below 50 keV. MAKS is a compact, mobile, and high-precision FAC whose geometry has been specially optimized for the use in this energy range.

A major focus of the present work was on the methodological preparatory work for the development of a specialized air kerma primary standard. In this study, it was shown how detailed Monte Carlo and FEM simulations can be systematically used to optimize the geometry of a FAC. The aim was to ensure that the correction factors required to determine the air kerma are as close to unity as possible. In addition, engineering tolerances for individual components and geometric parameters were derived from the simulations, allowing their contributions to the standard uncertainty of air-kerma measurements with MAKS to be minimized. The high-precision production and geometric measurement of MAKS was carried out using state-of-the-art manufacturing processes. Compliance with tight engineering tolerances resulted in a reduction of the uncertainties of the required correction factors and thus to a low uncertainty in the determination of the air kerma with MAKS. The concepts developed in this work are not exclusively limited to MAKS but can also be transferred to other primary standards. The approach described can be regarded as a methodological advance in the development of future primary standards.

However, a comparison of MAKS with the established PTB air kerma primary standard PK100 revealed a significant discrepancy in the determined air kerma of approximately 1.4 %. Despite extensive investigations, no systematic error or indication of a systematic error could be identified in the measurements with MAKS. Additional work is therefore required before MAKS can be established as an air kerma primary standard. The relevant aspects include in particular the investigation of the long-term stability and consistency of the measurements with MAKS. In addition, the ground electrode, which has been identified as the most critical component of the FAC, will be newly manufactured. This should ensure that the influence of the chamfers on the collecting and guard electrode on the electric field is correctly represented by the FEM simulations. Furthermore, international comparisons of MAKS with other established air kerma primary standards are planned. At the same time, the determination of the collecting volume and the correction factors of the PK100 should be verified and other possible potential sources of error on measurements with the PK100 must be investigated. However, due to the incomplete documentation and the limited possibilities for geometric remeasurement without dismantling the FAC, this is only possible to a limited extent.

Nevertheless, the present work provides a comprehensive investigation of the free-air ionization chamber MAKS and its application as an air kerma primary standard for low-energy x-rays. All relevant aspects of the FAC design, the measurement procedures, and the associated correction factors have been systematically analyzed and critically assessed. In this way, the work establishes a well-documented and comprehensible basis for the further development of MAKS and for future studies aimed at resolving the observed discrepancy. Moreover, the results and insights presented here contribute valuable information for the development of air kerma primary standards and for ongoing and future national and international comparisons.

References

[1] Katalinic A, Eisemann N, Kraywinkel K, Noftz MR, Hübner J. Breast cancer incidence and mortality before and after implementation of the German mammography screening program. International Journal of Cancer 2020;147:709–18. https://doi.org/10.1002/ijc.32767.

[2] Yaffe MJ, Mainprize JG. Risk of Radiation-induced Breast Cancer from Mammographic Screening. Radiology 2011;258:98–105. https://doi.org/10.1148/radiol.10100655.

[3] ICRU. REPORT No. 90: KEY DATA FOR IONIZING-RADIATION DOSIMETRY: MEASUREMENT STANDARDS AND APPLICATIONS 2016.

[4] Burns D, Büermann L. Free-air ionization chambers. Metrologia 2009;46:S9. https://doi.org/10.1088/0026-1394/46/2/S02.

[5] Grimbergen TWM, Dijk E van, Vries W de. Correction factors for the NMi free-air ionization chamber for medium-energy x-rays calculated with the Monte Carlo method. Physics in Medicine & Biology 1998;43:3207. https://doi.org/10.1088/0031-9155/43/11/004.

[6] M T Niatel. An experimental study of ion recombination in parallel-plate free-air ionization chambes. Physics in Medicine & Biology 1967;12:555. https://doi.org/10.1088/0031-9155/12/4/009.

[7] De Almeida C, Niatel M. Comparison between IRD and BIPM exposure and air kerma standards for cobalt gamma rays. Rapport BIPM 1986;86:12.

[8] M Boutillon. Volume recombination parameter in ionization chambers. Physics in Medicine & Biology 1998;43:2061. https://doi.org/10.1088/0031-9155/43/8/005.

[9] Ketelhut S, Büermann L, Hilgers G. Catalog of x-ray spectra of Mo-, Rh-, and W-anode-based x-ray tubes from 10 to 50 kV. Physics in Medicine & Biology 2021;66:115013. https://doi.org/10.1088/1361-6560/abfbb2.

[10] Burns DT, Kessler C, Butler D, Shoyookhi S, Hanlon M. Key comparison BIPM.RI(I)-K2 of the air-kerma standards of the ARPANSA, Australia, and the BIPM in low-energy x-rays. Metrologia 2022;59:06022. https://doi.org/10.1088/0026-1394/59/1A/06022.

[11] Burns DT, Kessler C, Finta V. Key comparison BIPM.RI(I)-K2 of the air-kerma standards of the BFKH, Hungary, and the BIPM in low-energy x-rays. Metrologia 2023;60:06016. https://doi.org/10.1088/0026-1394/60/1A/06016.

[12] Burns DT, Kessler C, Jinjie W, Peiwei W. Key comparison BIPM.RI(I)-K2 of the air-kerma standards of the NIM, China, and the BIPM in low-energy x-rays. Metrologia 2019;56:06006. https://doi.org/10.1088/0026-1394/56/1A/06006.

[13] Burns DT, Kessler C, Kelly M, Maughan DJ, Sander T. Key comparison BIPM.RI(I)-K2 of the air-kerma standards of the NPL, UK, and the BIPM in low-energy x-rays. Metrologia 2019;56:06004. https://doi.org/10.1088/0026-1394/56/1A/06004.

[14] Burns DT, Kessler C, Mainegra-Hing E, Shen H, McEwen MR. Key comparison BIPM.RI(I)-K2 of the air-kerma standards of the NRC, Canada, and the BIPM in low-energy x-rays. Metrologia 2019;56:06002. https://doi.org/10.1088/0026-1394/56/1A/06002.

[15] Burns DT, Kessler C, Michalik Ł. Key comparison BIPM.RI(I)-K2 of the air-kerma standards of the GUM, Poland, and the BIPM in low-energy x-rays. Metrologia 2022;59:06014. https://doi.org/10.1088/0026-1394/59/1A/06014.

[16] Burns DT, Kessler C, Pojtinger S. Key comparison BIPM.RI(I)-K2 of the air-kerma standards of the PTB, Germany, and the BIPM in low-energy x-rays. Metrologia 2024;61:06016. https://doi.org/10.1088/0026-1394/61/1A/06016.

[17] Burns DT, Kessler C, Prez L de, Joulaeizadeh L. Key comparison BIPM.RI(I)-K2 of the air-kerma standards of the VSL, Netherlands and the BIPM in low-energy x-rays. Metrologia 2014;51:06010. https://doi.org/10.1088/0026-1394/51/1A/06010.

[18] Burns DT, Kessler C, Roger P, Toni MP, Pinto M, Bovi M, et al. Key comparison BIPM.RI(I)-K2 of the air-kerma standards of the ENEA-INMRI, Italy and the BIPM in low-energy x-rays. Metrologia 2011;48:06010. https://doi.org/10.1088/0026-1394/48/1A/06010.

[19] Burns DT, Kessler C, Sochor V. Key comparison BIPM.RI(I)-K2 of the air-kerma standards of the CMI, Czech Republic and the BIPM in low-energy x-rays. Metrologia 2016;53:06009. https://doi.org/10.1088/0026-1394/53/1A/06009.
[20] Burns DT, Kessler C, Steurer A, Tiefenboeck W, Bauer M. Key comparison BIPM.RI(I)-K2 of the air-kerma standards of the BEV, Austria and the BIPM in low-energy x-rays. Metrologia 2015;52:06001. https://doi.org/10.1088/0026-1394/52/1A/06001.
[21] Burns DT, Kessler C, Tanaka T, Kurosawa T, Saito N. Key comparison BIPM.RI(I)-K2 of the air-kerma standards of the NMIJ, Japan and the BIPM in low-energy x-rays. Metrologia 2015;52:06008. https://doi.org/10.1088/0026-1394/52/1A/06008.
[22] Burns DT, Kessler C, Yi C-Y, Kim YH. Key comparison BIPM.RI(I)-K2 of the air-kerma standards of the KRISS, Republic of Korea, and the BIPM in low-energy x-rays. Metrologia 2022;59:06011. https://doi.org/10.1088/0026-1394/59/1A/06011.
[23] Burns DT, Roger P, Denozière M, Leroy E. Key comparison BIPM.RI(I)-K2 of the air-kerma standards of the LNE–LNHB, France and the BIPM in low-energy x-rays. Metrologia 2011;48:06013. https://doi.org/10.1088/0026-1394/48/1A/06013.
[24] Burns DT, Roger P, Villevalde AY, Oborin AV. Key comparison BIPM.RI(I)-K2 of the air-kerma standards of the VNIIM, Russian Federation and the BIPM in low-energy x-rays. Metrologia 2012;49:06003. https://doi.org/10.1088/0026-1394/49/1A/06003.
[25] Burns DT, Lamperti PJ, O'Brien M. Comparison of the air kerma standards of the NIST and the BIPM in the low-energy X-ray range 1999:11. https://doi.org/10.6028/jres.104.009.
[26] Büermann L. The PTB free-air ionization chambers 2021. https://doi.org/10.7795/120.20220324.
[27] Gschweng J, Pojtinger S. Free-air ionization chambers for the measurement of air kerma in low-energy x-rays – optimum air path length and the limitations of averaging monoenergetic correction factors. Metrologia 2025;62. https://doi.org/10.1088/1681-7575/adc39d.
[28] Gschweng J, Pojtinger S. OPTIMAL GEOMETRIC DESIGN OF THE DIAPHRAGM OF A FREE-AIR IONIZATION CHAMBER FOR LOW-ENERGY X-RAYS. RAP CONFERENCE PROCEEDINGS 2025;10:16–20. https://doi.org/10.37392/RAPPROC.2025.04.
[29] Kawrakow I, Rogers D. The EGSnrc code system. NRC Report PIRS-701, NRC, Ottawa 2000;17.
[30] COMSOL Multiphysics® v. 6.1. www.comsol.com. COMSOL AB, Stockholm, Schweden.
[31] Gschweng J, Pojtinger S. Development of the new PTB air kerma primary standard—optimization of the geometry for minimal electric field distortions and assessment of the associated uncertainties using the finite element method. Metrologia 2025;62. https://doi.org/10.1088/1681-7575/ae033e.
[32] Burns D, Kessler C. Measuring conditions and uncertainties for the comparison and calibration of national dosimetric standards at the BIPM. Rapport BIPM-2024/04 2024. https://doi.org/10.59161/Rapport202404.
[33] Mainegra-Hing E, Reynaert N, Kawrakow I. Novel approach for the Monte Carlo calculation of free-air chamber correction factors. Medical Physics 2008;35:3650–60. https://doi.org/10.1118/1.2955551.
[34] Rogers DWO, Townson RW. On calculating kerma, collision kerma and radiative yields. Medical Physics 2019;46:5173–84. https://doi.org/10.1002/mp.13744.
[35] Pojtinger S. On the robustness of detective quantum efficiency within the limits of IEC 61267 RQA standard radiation qualities. Radiation Protection Dosimetry 2024;200:515–22. https://doi.org/10.1093/rpd/ncae029.
[36] Sechopoulos I, Rogers DWO, Bazalova-Carter M, Bolch WE, Heath EC, McNitt-Gray MF, et al. RECORDS: improved Reporting of montE CarlO RaDiation transport Studies: Report of the AAPM Research Committee Task Group 268. Medical Physics 2018;45:e1–5. https://doi.org/10.1002/mp.12702.
[37] Kawrakow I, Fippel M. Investigation of variance reduction techniques for Monte Carlo photon dose calculation using XVMC. Physics in Medicine & Biology 2000;45:2163. https://doi.org/10.1088/0031-9155/45/8/308.
[38] COMSOL Multiphysics® v. 6.3. www.comsol.com. COMSOL AB, Stockholm, Schweden.

[39] Evaluation of measurement data—Guide to the expression of uncertainty in measurement 2008.
[40] Takata N, Begum A. Corrections to air kerma and exposure measured with free air ionisation chambers for charge of photoelectrons, Compton electrons and Auger electrons. Radiation Protection Dosimetry 2008;130:410–8. https://doi.org/10.1093/rpd/ncn093.
[41] Buhr H, Büermann L, Gerlach M, Krumrey M, Rabus H. Measurement of the mass energy-absorption coefficient of air for x-rays in the range from 3 to 60 keV. Physics in Medicine & Biology 2012;57:8231. https://doi.org/10.1088/0031-9155/57/24/8231.
[42] Kessler C. Développement et mise en place au BIPM d'un systéme international de comparaison et d'étalonnage pour la dosimétrie en mammographie. 2013.
[43] Gschweng J, Pojtinger S. PP10.04 VALIDATION OF THE FINITE ELEMENT METHOD TO DETERMINE THE SENSITIVE VOLUME OF FREE-AIR IONIZATION CHAMBER STANDARDS. Physica Medica 2024;125:103811. https://doi.org/10.1016/j.ejmp.2024.103811.
[44] DT Burns, L Bueermann, H M Kramer, B Lange. Comparison of the air-kerma standards of the PTB and the BIPM in the low-energy X-ray range. 2001.
[45] Burns DT, Kessler C, Büermann L. Key comparison BIPM.RI(I)-K2 of the air-kerma standards of the PTB, Germany and the BIPM in low-energy x-rays. Metrologia 2014;51:06011. https://doi.org/10.1088/0026-1394/51/1A/06011.

Appendix

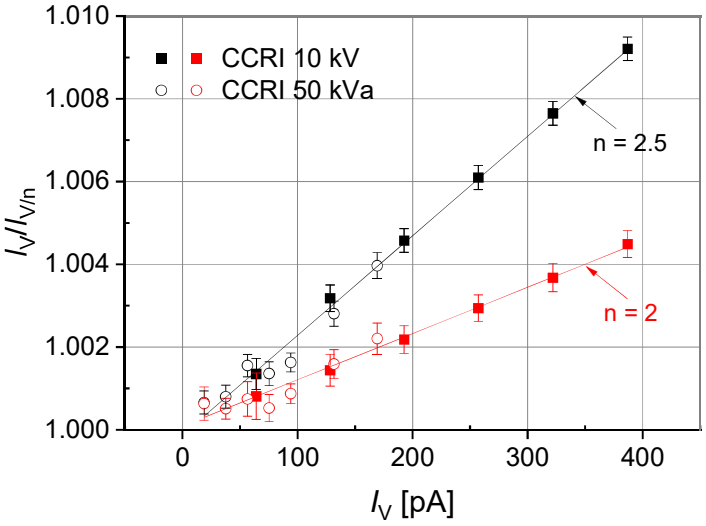

Figure A. 1: Linear fits used to determine the initial and volume recombination parameters of the ion recombination correction factor k_s.

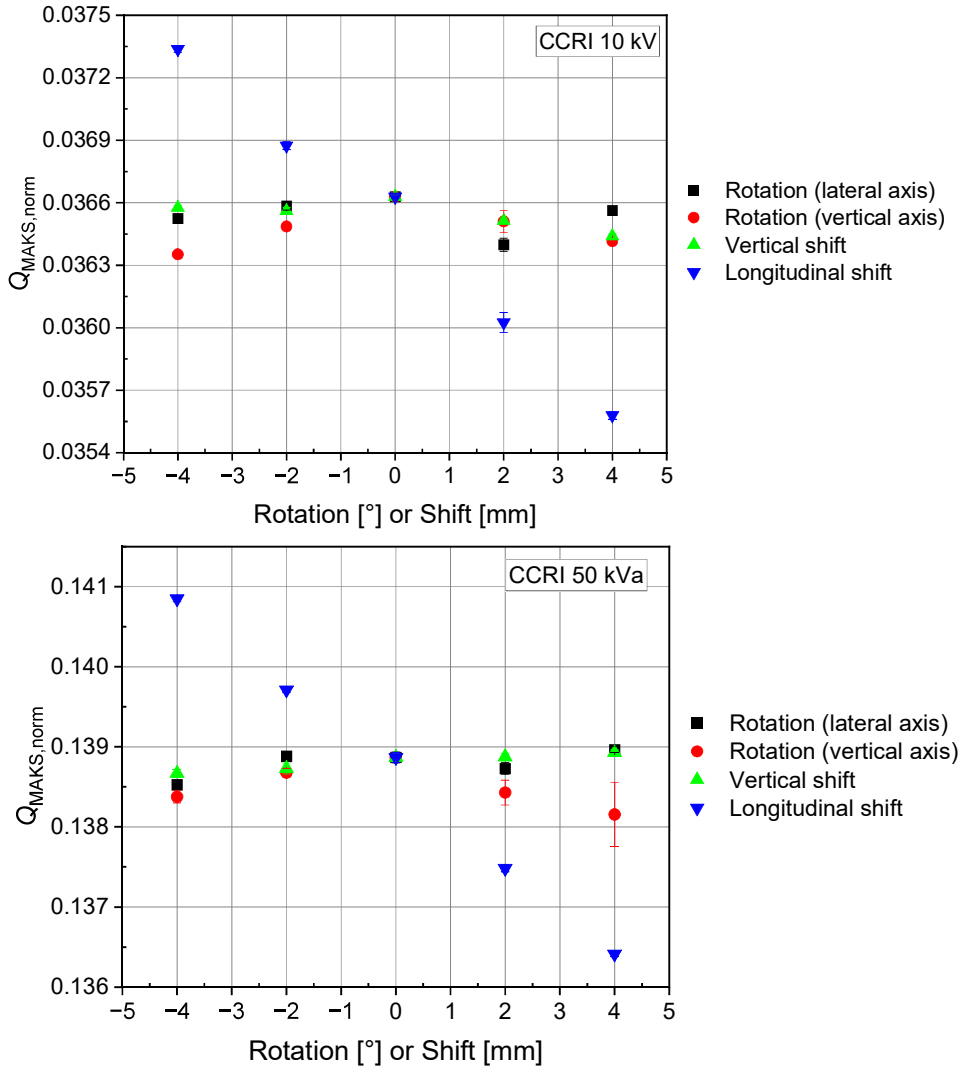

Figure A. 2: Effect of intentional misalignment of MAKS (rotation and shifting) on the measured ionization charge.

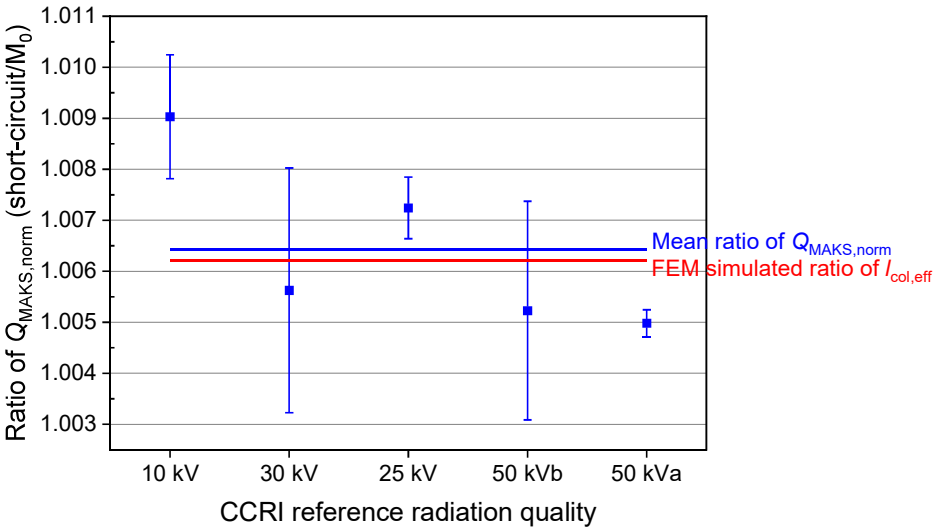

Figure A. 3:Ratios of the ionization charge Q measured with MAKS (normalized to the monitor chamber signal) between the reference setup M_0 and the setup with one resistor of the voltage divider short-circuited. For each CCRI reference radiation quality, the ionization charge with the short-circuited resistor was measured five times; the plotted points represent the mean values, and the error bars indicate the standard deviation. Increased variability between repeated measurements were observed, as the temporary short circuit of the resistor was realized by wrapping a wire around the resistor, which does not ensure a stable electrical contact.

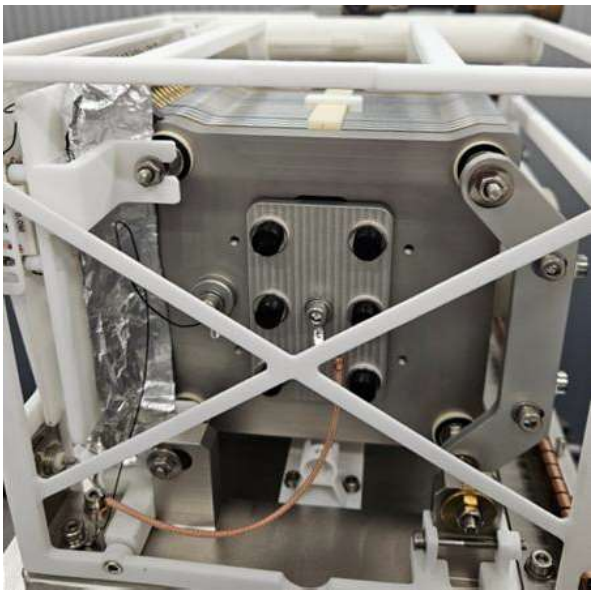

Figure A. 4: Setup to reduce parasitic capacitances by insulation the collecting electrode cable and inserting aluminum foil between guard electrode and the housing.

Metrologia

PAPER • OPEN ACCESS

Free-air ionization chambers for the measurement of air kerma in low-energy x-rays—optimum air path length and the limitations of averaging monoenergetic correction factors

To cite this article: J Gschweng and S Pojtinger 2025 *Metrologia* **62** 025013

View the article online for updates and enhancements.

You may also like

- GHz bursts in MHz burst (BiBurst) enabling high-speed femtosecond laser ablation of silicon due to prevention of air ionization
Kotaro Obata, Francesc Caballero-Lucas, Shota Kawabata et al.
- An analysis of scatter characteristics in x-ray CT spectral correction
Tao Zhang, Zhiqiang Chen, Hao Zhou et al.
- Characterization of a free air ionization chamber for low energy X-rays
N F Silva, M Xavier, V Vivolo et al.

This content was downloaded from IP address 192.53.103.119 on 01/04/2025 at 11:59

OPEN ACCESS
IOP Publishing | Bureau International des Poids et Mesures Metrologia
Metrologia **62** (2025) 025013 (9pp) https://doi.org/10.1088/1681-7575/adc39d

Free-air ionization chambers for the measurement of air kerma in low-energy x-rays—optimum air path length and the limitations of averaging monoenergetic correction factors

J Gschweng[1,2,*] **and S Pojtinger**[1]

[1] Physikalisch-Technische Bundesanstalt (PTB), Braunschweig, Germany
[2] Technische Hochschule Mittelhessen, Gießen, Germany

E-mail: Jessica.Gschweng@ptb.de

Received 10 July 2024, revised 14 March 2025
Accepted for publication 21 March 2025
Published 1 April 2025

Abstract

The German national metrology institute Physikalisch-Technische Bundesanstalt is developing a new primary standard for the realization of the quantity air kerma free-in-air in the x-ray energy range up to 50 keV. National metrology institutes use free-air ionization chambers (FACs) for this purpose. FACs with various geometrical dimensions are used for low-energy x-rays. This study aims to (1) determine the optimum air path length of a FAC, which is the most critical geometric parameter for the low-energy x-ray range, and (2) to evaluate the limitations of averaging monoenergetic correction factors, a method that many institutes use to enable time-saving calculation of spectral correction factors for a larger number of radiation qualities. Monte Carlo simulations were performed to compute monoenergetic and spectral correction factors for air attenuation, photon scattering, inadequate charged particle equilibrium, and diaphragm effects. In addition, spectral correction factors were calculated by averaging the monoenergetic correction factors with different x-ray spectra. The results show that for low-energy FACs the predominant correction is the correction for air attenuation. Thus, it is preferable to have a minimized air path length. The minimization of the air path length is limited by the impact of electrons created by diaphragm interactions and the loss of charged particle equilibrium. If the air attenuation between the aperture and the collecting volume is considered for a 10 kV x-ray spectrum, the averaged and simulated spectral correction factors agree within less than 0.1%.

Keywords: free-air ionization chamber, air kerma, primary standard, correction factors, Monte Carlo simulation

* Author to whom any correspondence should be addressed.

Original content from this work may be used under the terms of the Creative Commons Attribution 4.0 licence. Any further distribution of this work must maintain attribution to the author(s) and the title of the work, journal citation and DOI.

 © 2025 The Author(s). Published on behalf of BIPM by IOP Publishing Ltd

1. Introduction

Due to the increasing demand for traceable calibrations for the quantity air kerma in the x-ray energy range used for mammography, the German national metrology institute Physikalisch-Technische Bundesanstalt (PTB) is developing a new primary standard for the realization of the quantity air kerma free-in-air in the x-ray energy range up to 50 keV.

Most national metrology institutes (NMIs) use free-air ionization chambers (FACs) as primary standards to realize the quantity air kerma. The prevalent type of FACs is the parallel-plate chamber, as described in detail by Burns and Büermann [1]. X-rays enter the chamber through an entrance diaphragm and interact with the air inside the chamber. Charged particles generated are collected by applying a voltage between two planar parallel electrodes. Considering several correction factors, the air kerma can be calculated from the measured charge. Historically, the geometry-dependent correction factors were determined by measurements [2–6] or calculations [7, 8]. Later, advancements in Monte Carlo simulation methods allowed for the numerical calculation of the correction factors [9–16].

The development of a FAC used as a primary standard in the x-ray energy range used for mammography faces two main challenges. First, low-energy x-rays are subject to substantial air attenuation. The air attenuation depends on the air path length of the FAC, defined as the distance between the reference plane of the diaphragm and the middle of the collecting volume (CV). As shown in table 1, established FACs for low-energy x-rays used by various NMIs have a wide range of air path lengths from 39.02 mm to 110 mm. Consequently, the applied correction factors for air attenuation of the CCRI 10 kV reference radiation quality used in BIPM.RI(I)-K2 key comparisons (CCRI10kV) vary significantly between 5.66% [17] and 26.28% [18]. This variability is remarkable, as one might expect that the air path length in low-energy FACs would have been minimized to minimize the air attenuation, thus reducing sources for potentially large uncertainties.

The second challenge arises from the diversity of mammography devices. Manufacturers continuously develop new anode and filter material combinations, complicating the determination of correction factors for the resulting multitude of radiation qualities. An efficient method for calculating correction factors is necessary, as measuring or simulating each correction factor in extensive Monte Carlo simulations would be too time-consuming. A common approach is to average the simulated monoenergetic correction factors with the distribution of the uncharged-particle fluence with respect to the energy (referred to as x-ray spectrum) of different radiation qualities to determine the spectral correction factors [9, 10, 14–16, 33–35]. However, as Grimbergen [9] explained, this method is an approximation that assumes all correction factors are close to 1. As shown in table 1, the correction factors for air attenuation can be considerably large for FACs used as low-energy primary standards.

Consequently, this work aims to systematically address two main objectives: determining an optimum air path length to minimize air attenuation while keeping other corrections comparatively small and evaluating the limitations of averaging monoenergetic correction factors with the x-ray spectra of low-energy radiation qualities.

Table 1. Air path lengths of the FACs used by national metrology institutes to realize the quantity air kerma for low-energy x-rays. The air path length is defined as the distance between the reference plane and the center of the collecting volume.

Metrology institute	Air path length/mm	$k_{\mathrm{att,CCRI10kV}}$	References
PTB (Germany)	97.2	1.2294	[19]
BIPM	100	1.1956	[19]
ARPANSA (Australia)	85	1.1661	[20]
BEV (Austria)	63.64	1.2081	[21]
BFKH (Hungary)	63.7	1.1017	[22]
CMI (Czech Republic)	100.007	1.1951	[23]
ENEA-INMRI (Italy)	65.12	1.1246	[24]
GUM (Poland)	102.2	1.2079	[25]
KRISS (Korea)	77.0	1.1473	[26]
LNE-LNHB (France)	71.95	1.1372	[27]
NIM (China)	100	1.1759	[28]
NIST (USA)	39.02	1.0721	[29]
NMIJ (Japan)	80	1.1924	[30]
NPL (UK)	88.5	1.1708	[31]
NRC (Canada)	98.9	1.1733	[32]
VNIIM (Russia)	110	1.2628	[18]
VSL (Netherlands)	30.9	1.0566	[17]

2. Methods

To investigate the dependency of the correction factors on the air path length of a FAC, the correction factors were calculated using Monte Carlo simulations with EGSnrc [36]. Table 2 lists the parameters applied for the Monte Carlo simulations.

An adjustable FAC model was created for the Monte Carlo simulations, see figure 1. Two planar parallel electrodes made of graphitized aluminum alloy were placed inside the housing of aluminum and lead. The collecting electrode was spaced 1 mm from the guard electrode. In front of the housing, a 1 mm thick tungsten entrance diaphragm was included. Consistent with values commonly reported in the literature for well-established FACs, the electrode separation was 60 mm, the collecting electrode length was 15 mm, and the aperture diameter was 10 mm. The air path length was systematically varied between 20 and 100 mm. The distance between the x-ray source and the reference plane was 1000 mm. The beam diameter in the reference plane was 12 mm.

The following correction factors were part of this study. The correction factor for air attenuation k_{att} corrects photon attenuation in the air between the reference plane and the CV. The correction factor for photon scattering k_{sc} corrects for charge contributions from secondary photons, such as scattered or fluorescence photons, which were created by interactions with the air inside the FAC. The correction factor for inadequate CPE k_{cpe} corrects for charge losses when the air

Table 2. Description of the parameters applied for the Monte Carlo simulations according to [37].

Parameter	Description	References
Code	EGSnrc release version 2021	[36]
Timing	PTB computing cluster (CPU) Approx. 10^7–10^8 histories per hour	
Cross-sections	mcdf-xcom	
Transport parameters	Electron cutoff 0.512 MeV, photon cutoff 0.001 MeV	
Variance reduction	Photon splitting, Russian Roulette	[38]
Histories	10^9–10^{11} histories per simulation	
Statistical uncertainty	$\leqslant$0.01% k_{cpc} $\leqslant$0.001% others	
Postprocessing	OriginPro 2023b	

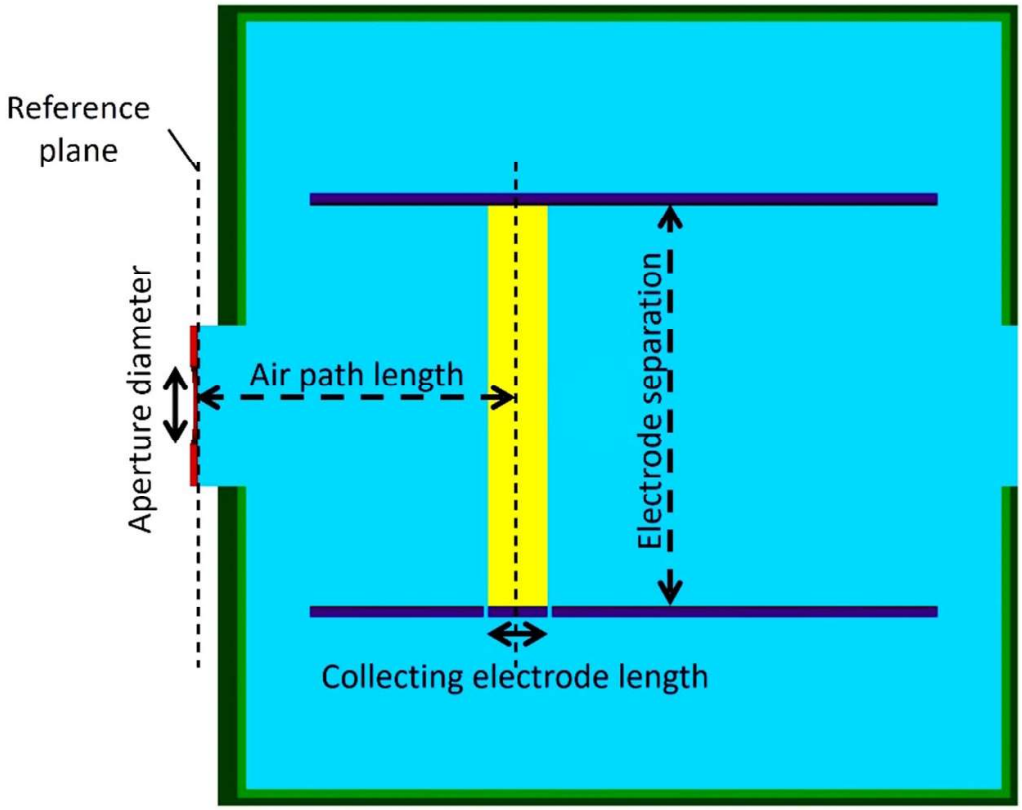

Figure 1. Cross-sectional view of the adjustable Monte Carlo simulation model of a free-air ionization chamber with the most important geometric parameters. The air path length was systematically varied in this study.

path length is insufficiently long to meet the conditions of CPE. The correction factor for diaphragm effects k_{dia} corrects for collected charge resulting from diaphragm interactions. The correction factor for electron loss k_{eloss} corrects for secondary electrons reaching the electrode before fully decelerating. This correction factor is not pertinent to the research question, as it primarily depends on the electrode separation rather than the air path length.

The correction factors k_{att}, k_{sc}, k_{cpe}, and k_{dia} were calculated with the EGSnrc user-code *egs_fac* [39] as follows:

$$k_{dia} = \frac{E1}{Eg}, \tag{1}$$

$$k_{sc} = \frac{E2}{E1}, \tag{2}$$

$$k_{cpe} = \frac{E4}{E3}, \tag{3}$$

$$k_{att} = \frac{E6}{E5}. \tag{4}$$

Eg represents the total energy deposited in the CV. $E1$ signifies the energy deposited excluding the contribution from particles that have interacted with the diaphragm. $E2$ accounts only for the energy deposited by electrons created from primary photons. $E3$ is $E2$ corrected for energy loss or gain through the side faces of the CV and $E4$ corrects additional

Table 3. Filtration of CCRI reference radiation qualities used for BIPM-RI(I)-K2 key comparisons [19].

Radiation quality	CCRI10kV	CCRI30kV	CCRI25kV	CCRI50kVb	CCRI50kVa
Tube potential/kV	10	30	25	50	50
Al filtration/mm	0	0.208	0.372	1.008	3.989

for the energy loss or gain through the front and back face. $E5$ is the computed air kerma in the CV and $E6$ is the computed air kerma at the reference plane.

The total correction factor k_{total} was calculated as the product of the individual correction factors:

$$k_{\text{total}} = k_{\text{att}} k_{\text{sc}} k_{\text{cpe}} k_{\text{dia}}. \tag{5}$$

Each correction factor was calculated as a function of the photon energy, resulting in the monoenergetic correction factors $k_{\text{att,mono}}$, $k_{\text{sc,mono}}$, $k_{\text{cpe,mono}}$, and $k_{\text{dia,mono}}$. For this purpose, Monte Carlo simulations were performed using a monoenergetic, collimated photon beam source. The photon energy was varied within a range of 4 keV–50 keV. Spectral correction factors ($k_{\Phi,\text{sim}}$) were computed by direct Monte Carlo simulation using tabulated *reference x-ray spectra*, created as described below.

In a second step, the spectral correction factors $k_{\Phi,\text{avg}}$ were determined by averaging the monoenergetic correction factors with the x-ray spectra (described below), using the following equation [9]:

$$k_{\Phi,\text{avg}} = \frac{\int k_{\text{mono}}(E) * \mu_{\text{tr}}(E) * E * \Phi(E)\,\mathrm{d}E}{\int \mu_{\text{tr}}(E) * E * \Phi(E)\,\mathrm{d}E}, \tag{6}$$

where k_{mono} is the monoenergetic correction factor, E is the incident photon energy, $\mu_{\text{tr}}(E)$ is the photon energy-transfer coefficient, and $\Phi(E)$ is the x-ray spectrum.

In the following $k_{\text{total},\Phi,\text{sim}}$ and $k_{\text{total},\Phi,\text{avg}}$ are used to differentiate the total correction factor based on the direct simulation using a tabulated x-ray spectrum ($k_{\text{total},\Phi,\text{sim}}$) from the total correction factor calculated based on averaging the monoenergetic correction factors ($k_{\text{total},\Phi,\text{avg}}$).

Three distinct approaches were employed to generate the x-ray spectra for use in equation (6) to evaluate the limitations of averaging monoenergetic correction factors with the x-ray spectra. For all approaches, unfiltered x-ray spectra were measured using spectrometry as described by Ketelhut *et al* [40] but with a source-to-detector distance of 500 mm, the distance between the reference plane and the source for BIPM.RI-K2 key comparisons. In the first approach, the unfiltered x-ray spectra were computationally filtered with the PTB in-house Python module bueSpec [41] to obtain the *reference x-ray spectra* of the CCRI radiation qualities, as listed in table 3. The *reference x-ray spectra* correspond to the reference plane (cf figure 1) and provide a good approximation for the x-ray spectra in the CV, assuming all correction factors are close to unity. However, the spectrum in the CV is attenuated between the reference plane and the CV. Therefore, in the second approach, *air-filtered x-ray spectra* were created by computationally filtering the *reference x-ray spectra* with an air layer whose thickness corresponded to the air path length. In addition to the attenuation, the x-ray spectra in the CV contain contributions of scattered and fluorescence photons. In the third approach, to account for these effects, the EGSnrc user code *egs_kerma* was employed to obtain the *simulated x-ray spectra* in the CV from the *reference x-ray spectra* by Monte Carlo simulations. The same simulation geometry described above (figure 1) was used for these simulations.

3. Results

The following results address the two main objectives of this study, focusing on the dependence of air attenuation on the air path length of a low-energy FAC and the evaluation of averaging monoenergetic correction factors with low-energy x-ray spectra.

3.1. Simulation of monoenergetic correction factors

The study systematically investigated the influence of the air path length of the FAC on the monoenergetic correction factors $k_{\text{att,mono}}$, $k_{\text{sc,mono}}$, $k_{\text{cpe,mono}}$, and $k_{\text{dia,mono}}$. The results are shown in figure 2, where the monoenergetic correction factors are presented as a function of the photon energy for different air path lengths of the FAC.

Figure 2(a) shows the values of $k_{\text{att,mono}}$. These values are always larger than one because the air attenuation decreases the energy deposited in the CV. For energies above 25 keV, the values of $k_{\text{att,mono}}$ remained between 1.0 and 1.005 across all air path lengths. At photon energies below 25 keV, the exponential decrease of $k_{\text{att,mono}}$ was more pronounced for longer air path lengths. For instance, at 10 keV, shortening the air path length by 10 mm decreased the correction for air attenuation by approximately 0.6%, while at 5 keV it was 6% per 10 mm.

Figure 2(b) shows the values of $k_{\text{sc,mono}}$. These values are always smaller than one because scatter increases the energy deposited in the CV. With smaller air path lengths, the values of $k_{\text{sc,mono}}$ were closer to 1. However, this trend did not hold for an air path length of 20 mm. At photon energies exceeding 35 keV, the impact of scattered photons was more pronounced for the 20 mm air path length compared to longer air path lengths.

The correction factors $k_{\text{cpe,mono}}$ and $k_{\text{dia,mono}}$ were near unity for lower energies before significantly increasing ($k_{\text{cpe,mono}}$) or decreasing ($k_{\text{dia,mono}}$). As depicted in figures 2(c) and (d), a shorter air path length resulted in lower energy thresholds for

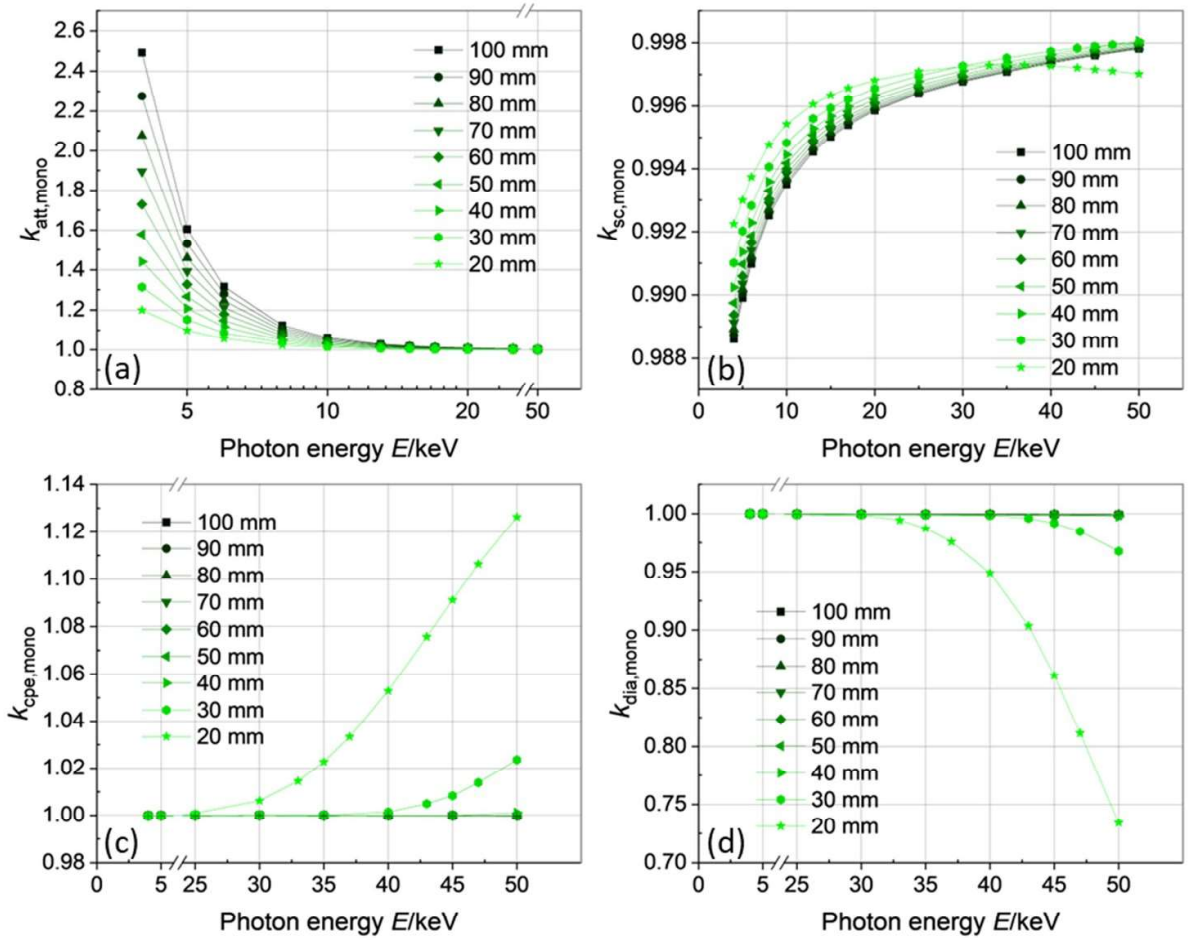

Figure 2. Correction factors $k_{att,mono}$ (a), $k_{sc,mono}$ (b), $k_{cpe,mono}$ (c), and $k_{dia,mono}$ (d) as a function of the photon energy for a free-air ionization chamber with varied air path length.

these changes in slope. The decrease in $k_{dia,mono}$ occurred at slightly higher energies than the increase in $k_{cpe,mono}$ but the decrease in $k_{dia,mono}$ was steeper. For example, for a 20 mm air path length, $k_{cpe,mono}$ started increasing at 25 keV, and $k_{dia,mono}$ started decreasing at 30 keV. At 50 keV, the corrections were 13% ($k_{cpe,mono}$) and 27% ($k_{dia,mono}$) for the 20 mm air path length.

3.2. Simulation of spectral correction factors

To investigate the impact of reducing the air path length on the total correction factor for a realistic x-ray beam, Monte Carlo simulations were conducted using EGSnrc with imported *reference x-ray spectra*. Figure 3 illustrates the calculated values of $k_{total,\Phi,sim}$ as a function of the air path length. The total correction factors for CCRI10kV, CCRI30kV, and CCRI25kV radiation qualities were greater than 1 and increased evenly with longer air path lengths. This trend was also observed for air path lengths from 30 mm to 100 mm for CCRI50kVb and CCRI50a radiation qualities. Notably, $k_{total,\Phi,sim}$ was significantly lower at the shorter air path length of 20 mm, with values of 0.995 94 (CCRI50kVb) and 0.989 89 (CCRI50kVa).

3.3. Averaging monoenergetic correction factors with x-ray spectra

In addition to the simulations, the spectral correction factors were calculated by averaging the monoenergetic correction factors with x-ray spectra. The study examined the use of three differently created x-ray spectra. To assess how well the averaging worked with the respective x-ray spectra, the averaged total correction factors $k_{total,\Phi,avg}$ were compared with the simulated total correction factors $k_{total,\Phi,sim}$.

Figure 4 shows the ratio between the averaged and simulated total correction factors as a function of the simulated total correction. When the *reference x-ray spectra* were used, the larger the total corrections, the greater the differences between averaging and simulation. The difference exceeded 0.1% when the value of $k_{total,\Phi,sim}$ surpassed 1.04 and continued to increase for higher values of $k_{total,\Phi,sim}$, reaching a peak of 1.17%. When using the *simulated x-ray spectra* or the *air-filtered x-ray spectra* for averaging, the difference between $k_{total,\Phi,sim}$ and $k_{total,\Phi,avg}$ was significantly reduced. The difference remained below 0.1% even for the largest $k_{total,\Phi,sim}$ of 1.215. However, figure 4 shows two outliers, where the difference was comparatively large and consistent across all three

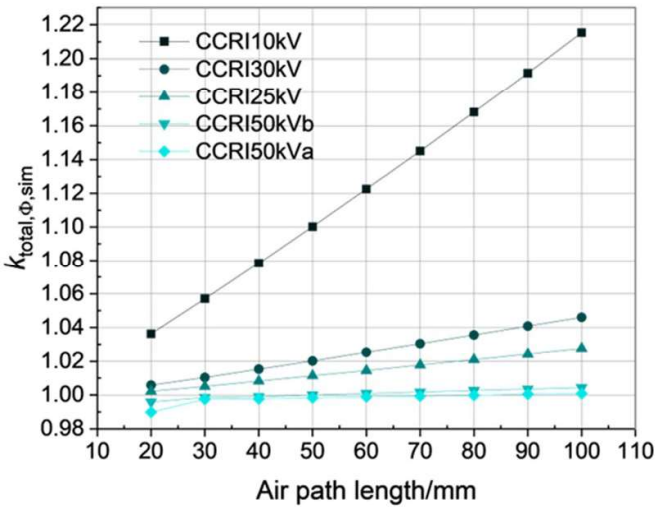

Figure 3. Total simulated correction factor $k_{total,\Phi,sim}$ as a function of the air path length of a free-air ionization chamber for CCRI reference qualities.

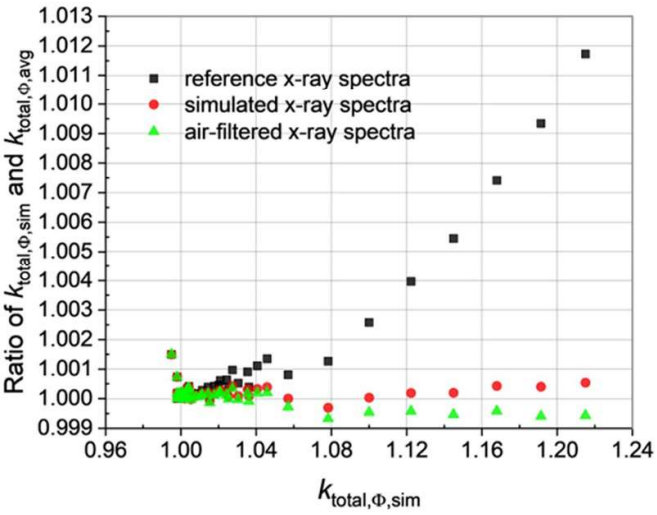

Figure 4. Ratio of the total simulated correction factors $k_{total,\Phi,sim}$ and the total averaged correction factors $k_{total,\Phi,avg}$ as a function of $k_{total,\Phi,sim}$. Three different x-ray spectra were used for averaging monoenergetic correction factors.

x-ray spectra. These two outliers correspond to the total corrections determined for the 50 kV radiation qualities and an air path length of 20 mm.

4. Discussion

This study systematically investigated the minimization of the air path length, which is the most critical geometric parameter for FACs used as primary standards in the low x-ray energy range. The dependencies between air path length and simulated monoenergetic and simulated spectral correction factors were analyzed. In addition, the applicability of the method of averaging monoenergetic correction factors with low-energy x-ray spectra to obtain the spectral correction factors was evaluated.

4.1. Analysis of monoenergetic correction factors

The variation of the air path length significantly influenced $k_{att,mono}$ at photon energies below 25 keV. Shortening the air path length by a few centimeters reduced the correction for air attenuation in the percentage range. However, changing the air path length also affects other correction factors. Consistent with early studies from Takata and Sakihara [7], the influence of scattered photons decreased as the air path length shortened. The results align with previous findings by Somerwil [3], indicating a difference of less than 2 ‰ scatter correction for a 60 mm change in the air path length. However, an air path length of 20 mm showed a different dependency. The required correction for photon scattering at photon energies above 35 keV and 20 mm of air path length was greater than at longer air path lengths. This is due to the gap of only 1 mm between the inside of the front wall and the front face of the CV, which resulted in collecting the electrons created within the FAC wall by backscattered photons.

The observed steep increases in $k_{cpe,mono}$ at higher energies showed that CPE is no longer achieved for an air path length of less than 40 mm. This is consistent with the continuous slowing down approximation range of the secondary electrons, which is 41 mm for 50 keV electrons [1]. The steep decrease in the values of $k_{dia,mono}$ at high energies and short air path lengths is due to electrons created in the diaphragm and reaching the CV. A minimum of 40 mm of air path length is necessary to prevent diaphragm electrons from reaching the CV in the photon energy range up to 50 keV. Burns and Kessler [13] introduced the correction factor k_{del} as part of k_{dia} for these diaphragm electrons. Their assumption that k_{del} might depend on the chamber dimension was confirmed by these findings. The investigation revealed that both k_{cpe} and k_{dia} limit the minimization of the air path length to 40 mm.

When a FAC is used as a primary standard, it is crucial to determine the correction factors and to quantify the associated uncertainties. This study assumes an ideal geometry for the FAC in the Monte Carlo simulation, resulting in the statistical uncertainty (cf table 2) of the simulation being the primary source of uncertainty for the monoenergetic correction factors. However, for real FACs, manufacturing imprecisions contribute to the uncertainties. After manufacturing, the FAC should be measured with high precision. The measurement uncertainty can then be used to derive the uncertainty of the correction factors. Using the data in figure 2 as an example, the process can be illustrated as follows: Assuming that the air path length was measured with an uncertainty of one-hundredth of a millimeter and the resulting value is 40 mm. Therefore, the true value for the air path length would be between 39.99 mm and 40.01 mm. The correction factors corresponding to these dimensions can be derived from the values in the graphs of figure 2, for instance, by employing a fit function. In a conservative estimate, these values can be used as the limits of a rectangular distribution, which can then be converted into a standard uncertainty according to the ISO Guide to the Expression of Uncertainty in Measurement [42]. For this example, a conservative estimate yields a standard uncertainty contribution of 0.005% for $k_{att,mono}$ and less than 0.001% for

$k_{cpe,mono}$, $k_{dia,mono}$ and $k_{sc,mono}$. Another contribution to uncertainty arises from the mass energy-absorption coefficients. As demonstrated by Stasko and Culberson [16], a comparison between using *xcom* and *mcdf-xcom* photon cross-sections can be employed to estimate a type B uncertainty for the simulated correction factors.

In addition to the energy-dependent correction factors, it is important to consider the impact of the air path length on the electric field distortion. With a longer air path length, the distance between the grounded housing of the FAC and the collecting electrode is longer, and the guard electrode is wider. This reduces the electric field distortion. Given this opposite dependency compared to the dependency between the air path length and k_{att}, further investigation is needed.

4.2. Analysis of spectral correction factors

From the monoenergetic correction factors discussed before, a minimized air path length is desirable for FACs used for photon energies up to 50 keV to minimize k_{att}. Nevertheless, the air path length should be at least 40 mm to ensure that the conditions of CPE are met and to prevent diaphragm electrons from reaching the CV. However, real photon beams are not monoenergetic. Monte Carlo simulations with tabulated x-ray spectra revealed that the total correction can be substantially reduced by minimizing the air path length. Specifically, for the CCRI10kV radiation quality, the reduction of corrections exceeded 15%. This is in line with the data in table 1, which shows that low-energy FACs from various metrology institutes, such as PTB, BIPM, CMI, GUM, NIM, and NRC, have air path lengths of approximately 100 mm and apply 17%–23% correction for air attenuation. If these air path lengths were shortened to 30 mm–40 mm, the required correction could be decreased to 5%–8%, as observed with the FACs from NIST and VSL.

The simulations also showed that for the CCRI50kV radiation qualities, the minimization is limited to 30 mm. Below this length, the total correction factor was less than 1, showing the influence of k_{dia}. The impact of k_{cpe}, on the other hand, was not evident in the total correction factor for the tested radiation qualities, as it was subordinate to k_{dia}.

4.3. Limitations of averaging monoenergetic correction factors with x-ray spectra

In practice, there are several methods available for measuring k_{att}. For instance, the displacement method of the diaphragm or a reduced air pressure pipe can be used to measure air attenuation, as described in more detail by Burns and Büermann [1]. While measurements are time-consuming, this presents a challenge. PTB offers a variety of anode and filter material combinations for the calibration of dosimeters in the energy range used in mammography. Measuring the correction factor for air attenuation in each combination would be overly time-consuming. A more efficient, commonly used approach is to derive the spectral correction factors for different radiation qualities by averaging the monoenergetic correction factors with an x-ray spectrum, see equation (6). However, as described by Grimbergen [9], this equation is an approximation on the condition that all correction factors are near unity. To investigate the applicability of this method in the low-energy x-ray range, the averaged spectral correction factors were compared with the simulated spectral correction factors. The use of three different x-ray spectra for averaging was analyzed.

The comparison when the *reference x-ray spectra* were used for averaging, revealed that the greater the total correction, the more significant the difference between averaged and simulated correction factors. With air attenuation corrections of approximately 20%, anticipated for a FAC with 100 mm air path length and the CCRI10kV radiation quality, a difference of 1.15% would be expected. With an air path length between 30 mm and 40 mm, the difference between simulated and averaged spectral correction factors was less than 0.2%. The difference observed at energies below 10 kV is attributed to significant differences between the x-ray spectra in the reference plane and at the CV. As the air path length increased, the spectral differences became more pronounced, making the *reference x-ray spectra* less suitable for averaging with the monoenergetic correction factors to derive the spectral correction factors. Using the *reference x-ray spectra* for averaging as an approximation for the spectra in the CV only works if the air path length is minimized accordingly.

The study showed that when the *simulated x-ray spectra*, calculated for the CV by Monte Carlo simulations, were used, averaging represents a valid method to calculate the spectral correction factors from the monoenergetic correction factors. Furthermore, this study proved by using the *air-filtered x-ray spectra* for averaging that the main reason for the change in the spectra between the reference plane and the CV comes from air attenuation. Therefore, the spectrum in the CV does not need to be calculated by Monte Carlo simulations. If the spectrum in the reference plane is known, it is sufficient to computationally filter the spectrum with an air layer as thick as the air path length to correctly calculate the spectral correction factors by the averaging method. The outliers observed in figure 4 correspond to the total corrections for CCRI50kV radiation qualities and an air path length of the FAC of 20 mm. In these cases, there is inadequate CPE, and the diaphragm electrons reach the CV. These effects are unrelated to the x-ray spectra, which is why the observed difference between simulated and averaged spectral correction factors remained the same for the three x-ray spectra tested. This again shows that the described averaging approach is based on the assumption that all correction factors are nearly unity.

The calculation of k_{att} is constrained by the underlying attenuation coefficients. The rapid increase in attenuation coefficients at low energies means that minor errors in a tabulated x-ray spectrum can significantly impact Monte Carlo simulation results. For example, we observed small but present differences between simulated and averaged correction factors using *simulated* and *air-filtered x-ray spectra*, which increased with the total corrections. This may be attributed to the x-ray spectra being cut off at 4 keV while the *egs_fac* simulations employed a photon cutoff of 1 keV. Furthermore, during this study, it became clear that the averaging method is also limited

by the resolution of the monoenergetic correction factors. For averaging, it was necessary to simulate and apply the monoenergetic correction factors in 0.25 keV steps below 10 keV to produce the results shown above. When monoenergetic correction factors were applied only in 1 keV steps, the observed difference between averaged and simulated spectral correction factors was up to 1.5% higher than shown in figure 4. The larger the total correction, the greater the limitation due to the resolution of the monoenergetic correction factors. These points highlight the importance of maintaining correction factors as small as possible to minimize potential errors.

5. Conclusion

This study systematically investigated the dependency between the air path length of low-energy FAC standards and their correction factors using Monte Carlo simulations. The results provide a useful data set of the dependencies between the air path length and the correction factors for air attenuation, photon scattering, inadequate CPE, and diaphragm effects. The results in this study confirm that the air attenuation corrections, partly exceeding 20% for the CCRI10kV radiation quality for established FACs from different NMIs, can be significantly reduced by minimizing the air path length. This is desirable for a FAC to operate as a primary standard in the low-energy range, as it reduces the sources for potentially large uncertainties. However, minimizing the air path length of a low-energy FAC in favor of the air attenuation is limited, predominantly by the correction for diaphragm effects rather than the correction for inadequate CPE. The air path length should be at least 45 mm to ensure that electrons produced by the interaction of a 50 keV photon with the diaphragm do not reach the CV.

This study confirms that computing spectral correction factors by averaging monoenergetic correction factors with an x-ray spectrum is a beneficial technique to avoid time-intensive measurements. Nevertheless, this approach necessitates a FAC geometry where the required correction factors are minimal and demands a strong comprehension of the associated limitations. In particular, using a suitable x-ray spectrum for averaging is essential.

ORCID iDs

J Gschweng https://orcid.org/0009-0001-0834-6626
S Pojtinger https://orcid.org/0000-0001-6397-4572

References

[1] Burns D T and Büermann L 2009 Free-air ionization chambers *Metrologia* **46** S9
[2] Attix F H and DeLaVergne L 1954 Plate separation requirements for standard free-air ionization chambers *Radiology* **63** 853–66
[3] Somerwil A 1972 Influence of beam path length in standard free air chambers on the photon scatter correction in low energy X-radiation measurements *Metrologia* **8** 42
[4] Engelke B-A, Oetzmann W and Struppek G 1988 *Die Messeinrichtungen der Physikalisch-Technischen Bundesanstalt zur Darstellung der Einheiten der Standard-Ionendosis, Photonen-Aquivalentdosis und Luftkerma* Physikalisch-Technische Bundesanstalt
[5] Wyckoff H O and Attix F H 1957 *Design of Free-air Ionization Chambers* vol 64 (US Government Printing Office)
[6] Allisy A and Roux M A M 1961 Contribution a la Mesure des Rayons Roentgen dans le Domaine de 5 a 50 kV *Acta Radiol.* **os-55** 57–74
[7] Takata N and Sakihara K 1985 Effects of scattered x-rays and fluorescences on exposure measured with a free-air ionisation chamber *Radiat. Prot. Dosim.* **11** 53–56
[8] Lamperti P J and O'Brien M 2001 *NIST Measurement Services: Calibration of X-ray and Gamma-Ray Measuring Instruments* (NIST Special Publication) pp 250–8
[9] Grimbergen T W M, van Dijk E and de Vries W 1998 Correction factors for the NMi free-air ionization chamber for medium-energy x-rays calculated with the Monte Carlo method *Phys. Med. Biol.* **43** 3207
[10] Lin U-T and Chu C-H 2006 Correction factors for the INER-improved free-air ionization chambers calculated with the Monte Carlo method *Appl. Radiat. Isot.* **64** 608–14
[11] Kurosawa T and Takata N 2005 Estimation of electron-loss and photon-scattering corrections for parallel-plate free-air chambers *J. Nucl. Sci. Technol.* **42** 1077–80
[12] Burns D 2001 Free-air chamber correction factors for electron loss, photon scatter, fluorescence and bremsstrahlung (CCRI) pp 01–36
[13] Burns D and Kessler C 2009 Diaphragm correction factors for free-air chamber standards for air kerma in x-rays *Phys. Med. Biol.* **54** 2737–45
[14] Büermann L 2021 *The PTB free-air ionization chambers* Physikalisch-Technische Bundesanstalt (https://doi.org/10.7795/120.20220324)
[15] Lye J E, Butler D J and Webb D V 2009 Monte Carlo correction factors for the ARPANSA kilovoltage free-air chambers and the effect of moving the limiting aperture *Metrologia* **47** 11
[16] Stasko J T and Culberson W S 2025 Attix free-air chamber correction factors computed using EGSnrc *Med. Phys.* (https://doi.org/10.1002/mp.17629)
[17] Burns D T, Kessler C, de Prez L and Joulaeizadeh L 2014 Key comparison BIPM.RI(I)-K2 of the air-kerma standards of the VSL, Netherlands and the BIPM in low-energy x-rays *Metrologia* **51** 06010
[18] Burns D T, Roger P, Villevalde A Y and Oborin A V 2012 Key comparison BIPM.RI(I)-K2 of the air-kerma standards of the VNIIM, Russian Federation and the BIPM in low-energy x-rays *Metrologia* **49** 06003
[19] Burns D T, Kessler C and Pojtinger S 2024 Key comparison BIPM.RI(I)-K2 of the air-kerma standards of the PTB, Germany, and the BIPM in low-energy x-rays *Metrologia* **61** 06016
[20] Burns D T, Kessler C, Butler D, Shoyookhi S and Hanlon M 2022 Key comparison BIPM.RI(I)-K2 of the air-kerma standards of the ARPANSA, Australia, and the BIPM in low-energy x-rays *Metrologia* **59** 06022
[21] Burns D T, Kessler C, Steurer A, Tiefenboeck W and Bauer M 2015 Key comparison BIPM.RI(I)-K2 of the air-kerma standards of the BEV, Austria and the BIPM in low-energy x-rays *Metrologia* **52** 06001
[22] Burns D T, Kessler C and Finta V 2023 Key comparison BIPM.RI(I)-K2 of the air-kerma standards of the BFKH, Hungary, and the BIPM in low-energy x-rays *Metrologia* **60** 06016

[23] Burns D T, Kessler C and Sochor V 2016 Key comparison BIPM.RI(I)-K2 of the air-kerma standards of the CMI, Czech Republic and the BIPM in low-energy x-rays *Metrologia* **53** 06009
[24] Burns D T, Kessler C, Roger P, Toni M P, Pinto M, Bovi M, Cappadozzi G and Silvestri C 2011 Key comparison BIPM.RI(I)-K2 of the air-kerma standards of the ENEA-INMRI, Italy and the BIPM in low-energy x-rays *Metrologia* **48** 06010
[25] Burns D T, Kessler C and Michalik Ł 2022 Key comparison BIPM.RI(I)-K2 of the air-kerma standards of the GUM, Poland, and the BIPM in low-energy x-rays *Metrologia* **59** 06014
[26] Burns D T, Kessler C, Yi C-Y and Kim Y H 2022 Key comparison BIPM.RI(I)-K2 of the air-kerma standards of the KRISS, Republic of Korea, and the BIPM in low-energy x-rays *Metrologia* **59** 06011
[27] Burns D T, Roger P, Denozière M and Leroy E 2011 Key comparison BIPM.RI(I)-K2 of the air-kerma standards of the LNE–LNHB, France and the BIPM in low-energy x-rays *Metrologia* **48** 06013
[28] Burns D T, Kessler C, Jinjie W and Peiwei W 2019 Key comparison BIPM.RI(I)-K2 of the air-kerma standards of the NIM, China, and the BIPM in low-energy x-rays *Metrologia* **56** 06006
[29] Burns D T, Lamperti P J and O'Brien M 1999 Comparison of the air kerma standards of the NIST and the BIPM in the low-energy x-ray range
[30] Burns D T, Kessler C, Tanaka T, Kurosawa T and Saito N 2015 Key comparison BIPM.RI(I)-K2 of the air-kerma standards of the NMIJ, Japan and the BIPM in low-energy x-rays *Metrologia* **52** 06008
[31] Burns D T, Kessler C, Kelly M, Maughan D J and Sander T 2019 Key comparison BIPM.RI(I)-K2 of the air-kerma standards of the NPL, UK, and the BIPM in low-energy x-rays *Metrologia* **56** 06004
[32] Burns D T, Kessler C, Mainegra-Hing E, Shen H and McEwen M R 2019 Key comparison BIPM.RI(I)-K2 of the air-kerma standards of the NRC, Canada, and the BIPM in low-energy x-rays *Metrologia* **56** 06002
[33] Kessler C, Burns D T, Roger P and Allisy-Roberts P J 2010 Establishment of reference radiation qualities for mammography at the BIPM
[34] Kessler C 2013 Développement et mise en place au BIPM d'un systéme international de comparaison et d'étalonnage pour la dosimétrie en mammographie
[35] Rindhatayathon P, Koonkana K and Pungkun V 2021 Development of the primary standard for low-energy and W/Mo mammography x-rays at OAP, Thailand *Metrologia* **58** 055009
[36] Kawrakow I and Rogers D 2000 The EGSnrc code system *NRC Report PIRS-701* (NRC) p 17
[37] Sechopoulos I, Rogers D W O, Bazalova-Carter M, Bolch W E, Heath E C, McNitt-Gray M F, Sempau J and Williamson J F 2018 RECORDS: improved reporting of montE CarlO RaDiation transport studies: report of the AAPM Research Committee Task Group 268 *Med. Phys.* **45** e1–5
[38] Kawrakow I and Fippel M 2000 Investigation of variance reduction techniques for Monte Carlo photon dose calculation using XVMC *Phys. Med. Biol.* **45** 2163
[39] Mainegra-Hing E, Reynaert N and Kawrakow I 2008 Novel approach for the Monte Carlo calculation of free-air chamber correction factors *Med. Phys.* **35** 3650–60
[40] Ketelhut S, Büermann L and Hilgers G 2021 Catalog of x-ray spectra of Mo-, Rh-, and W-anode-based x-ray tubes from 10 to 50 kV *Phys. Med. Biol.* **66** 115013
[41] Pojtinger S 2024 On the robustness of detective quantum efficiency within the limits of IEC 61267 RQA standard radiation qualities *Radiat. Prot. Dosim.* **200** 515–22
[42] Joint Committee for Guides in Metrology 2008 Evaluation of measurement data—guide to the expression of uncertainty in measurement (JCGM)

PAPER • OPEN ACCESS

Development of the new PTB air kerma primary standard—optimization of the geometry for minimal electric field distortions and assessment of the associated uncertainties using the finite element method

To cite this article: J Gschweng and S Pojtinger 2025 *Metrologia* **62** 055002

View the article online for updates and enhancements.

You may also like

- CHIANTI—An Atomic Database for Emission Lines. XVII. Version 10.1: Revised Ionization and Recombination Rates and Other Updates
Kenneth P. Dere, G. Del Zanna, P. R. Young et al.
- The Roles of Fluid Hydrodynamics, Mass Transfer, Rust Layer and Macro-Cell Current on Flow Accelerated Corrosion of Carbon Steel in Oxygen Containing Electrolyte
Liang Liu, Yunze Xu, Yesen Zhu et al.
- Electron-impact ionization of Si IV–VIII in hot plasmas
Jean-Christophe Pain and Djamel Benredjem

This content was downloaded from IP address 192.53.103.119 on 19/01/2026 at 08:17

OPEN ACCESS
IOP Publishing | Bureau International des Poids et Mesures Metrologia
Metrologia **62** (2025) 055002 (11pp) https://doi.org/10.1088/1681-7575/ae033e

Development of the new PTB air kerma primary standard—optimization of the geometry for minimal electric field distortions and assessment of the associated uncertainties using the finite element method

J Gschweng[1,2,*] **and S Pojtinger**[1]

[1] Physikalisch-Technische Bundesanstalt (PTB), Braunschweig, Germany
[2] Technische Hochschule Mittelhessen, Gießen, Germany

E-mail: Jessica.Gschweng@ptb.de

Received 4 June 2025, revised 19 August 2025
Accepted for publication 4 September 2025
Published 17 September 2025

Abstract

The German national metrology institute, Physikalisch-Technische Bundesanstalt (PTB), currently develops a new free-air ionization chamber (FAC) for use as a primary standard for realizing the unit of the air kerma free-in-air. The aim of this study was to optimize the FAC geometry to minimize electric field distortions and to analyze how engineering tolerances affect the uncertainty of the electric field correction factor. We simulated the electric field in the FAC using finite element method simulations and systematically varied the geometry of the FAC. The results of this study invalidated the common conclusion in the literature, that applying half the high-voltage potential to the housing of the FAC minimizes electric field distortions. Instead, we present two novel approaches for reducing electric field distortions by modifying the geometry of the FAC that yielded to an optimal geometry for the new PTB primary standard. The uncertainty of the resulting correction factors for electric field distortion was quantified as 0.04% by considering the engineering tolerances of the FAC.

Keywords: free-air ionization chamber, primary standard, correction factor, electric field distortion, finite element method

* Author to whom any correspondence should be addressed.

Original content from this work may be used under the terms of the Creative Commons Attribution 4.0 licence. Any further distribution of this work must maintain attribution to the author(s) and the title of the work, journal citation and DOI.

 © 2025 The Author(s). Published on behalf of BIPM by IOP Publishing Ltd

1. Introduction

Accurate radiation dose measurements are essential in various fields, including radiation protection, quality assurance of x-ray systems, and patient dose monitoring in diagnostic radiology. Ensuring that dosimeters measuring the air kerma provide reliable and comparable results requires traceability to primary standards. Such traceability ensures consistent dose measurements across laboratories and clinical x-ray systems. Free-air ionization chambers (FACs) are used as primary standards for the realization of the unit of the air kerma free-in-air.

As a result of the significantly increased demand for traceable calibrations in the low-energy x-ray range of mammography, the German national metrology institute Physikalisch-Technische Bundesanstalt (PTB) is currently developing a new FAC to be used as a primary standard in the energy range up to 50 keV. The most common design used for FAC standards is the parallel plate chamber described by Burns and Büermann [1]. This chamber typically consists of a grounded housing with two planar parallel electrodes inside. Ion pairs created by the interactions of x-rays with the air inside the FAC are detected by applying a high voltage that generates an electric field between the electrodes. The air kerma is derived from the collected charge per unit mass of air. Therefore, accurate knowledge of the collecting volume of the FAC is essential.

If the electric field is uniform, the collecting volume is a cylinder defined by the aperture diameter and electrode length. For a non-uniform electric field, the electric field lines ending in the collecting electrode define the collecting volume. The impact of deviations in the collecting volume on the measured charge caused by a non-uniform electric field (electric field distortions) is corrected using the correction factor k_{d}. For example, for the PK100, one of the well-established FACs from PTB, k_{d} is 0.9910 [2].

Several methods have been used to investigate the electric field within FACs. Kemp *et al* [3] measured ionization currents with the housing grounded and at high voltage to estimate the electric field distortion. Miller and Kennedy [4] developed a two-dimensional (2D) analog of a FAC to measure the electric field distortion. Boag [5] concluded from 2D mathematical calculations that engineering tolerances in the construction of the FAC can have a significant impact on the electric field distortion. Uotila [6] subsequently confirmed this finding for a three-dimensional (3D) case. Numerical simulations using the finite element method (FEM) for 2D [7–10] or 3D [11, 12] models have enabled more detailed examinations of the electric field uniformity. However, these studies have certain limitations.

It has been suggested by several authors [7, 11, 12] that applying an electric potential equal to half the applied high-voltage potential of the FAC to the housing is an effective method for reducing electric field distortions. This study investigated this approach but could not validate it. Consequently, an alternative method to minimize electric field distortions inside the FAC was needed.

Therefore, we systematically analyzed the influence of the geometry of the FAC on the electric field. The studies mentioned above each focused on a fixed FAC design. Based on these studies, it was not possible to make a reliable statement about the influence of different choices in the FAC design on the electric field. In this work, we investigated a variable FAC model. This model was used to investigate the various possibilities for the geometry of the FAC by systematically varying its dimensions and calculating the associated effects on the electric field. The aim was to find an optimum FAC geometry with minimal electric field distortion for the new FAC of the PTB.

Furthermore, existing literature lacks analyses examining the impact of engineering tolerances on the uncertainty of electric field distortions using FEM. However, this information is needed for the construction of the new primary standard of the PTB. We have addressed this gap by systematically varying individual components of the FAC down to the micrometer level and quantitatively assessing their respective contributions to the uncertainty.

In order to find the optimal design for the new PTB primary standard, this study aims to address three key research objectives: (1) investigate the uniformity of the electric field when half of the FAC potential is applied to the housing, (2) analyze the dependence between the FAC geometry and the electric field distortion, and (3) quantify the uncertainty contribution arising from engineering tolerances.

2. Methods

2.1. Geometric models

Two simplified computer-aided design (CAD) models of a FAC were created using SOLIDWORKS 2022 for the FEM simulations. One of these models represents the PK100, a FAC currently utilized at PTB as a primary standard for the realization of the unit of the air-kerma free-in-air, as described by Burns and Büermann [1]. The PK100 is a parallel plate FAC that employs a system of guard wires to create a uniform electric field. The PK100 was used to validate the use of the FEM simulations as described by Gschweng and Pojtinger [13]. Changes in the air kerma measured with the PK100 due to a controlled alteration of the electric field were compared to the change in the FEM-simulated collecting volumes. The alteration of the electric field was achieved by shorting a resistor of the voltage divider of the guard wire system.

The second model ($\mathrm{FAC_{flex}}$) consisted of a housing, a guard electrode, a collecting electrode, a high-voltage electrode, and guard rings. The geometric parameters that potentially impact the electric field within the $\mathrm{FAC_{flex}}$ are shown in figure 1. Namely, these are the distance from the guard rings to the middle of the collecting electrode a, the guard ring width w, the cutout diameter in the guard rings d, the distance from the guard rings to the housing h, the collecting electrode length l, the electrode separation s, the guard ring thickness t and the gap between the guard rings g.

Initial dimensions were based on established low-energy FAC designs (see table 1). The present study investigated the impact of varying these geometric parameters within the ranges indicated in table 1 on the electric field distortion of the

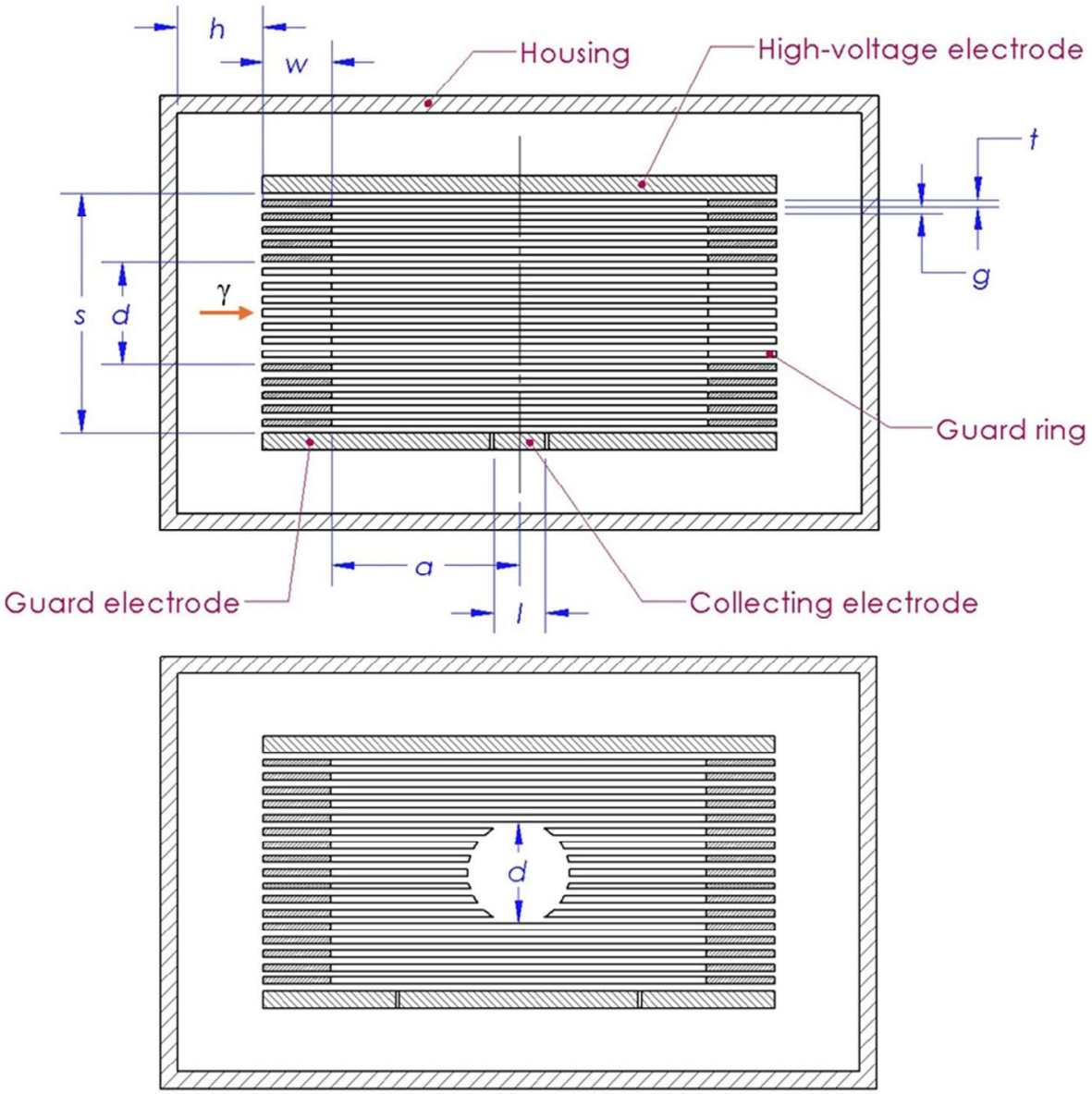

Figure 1. Simplified technical drawing of the FAC_{flex} showing cross-sections along (top) and transverse to (bottom) the beam axis.

Table 1. Geometric parameters of the FAC_{flex}.

Geometric parameter	Description	Initial dimension (mm)	Variation range (mm)	Selected dimension (mm)
a	Distance guard rings to middle of collecting electrode	55	45–80	40
w	Guard ring width	20	10–30	15
d	Cutout diameter in the guard rings	30	20–40	30
h	Distance guard rings to housing	25	5–30	25
l	Collecting electrode length	15	5–25	15
s	Electrode separation	70	54–86	62
t	Guard ring thickness	2	1.091–3.667	2
g	Gap between the guard rings	2	1–2.8	2

FAC_{flex}, while keeping the other parameters constant at their initial dimensions. The FAC model with the initial dimensions was also employed for the study described below on the influence of the electric potential of the housing on the electric field distortion (see section 3.1).

For the following investigations, the dimensions for the FAC_{flex} simulation model were selected based on the results of the simulations described above. Geometry was optimized so that field lines intersect ideal lines on the beam axis (see section 4.2). The selection is presented in table 1. To evaluate the impact of engineering tolerances on the uncertainty of the correction factor k_d, minor systematic variations were made to the components of the FAC_{flex} ranging from micrometer to millimeter. The collecting electrode was displaced along the beam axis (longitudinal shift) and up and down in the direction perpendicular to the beam axis (vertical shift). The high-voltage electrode, the ground electrode (which includes both the collecting and guard electrode), and the guard rings were also shifted vertically. Furthermore, the aperture underwent vertical shifts and adjustments from side to side (transversal shift).

2.2. FEM simulations of the electric field

The study employed 3D FEM simulations using COMSOL Multiphysics 6.1.0.252 and the Electrostatics Interface to compute the electric field. After the CAD models of the FACs were imported, the electric potentials were assigned to the individual components. The housing, guard, and collecting electrode were set to ground potential, and the high-voltage electrode to V_{HV}. The electric potential applied to the guard rings between the electrodes was adjusted to create a progressively decreasing electric potential from the high-voltage electrode to the ground electrode. Part of the study involved varying the applied housing potential to assess the impact of the housing potential on electric field distortion. The electric potentials evaluated besides ground potential were $V_{HV}/2$ and V_{HV}.

After determining the electric field distribution, the electric field lines in the midplane cross-section perpendicular to the electrodes were computed. The two electric field lines that define the collecting volume were calculated, with the starting point being the center of the air gap on both sides of the collecting electrode. The electric field distortion was then quantitatively evaluated by calculating the correction factor k_d from the electric field lines.

The correction factor for the electric field distortion k_d can be derived from the ratio of a collection volume defined by hypothetical, perfectly straight field lines (V_{ideal}) and the collecting volume spanned by the actual electric field lines V_{eff},

$$k_d = \frac{V_{ideal}}{V_{eff}}. \tag{1}$$

In the validation approach with the PK100 described by Gschweng and Pojtinger [13], the volume ratio was calculated as the ratio of the ideal collecting length l_{ideal} and the effective collecting length l_{eff}. For this, equation (1) can be simplified

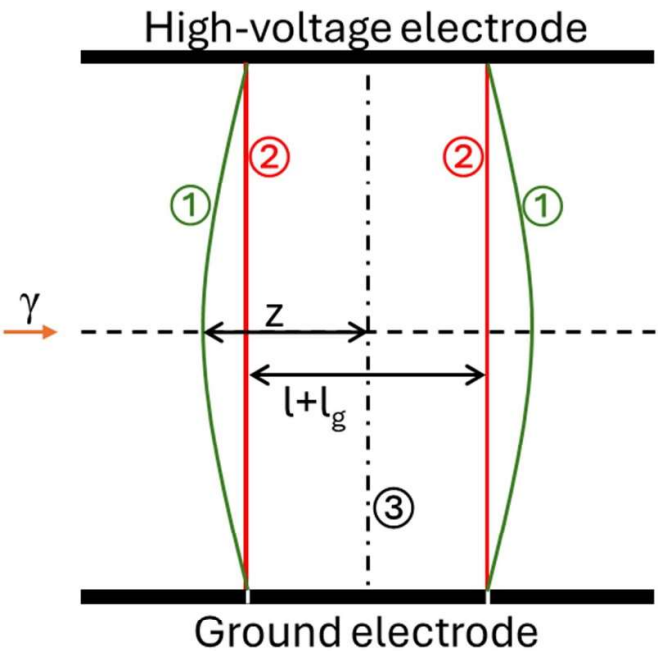

Figure 2. Sketch of the collecting volume defining field lines of a free-air ionization chamber. ① distorted electric field lines, ② ideal electric field lines, ③ middle of the collecting electrode. z and $l + l_g$ are used to calculate k_d according to equation (2).

for the symmetrical FAC_{flex} to:

$$k_d = \frac{l_{ideal}}{l_{eff}} = \frac{l + l_g}{2 * z}, \tag{2}$$

where l is the collecting electrode length, l_g is the length of the air gap between the collecting electrode and the guard electrode and z is the distance from the intersection of the electric field line with the beam axis and the middle of the collecting electrode (see figure 2).

3. Results

3.1. Influence of the housing potential on the electric field

The influence of the electric potential of the housing on the electric field distortion was investigated, with a series of 3D FEM simulations using the FAC_{flex} model. The electric housing potential varied between grounded, half the high-voltage potential ($V_{HV}/2$), and equal to the high-voltage potential (V_{HV}). The derived correction factors for electric field distortion k_d were 0.9993 for the grounded housing, 0.9985 for the housing at $V_{HV}/2$, and 0.9977 for the housing at V_{HV}.

3.2. Dependence between FAC geometry and electric field distortion

The dependence between FAC geometry and electric field distortion was analyzed by varying the geometry of the FAC_{flex}. The aim was to identify geometric parameters that could alter the electric field distribution within the FAC so that k_d is unity. Appendix figure A1 shows one of the two electric field lines

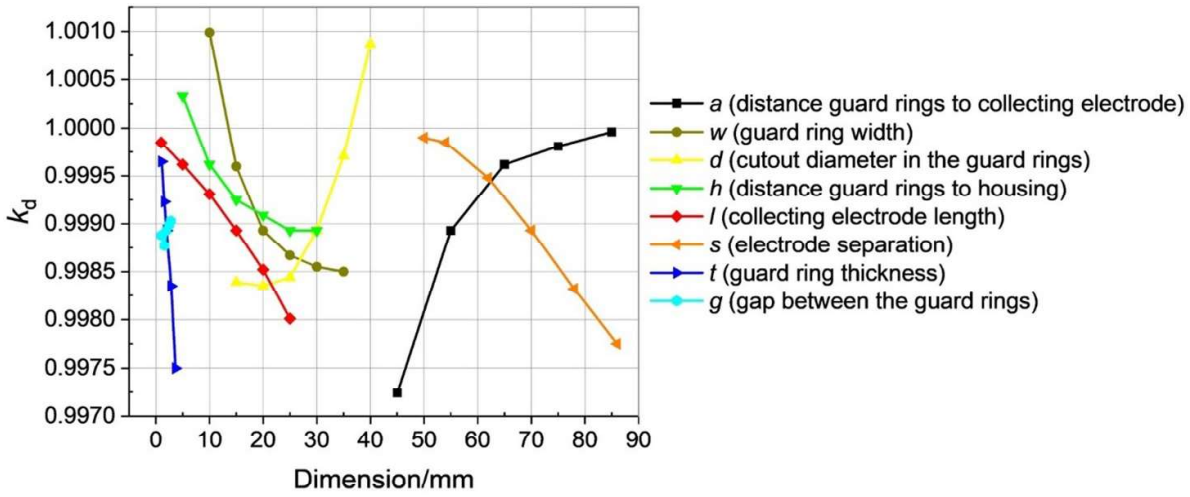

Figure 3. Dependence between the correction factors for electric field distortion k_d and the geometric parameters of the FAC_{flex}. For the definition of the geometric parameters see figure 1 and table 1.

defining the collecting volume for each geometric parameter and all variations made to its dimension. Given the symmetry of the FAC_{flex}, the other electric field lines of interest are mirrored. k_d was calculated for each electric field line using equation (2). The dependencies between k_d and the geometric parameters are illustrated in figure 3.

Varying the guard ring gap g from 1 to 2.8 mm had negligible impact on field lines (see appendix figure A1(a)). The maximum difference in k_d due to variation in g was less than 0.03%.

Varying the distance between the middle of the collecting volume and the inner edge of the guard rings a, showed that the electric field lines (see appendix figures A1(e)) were straighter for a larger a. Consequently, the value of k_d approached 1. The variation of the collecting electrode length l, the electrode separation s, and the guard ring thickness t showed straighter electric field lines (see appendix figure A1(f)–(h)) for smaller dimensions, leading to an approach of k_d towards 1.

The variation of the cutout diameter in the guard rings d, the guard ring width w, and the distance from the housing to the guard rings h (see appendix figures A1(b)–(d)) did not consistently result in a value of k_d approaching 1. For $d = 36$ mm, k_d was approximately 1. An increasing d resulted in a k_d greater than 1 and a decreasing d in a k_d smaller than 1. The dependence of k_d on the guard ring width w and the distance from the housing to the guard rings h was found to be reversed. For $w = 14$ mm and $h = 7$ mm, k_d was approximately 1. A decrease in w and h resulted in a k_d greater than 1, whereas an increase in w and h led to a k_d lower than 1.

3.3. Impact of engineering tolerances on the uncertainty

Based on the selected dimension derived from 3.2 as described in 4.2, the effect of engineering tolerances on the uncertainty of k_d was investigated. For this, the components of the electric field defining system of the FAC_{flex} were shifted in their positions by micrometers to millimeters. The corresponding electric field lines can be found in the appendix in figure A2. The correction factors for electric field distortion $k_{d,shifted}$ were calculated for the FAC geometries with displaced components and compared to the value of $k_{d,0}$ of the mechanically accurate FAC_{flex}. In figure 4, the relative deviations of $k_{d,shifted}$ from $k_{d,0}$ are plotted against the geometric shift of the respective component.

The vertical shift of the collecting electrode showed the steepest slope in the linear fit. 0.2 mm vertical shifting of the collecting electrode was a 1.4% relative deviation in the value of k_d. The smallest relative deviations were observed for the vertical and transversal displacement of the aperture, and the longitudinal displacement of the collecting electrode. The relative deviations were found to be less than 0.02% for a 1 mm geometric shift.

4. Discussion

4.1. Influence of the housing potential on the electric field

Varying the electric potential of the housing of the FAC_{flex} from grounded to $V_{HV}/2$ resulted in a difference of 0.08% in the correction for electric field distortion in the 3D simulation. With grounded housing, the correction of electric field distortion was smaller than that of the simulations with applied housing potential. In contrast, previous studies by Takata [7], Groetz *et al* [11], and Mohammadi *et al* [12] suggested that the electric field distortion is reduced when the housing is set to $V_{HV}/2$.

Takata [7] did not specify whether their simulations were conducted in 3D or 2D. However, their description of the FAC geometry suggests that they computed the FEM in 2D. We therefore recreated our FEM simulation series employing a 2D model. The 2D model corresponded to the cross-sectional geometry of the 3D model. When simulating in 2D instead of 3D, the value of k_d for a FAC with housing at $V_{HV}/2$ was 0.9999. This corresponds to a 0.80% reduction in electric field distortion when compared to a 2D FAC with grounded housing. However, we observed a discrepancy of up to 0.87%

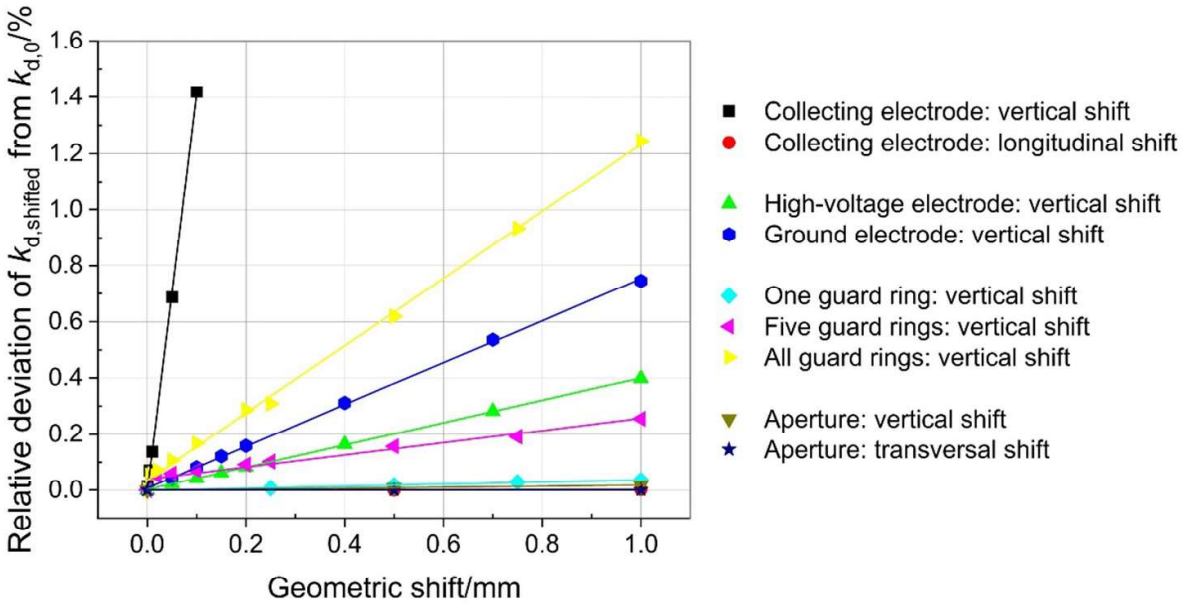

Figure 4. Deviations of k_d when shifting the components of the electric field defining system of the FAC_{flex}.

between the 2D and 3D simulations. A 2D cross-section of the FAC mid-plane does not fully capture the internal geometry. In particular, the cutouts in the guard rings appear in 2D as if the entire rings in the mid-plane were absent, whereas in the actual 3D geometry the applied potential on these rings still contributes to maintaining field uniformity. Consequently, 2D FEM simulations cannot accurately reproduce the electric field distribution in the FAC. These observations align with the findings of Miller and Kennedy [4], who reported that 2D approaches tend to overestimate electric field distortions. Based on this, a 3D FEM approach is required to realistically assess electric field distortions in the FAC.

Groetz *et al* [11] utilized 3D FEM to analyze electric field distortions. However, their study focused on a miniature FAC with considerably different geometry. As demonstrated in section 3.2, the electric field of a FAC is strongly dependent on its geometry. Consequently, comparing the electric field distortion from a miniature FAC to that of a larger FAC is challenging. Any statement regarding the advantages of applying $V_{HV}/2$ to the housing must consider the geometry involved.

Mohammadi *et al* [12] also used 3D FEM to assess the electric field distortion. The FAC under consideration was designed for medium x-ray energies and was larger than the FAC_{flex} that was utilized in the present study. For this larger FAC, we do not anticipate that the housing potential will affect the electric field distribution, as the cutout in the guard rings is small and the distance between the collection volume and the housing is large, as discussed in section 4.2. Consequently, k_d should remain constant when the applied housing potential changes. To verify this, we re-modeled the FAC of Mohammadi *et al* [12] and performed 3D FEM simulations with the housing grounded and at $V_{HV}/2$. For both scenarios, the resulting k_d was 0.9995, thereby confirming our hypothesis.

4.2. Dependence between FAC geometry and electric field distortion

The study demonstrated that modifying the geometric parameters of the symmetrical FAC_{flex} results in three distinct outcomes. These outcomes offer opportunities to modify the electric field by adjusting the geometry of a FAC, thereby reducing electric field distortions.

Firstly, it was observed that varying the gap between the guard rings g between 1 and 2.8 mm did not significantly influence the electric field. Uotila [6] concluded that minimizing the gap between the guard rings enhances the uniformity of the electric field. However, the current study differs from the work of Uotila, which considered the effect of the gap width depending on the thickness of the guard rings. The influence of the thickness of the guard rings on the electric field distortion with constant g is discussed below.

Secondly, variations in the dimensions of certain geometric parameters straightened the electric field lines, resulting in a value of k_d approaching 1. One of these geometric parameters was the distance between the middle of the collecting electrode and the inner edge of the guard rings a. A larger a means a wider guard electrode. As shown by Miller and Kennedy [4] using a 2D analog of a FAC for measuring electric field distortions, a wider guard electrode reduces the electric field distortion. However, this also increases the air path length of the FAC. This is undesirable for FACs employed in low-energy x-ray ranges, where minimizing the air path length is required to reduce air attenuation [14]. A similar discrepancy has been observed in relation to the electrode separation. The smaller the electrode separation, the straighter the electric field lines. Too small an electrode gap may allow secondary electrons to reach the electrode prematurely.

Another geometric parameter that caused k_d to approach 1, was the collecting electrode length l. Miller and Kennedy

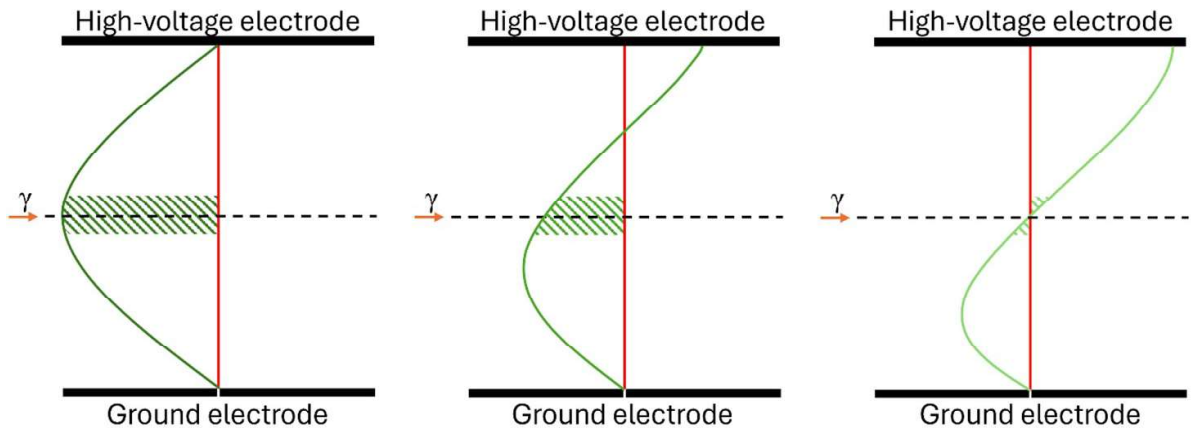

Figure 5. Sketch of one of the collecting volume defining field lines. The dashed area marks the difference between the effective collecting volume (defined by the distorted electric field line and the beam diameter) and the ideal collecting volume. From left to right: The curvature of the distorted field line changes so that its intersection with the ideal field line moves from the high-voltage electrode toward the ground electrode. When the intersection of the distorted field line and the ideal field line is exactly on the beam axis (sketch on the right), the additional and missing volume are the same size. As a result, the effective collecting volume is equal to the ideal collecting volume.

[4] previously noted that a greater collecting electrode length would result in less electric field distortion. Takata [7] found the opposite. This study found that reducing l resulted in the straightening of the electric field lines. This is due to the fact that, in a symmetrical FAC, the central field line is perfectly straight. As the collecting electrode shortens, the collecting volume defining electric field lines shift closer to the center of the FAC. Nevertheless, as a shorter collecting electrode length results in a smaller collecting volume, it cannot be reduced indefinitely as this would result in a too small measurement signal.

Varying the thickness of the guard rings also resulted in k_d approaching 1. Thinner guard rings increase the number of guard rings between the electrodes and, therefore, the regions defining the electric potential within the FAC, leading to a more uniform electric field. However, the thickness of the guard rings is constrained by construction feasibility.

Thirdly, by varying certain geometric parameters, the curvature of the electric field line changed, causing its intersection with the ideal field line to shift from the high-voltage electrode side toward the ground electrode side (shown in figure 5). These were the distance from the housing to the guard rings h, the cutout diameter in the guard rings d, and the guard ring width w. Compared to the above-mentioned geometric parameters, the value of k_d did not approach 1 through systematic scaling of h, d, and w. Instead, k_d was 1 at a specific value for each geometric parameter. At these values, the intersection of the simulated electric field line with the ideal electric field line was located on the beam axis. This resulted in the effective collecting electrode length being equivalent to the ideal collecting electrode length. These outcomes refine the findings from those of Takata [7], who reported that a reduction in the size of cutout in the guard rings leads to less distortion in the collecting volume, and those of Miller and Kennedy [4], as they concluded that the electric field distortion is larger when the housing is closer. It is important to note that bending the electric field lines as described above is only effective when the housing is grounded. Conversely, if the housing potential is set to $V_\mathrm{HV}/2$, variations in the mentioned parameters will not change the electric field.

The findings presented herein are confined to a symmetrical FAC. Moreover, any impact of a geometric parameter on the electric field distortion depends on the other geometric parameters. Consequently, the approach outlined to alter the electric field lines by adjusting the geometric parameters of the FAC to achieve $k_\mathrm{d} = 1$ may not be universally applicable to all FAC designs.

4.3. *Impact of engineering tolerances on the uncertainty*

The present study examined the impact of the engineering tolerances of FAC components on the uncertainty associated with the simulated value of the correction factor for electric field distortion k_d. The results show that the non-planarity between the collecting and the guard electrode has the most substantial influence on k_d. Boag [5] noted the importance of precise alignment between the collecting and the guard electrode. The results of this study enable quantification of this requirement, showing that to maintain relative deviations in k_d smaller than 0.1%, the collecting electrode and the guard electrode must be aligned planar to each other within 0.008 mm. The second largest influence on k_d was observed when shifting all guard rings. To limit the relative deviation in k_d to less than 0.1%, a mechanical positioning precision of at least 0.05 mm is required. While the non-planarity between the collecting and guard electrode has a greater influence on k_d, the precise positioning of the guard rings during the construction of a real FAC contributes more to the uncertainty of k_d. Aligning two surfaces with a precision of 0.001 mm is feasible, but achieving a positioning precision of 0.015 mm for all the guard rings presents a challenge.

As reported by Burns and Büermann [1], k_d is commonly assumed to be unity with an uncertainty of less than 0.1% for numerous FACs. However, the authors did not specify the origin of the uncertainty value. Using the data from the present study allows the derivation for the uncertainty of k_d caused

Table 2. Uncertainty assessment for the correction factor for diaphragm effects k_d for the new PTB primary standard.

	Tolerance	Relative deviation from $k_{d,0}$	Standard uncertainty
Distance guard rings to collecting electrode *a*	±0.1 mm	0.004%	0.002%
Collecting electrode: vertical shift	±0.001 mm	0.015%	0.009%
High-voltage electrode: vertical shift	±0.015 mm	0.009%	0.005%
Ground electrode: vertical shift	±0.015 mm	0.018%	0.010%
All guard rings: vertical shift	±0.015 mm	0.065%	0.038%
Midplane simplification ➔Aperture: transversal shift	±5 mm	0.015%	0.009%
Resistors	±0.01%	0.011%	0.006%
Total k_d uncertainty			0.042%

by engineering tolerances. This, in turn, offers opportunities to specify the engineering tolerances to minimize the uncertainty of k_d.

In the following, the example of the new PTB primary standard will be used to demonstrate the calculation of an uncertainty budget for k_d from the results of this study. After determining the FAC geometry and the engineering tolerances, the relative deviations of k_d for the limit values of the engineering tolerances were read from figures 3 and 4. We assumed that k_d is uniformly distributed within the intervals resulting from the FEM simulations and calculated the standard uncertainty for k_d according to the Guide to the expression of Uncertainty in Measurement [15]. Table 2 shows the engineering tolerances selected for the new PTB primary standard, the relative deviations from $k_{d,0}$ resulted from the engineering tolerances, and the calculated standard uncertainties. Only contributions to the uncertainty of k_d greater than 0.001% were considered. In addition to the uncertainty contributions from engineering tolerances, two further contributions to the uncertainty of k_d are listed. As outlined in section 2.2, the FEM simulations were conducted utilizing a 3D model, yet the electric field lines were calculated exclusively for the midplane of the geometry. Consequently, the transverse width of the collecting volume was disregarded. To account for this simplification in the uncertainty budget, a transverse shift of the aperture is considered with a tolerance equal to the aperture diameter. The uncertainty contribution from the tolerance of the resistors of the voltage divider was also determined using FEM simulations.

5. Conclusion

This study systematically investigated the electric field within a FAC using FEM simulations. The aim was to optimize the FAC geometry of the new PTB primary standard to minimize electric field distortion and to evaluate the contribution of engineering tolerances to the uncertainty of the correction factor for electric field distortion k_d. It is important to note that the FAC_{flex} chamber presented in this work is a design proposal and is not physically realized at the time of the study. The results presented are based on simulations, and experimental verification is essential and will be carried out in subsequent studies.

The results of this study proved that the previous assumption that applying half the high-voltage potential to the housing reduces electric field distortions is not fundamentally applicable. Instead, there are two approaches to adjust the geometry of the FAC such that k_d is about 1. The straightforward method utilizes geometric parameters that straighten the electric field lines, leading to an approximation of k_d to 1 when these parameters are increased or decreased. However, this can result in significant trade-offs with other aspects. For instance, reducing the electrode separation to minimize electric field distortion conflicts with the correction factor for electron loss. The alternative method takes advantage of the ability to shape the electric field lines when the housing is grounded. Specific geometric parameters, such as the cutout diameter in the guard rings, can be adjusted to ensure the electric field lines align with the ideal electric field lines on the beam axis. Thus, the effective length of the collecting electrode is equal to its ideal length and k_d is 1.

Even minor geometric deviations can significantly affect the electric field. A systematic analysis of these influences enabled the identification of components that are highly sensitive to engineering tolerances. The data provided in this study allows the quantification of the uncertainty of k_d based on the engineering tolerances of the FAC. Without this study, only a rough estimate of at least 0.1% would have been assumed for the uncertainty of k_d for PTB's new primary standard. The present results, however, allowed us to define the engineering tolerances such that the resulting uncertainty will be reduced to about 0.04%, more than halving the initial estimate.

Appendix

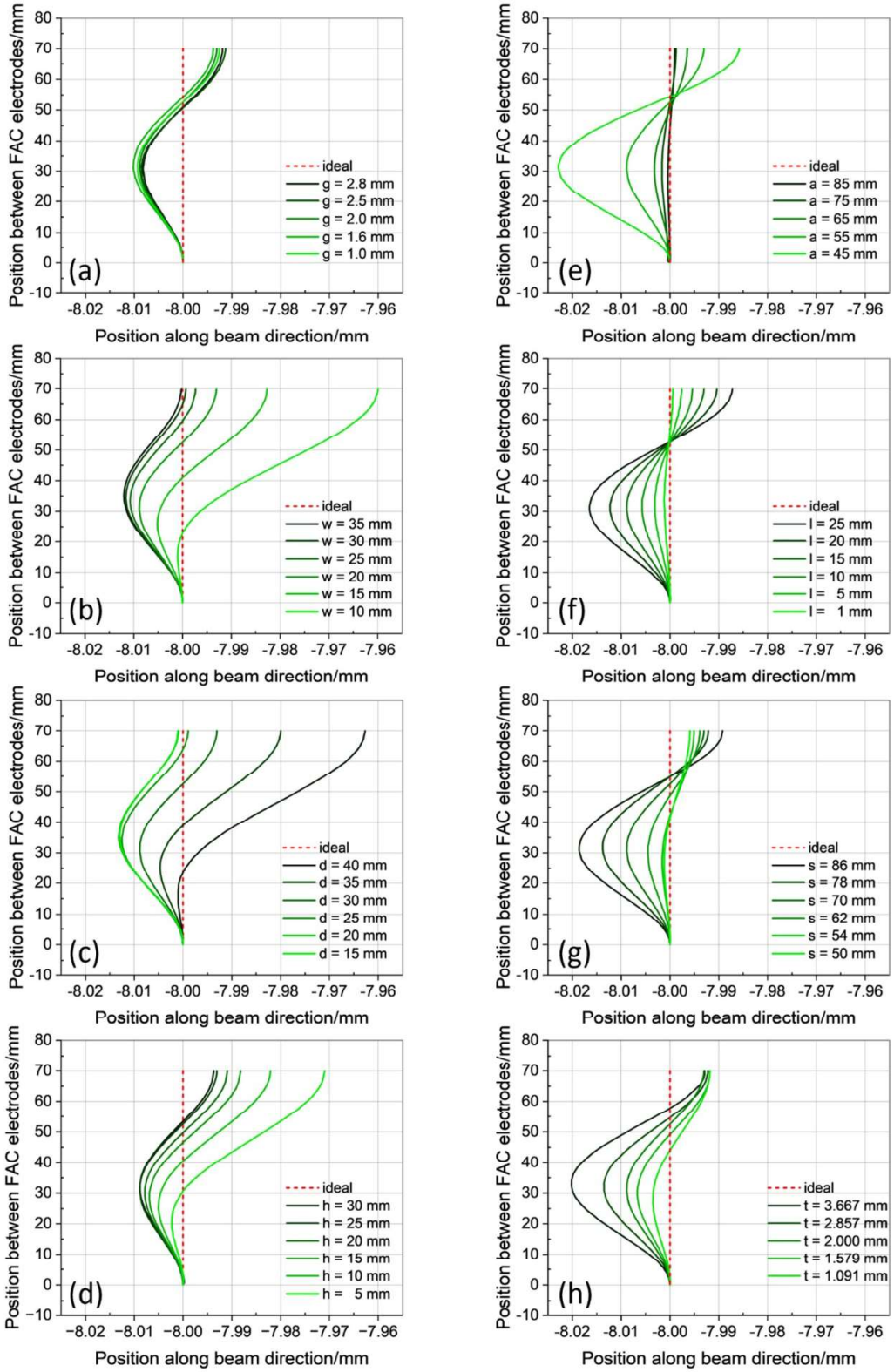

Figure A1. Electric field lines of a free-air ionization chamber with variable geometry. Each subpanel shows the influence of one geometric parameter: (a)—gap between the guard rings g, (b)—guard ring width w, (c)—cutout diameter in the guard rings d, (d)—distance guard rings to housing h, (e)—distance guard rings to collecting electrode a, (f)—collecting electrode length l, (g)—electrode separation s, (h)—guard ring thickness t. The field lines in graph (f) have been shifted towards the same x-axis value for better comparability. The field lines in graph (g) have been scaled to the same y-axis for better comparability.

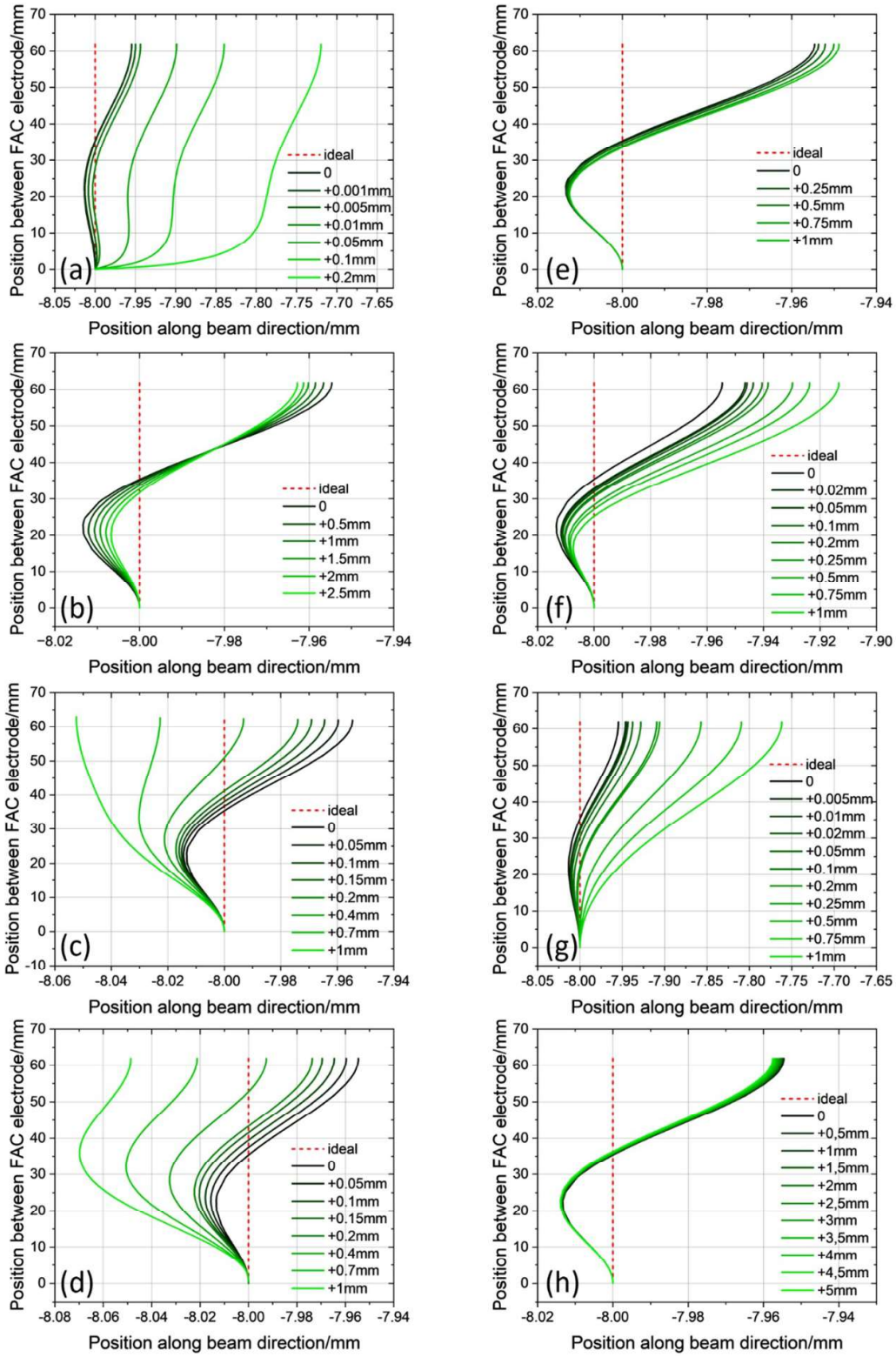

Figure A2. Electric field lines of a free-air ionization chamber with individually shifted geometric components. Vertical (a) and longitudinal (b) shift of the collecting electrode; vertical shift of the high-voltage (c) and the ground (d) electrode; vertical shift of one (e), five (f) and all (g) guard rings; transversal shift of the aperture (h). The field lines in graph (b) have been shifted towards the same x-axis value for better comparability.

ORCID iDs

J Gschweng 0009-0001-0834-6626
S Pojtinger 0000-0001-6397-4572

References

[1] Burns D T and Büermann L 2009 Free-air ionization chambers *Metrologia* **46** S9
[2] Büermann L 2021 *The PTB free-air ionization chambers* Physikalisch-Technische Bundesanstalt (https://doi.org/10.7795/120.20220324)
[3] Kemp L A W, Read L R and Woodall J E 1968 Field distortion in a parallel-plate free-air chamber: a compensatory effect *Phys. Med. Biol.* **13** 91—-95
[4] Miller W and Kennedy R J 1955 Measurement of field distortion in free-air ionization chambers by analog method *J. Res. Natl Bur. Stand.* **55** 291–7
[5] Boag J W 1964 Distortion of the electric field in an ionization chamber due to a difference in potential between guard ring and collector *Phys. Med. Biol.* **9** 25
[6] Uotila I K 1980 Field distortion in guarded-wall free-air ionization chambers *Metrologia* **16** 15
[7] Takata N 2010 A free-air ionization chamber with a large aperture diaphragm *Nucl. Instrum. Methods Phys. Res. A* **619** 216–20
[8] Rogers D W O, Kawrakow I, Klassen N V, McCaffrey J P and Ross C K 2001 NRC activities and publications, 1999–2001 Report to CCRI(I) Meeting, BIPM (available at: www.irs.inms.nrc.ca/inms/irs/papers/CCRI01/01ccri.html)
[9] Yi C-Y, Kim Y H and Jeong D Y 2022 Effective volume of the Korea research institute of standards and science free air chamber L1 for low-energy x-ray measurement *Prog. Med. Phys.* **33** 1–9
[10] Kessler C 2013 Développement et mise en place au BIPM d'un systéme international de comparaison et d'étalonnage pour la dosimétrie en mammographie
[11] Groetz J-E, Ounoughi N, Mavon C, Belafrites A and Fromm M 2014 Conception and realization of a parallel-plate free-air ionization chamber for the absolute dosimetry of an ultrasoft x-ray beam *Rev. Sci. Instrum.* **85** 083304
[12] Mohammadi S M, Tavakoli-Anbaran H and Zeinali H Z 2016 Investigation of electric field distribution on FAC-IR-300 ionization chamber *J. Instrum.* **11** P07017
[13] Gschweng J and Pojtinger S 2024 PP10.04 validation of the finite element method to determine the sensitive volume of free-air ionization chamber standards *Phys. Med.* **125** 103811
[14] Gschweng J and Pojtinger S 2025 Free-air ionization chambers for the measurement of air kerma in low-energy x-rays—optimum air path length and the limitations of averaging monoenergetic correction factors *Metrologia* **62** 025013
[15] Joint Committee for Guides in Metrology 2008 Evaluation of measurement data—Guide to the expression of uncertainty in measurement (JCGM)

RAP CONFERENCE PROCEEDINGS, VOL. 10, PP. 16–20, 2025
ISSN 2737-9973 (ONLINE) | DOI: 10.37392/RAPPROC.2025.04
RAP-PROCEEDINGS.ORG

OPTIMAL GEOMETRIC DESIGN OF THE DIAPHRAGM OF A FREE-AIR IONIZATION CHAMBER FOR LOW-ENERGY X-RAYS

Jessica Gschweng[1,2*], Stefan Pojtinger[1]

[1]Physikalisch-Technische Bundesanstalt (PTB), Braunschweig, Germany
[2]Technische Hochschule Mittelhessen, Gießen, Germany

Abstract. *For reliable and comparable measurements of the dose quantity air kerma, dosimeter measurements must be traceable to a primary standard. Primary standard laboratories use free-air ionization chambers (FACs) for the primary realization of the unit of the air kerma free-in-air. Correction factors must be applied to convert measured charge to air kerma. One such correction factor is the correction factor for diaphragm effects (k_{dia}). This study investigated the impact of the geometry of the diaphragm on k_{dia}, as established FACs from different metrology institutes use different diaphragm geometries. The aim was to find the optimal diaphragm thickness and aperture shape to minimize the required diaphragm correction for the new PTB primary standard. Monte Carlo simulations were performed to determine k_{dia} for various diaphragm geometries of a low-energy x-ray FAC. The influence of the diaphragm thickness and the aperture shape were investigated. The results showed that the diaphragm needs to be sufficiently thick to prevent transmission yet as thin as possible to reduce scattering at the inner surface of the aperture. The optimal diaphragm thickness, which depends on the air path length of the FAC, ranges from 0.8 mm to 1 mm. Using a diaphragm geometry with a more complex geometry than a simple 1 mm thick diaphragm with a cylindrical aperture is not advantageous.*

Keywords: *free-air ionization chamber, primary standard, air kerma, diaphragm correction factor, Monte Carlo simulation*

1. INTRODUCTION

Diagnostic dosimeters are specialized instruments that measure the energy deposited by ionizing radiation in a material. These devices are used in acceptance and constancy testing to measure air kerma in diagnostic applications and thereby ensure compliance with regulatory safety standards. Regular calibration of diagnostic dosimeters is essential to maintain measurement accuracy, reliability, and comparability. National metrology institutes use free-air ionization chambers (FACs) as primary standards to realize the unit of the air kerma free-in-air. With the increasing demand for low-energy x-ray calibrations, particularly in the energy range of mammography, the Physikalisch-Technische Bundesanstalt (PTB) is currently developing a new primary standard for x-ray energies up to 50 keV.

The principle of a FAC is based on an x-ray beam entering the chamber through the entrance diaphragm and interacting with the air inside the FAC, thereby producing secondary electrons. The secondary electrons create ion pairs, which are subsequently measured as charge by an applied electric field. The measured charge can be converted into the air kerma using several correction factors that compensate for non-idealities in the geometry and operation of the FAC. The correction factors should always be as small as possible to minimize potential sources of errors or large uncertainties. Most correction factors depend on the geometry of the FAC and should be considered when designing a new primary standard.

According to ICRU Report 85 [1], kerma K is defined as the mean sum of the initial kinetic energies $\mathrm{d}E_{\mathrm{tr}}$ of all charged particles liberated in a mass $\mathrm{d}m$ of a material by uncharged particles, thus

$$K = \frac{\mathrm{d}E_{\mathrm{tr}}}{\mathrm{d}m}. \qquad (1)$$

The unit of kerma is gray.

Consequently, air kerma only reflects dose contributions from secondary electrons generated by the interaction of the primary photon beam with the air inside the FAC. Dose contributions from particles that have interacted with the diaphragm – transmitted, scattered and fluorescence photons or electrons produced in the diaphragm by the incident photons – are excluded from the definition of air kerma. The diaphragm correction factor, denoted as k_{dia}, corrects for dose contributions from these secondary particles. Like several other correction factors, k_{dia} depends on the geometry of the FAC. In particular, k_{dia} is influenced by the geometry of the diaphragm itself [2–7]. In addition, the distance between the diaphragm and the collection volume is critical because it determines whether particles created by interactions with the diaphragm reach the collection volume and can contribute to the measured charge. To minimize photon attenuation in air this distance should be as small as possible for a low-

* jessica.gschweng@ptb.de

energy x-ray primary standard [8]. This increases the correction for diaphragm effects. Therefore, it is important to reduce k_{dia} with an optimized diaphragm geometry.

This study systematically investigates the optimal diaphragm geometry to minimize the diaphragm correction factor for a low-energy x-ray FAC, with the aim of finding the best solution for the new PTB primary standard.

2. Materials and Methods

To investigate the optimal geometric design of the diaphragm of a low-energy x-ray FAC, a simplified FAC was modeled in the Monte Carlo simulation environment EGSnrc [9]. The FAC model consisted of a housing, two plane-parallel electrodes, and a tungsten diaphragm with 10 mm aperture diameter. A sketch of the FAC model is shown in Figure 1.

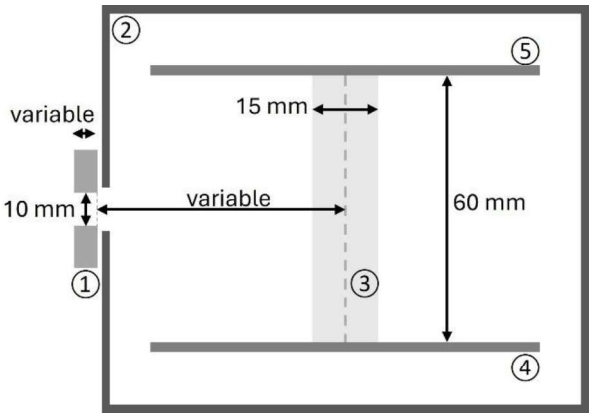

Figure 1. Cross-sectional sketch of the Monte Carlo simulation model of the free-air ionization chamber with variable entrance diaphragm ① geometry. The air path length (the distance between the reference plane of the FAC, defined by the diaphragm, and the middle of the collecting volume ③) is variable. The housing ② contains the ground ④ and the high-voltage electrode ⑤.

In the Monte Carlo simulations, the diaphragm thickness and the aperture shape of the diaphragm were varied. The diaphragm thickness was varied between 0.4 mm and 10 mm for a FAC model with variable air path length. The air path length is defined as the distance between the reference plane of the FAC, which is located at the downstream end of the diaphragm, and the middle of the collecting volume. Air path lengths between 40 mm and 100 mm were chosen based on common dimensions of established low-energy x-ray FACs from various metrology institutes [8]. For this part of the study, the aperture of the diaphragm was cylindrical.

To further evaluate the optimal design for the aperture of the diaphragm, three different aperture shapes (see Figure 2) were compared: cylindrical, conical, and hybrid. For the hybrid shape, the upstream half of the diaphragm was cylindrical, and the downstream half was conical. The opening angles for conical and hybrid apertures ranged from 0.15° to 45°. For this part of the study, the air path length of the FAC model was 60 mm, and the diaphragm thickness was between 1 mm and 10 mm.

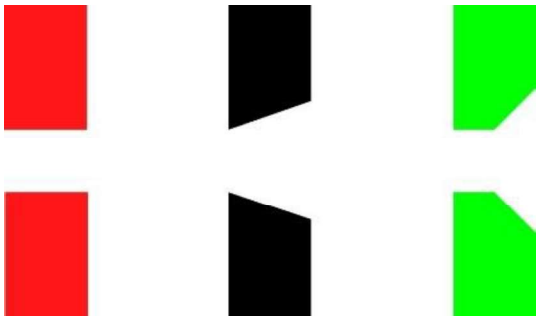

Figure 2. Different aperture shapes of the diaphragm of a free-air ionization chamber: cylindrical (left), conical (middle), hybrid (right).

Monte Carlo simulations were carried out with the EGSnrc user code egs_fac [10] to calculate the correction factor for diaphragm effects k_{dia}. k_{dia} was calculated as follows:

$$k_{\mathrm{dia}} = \frac{E1}{Eg}, \qquad (2)$$

where Eg is the total energy deposited in the collecting volume and $E1$ is the energy deposited in the collecting volume without the contribution of the particles that have interacted with the diaphragm or been generated by such interactions. Accordingly, $E1$ excludes energy contributions caused by transmission through the diaphragm, as well as by both scattering at the diaphragm and fluorescence.

A monoenergetic x-ray beam with an energy of 50 keV was simulated to analyze the influence of the diaphragm geometry. A point source was defined at a distance of one meter from the reference plane of the FAC. The beam diameter at the reference plane was 12 mm. The applied Monte Carlo simulation parameters are listed in Table 1.

Table 1. Parameters applied for the Monte Carlo simulations according to [11].

Parameter	Description	Ref.
Code	EGSnrc release version 2021	[9]
Timing	PTB computing cluster (CPU), approx. 10^7-10^8 histories per hour	
Cross-sections	mcdf-xcom	
Transport parameters	Electron cutoff 0.512 MeV, photon cutoff 0.001 MeV	
Variance reduction	Photon splitting, Russian Roulette	[12]
Histories	10^9-10^{11} histories per simulation	
Statistical uncertainty	≤ 0.01 % for k_{dia}	
Postprocessing	OriginPro 2023b	

3. Results

The aim of this study was to determine the optimal diaphragm geometry, in terms of diaphragm thickness

and aperture shape, using Monte Carlo simulations. The influence of the geometric design on the diaphragm correction factor k_{dia} was evaluated by systematically varying these parameters. The results of the Monte Carlo simulation study are presented in the following sections.

3.1. Diaphragm thickness

The diaphragm thickness for FAC models with air path lengths ranging from 40 mm to 100 mm was varied between 0.4 mm and 10 mm. For each air path length of the FAC, an optimal diaphragm thickness was determined at which the value of k_{dia} is closest to 1 (see Figure 3). As the air path length of the FAC model increased, the optimal diaphragm thickness also increased slightly. For instance, an optimal thickness of 0.8 mm was found for an air path length of 40 mm, while it was 1 mm at 100 mm air path length. For diaphragm thicknesses below these optimal values, a steep drop in k_{dia} was observed, indicating that more correction of diaphragm effects is required. Conversely, for diaphragm thicknesses exceeding the optimal value, a continuous moderate decrease in the value of k_{dia} was observed. However, this decrease was steeper for an air path length of 40 mm.

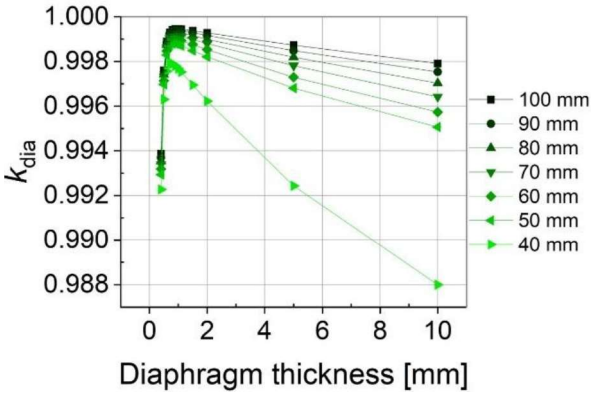

Figure 3. Diaphragm correction factor k_{dia} as a function of the diaphragm thickness, plotted for several air path lengths of the free-air ionization chamber model.

3.2. Aperture shape

The impact of three different aperture shapes (cylindrical, conical and hybrid) on the diaphragm correction factor k_{dia} was analyzed. Figure 4 shows the values of k_{dia} in dependence on the aperture shape and the diaphragm thickness for a FAC model with an air path length of 60 mm. For a 1 mm thick diaphragm with a cylindrical aperture, k_{dia} was 0.9990. For conical and hybrid apertures with opening angles of 0.3°, k_{dia} approached 1. The thicker the diaphragm, the greater the observed difference between 0° and 0.3°. The best value for k_{dia} (0.9997) was observed for a 10 mm thick diaphragm with conical aperture and an opening angle of 0.3°. This indicates a 0.4% reduction in diaphragm correction when compared with a 10 mm diaphragm with cylindrical aperture. Compared to a 1 mm diaphragm with cylindrical aperture, this is a 0.07% reduction in diaphragm correction.

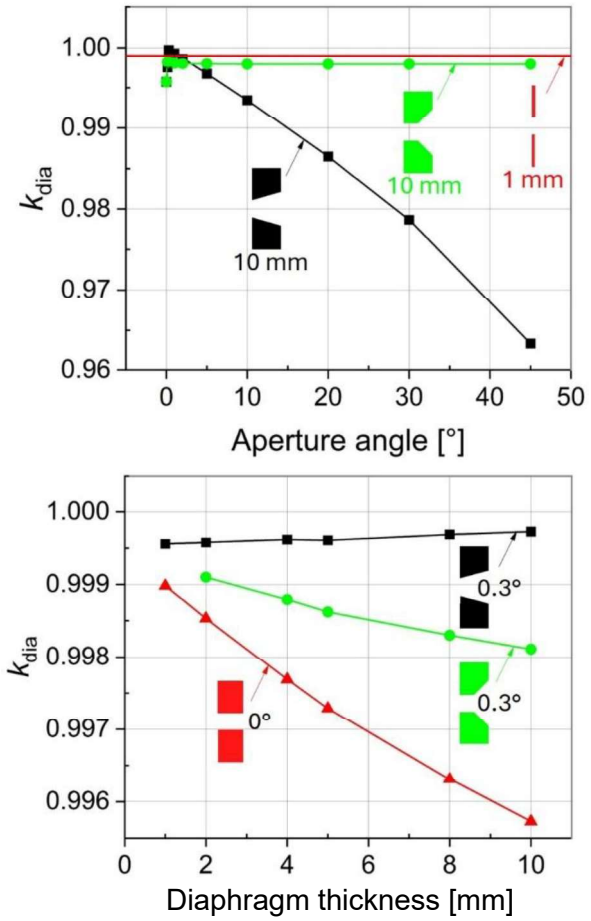

Figure 4. Top: k_{dia} as a function of the aperture opening angle for a 10 mm thick diaphragm with conical or hybrid aperture. For comparison, the k_{dia} value for a 1 mm thick diaphragm with cylindrical aperture is given as a constant. Bottom: k_{dia} as a function of the diaphragm thickness for diaphragms with cylindrical or conical and hybrid apertures with opening angles of 0.3°.

4. Discussion

The diaphragms in established FACs of different metrology institutes have different geometric designs regarding diaphragm thickness and aperture shape. Figure 5 shows the technical drawings of the diaphragms of three different FACs – two from PTB and one from the Bureau International des Poids et Mesures (BIPM). Furthermore, the literature is inconsistent regarding the dependence between the diaphragm correction factor and the diaphragm thickness or the aperture shape. These inconsistencies will be addressed in the following sections.

4.1. Diaphragm thickness

The results of the Monte Carlo simulations with the FAC with cylindrical diaphragm and varying diaphragm thickness, see Figure 3, show that the diaphragm must be thick enough to prevent transmission through the diaphragm body. At the same time, it must be as thin as possible to reduce the inner surface of the aperture

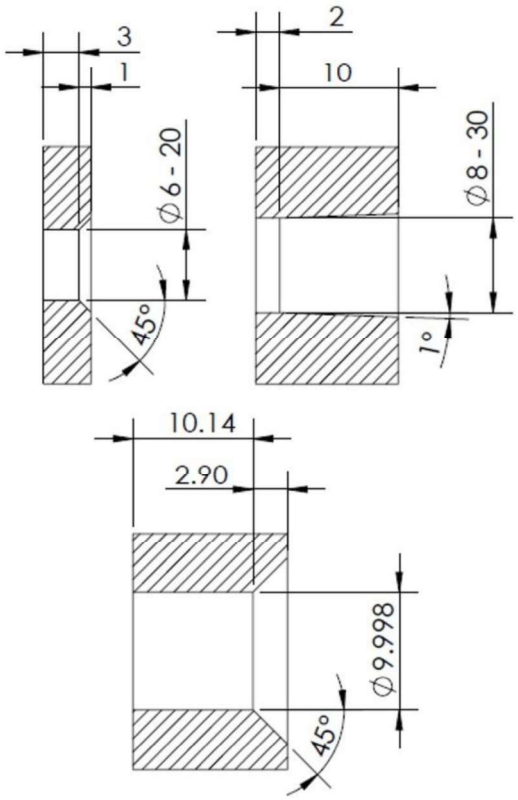

Figure 5. Technical drawings of the diaphragms of PTB's PK100 (top left) and FK (top right) [13], and of BIPM's FAC-L-02 (bottom) [14]. Dimensions are given in mm.

where photons can interact with the diaphragm material. The optimal diaphragm thickness is slightly dependent on the air path length of the FAC. For a FAC with an air path length of 40 mm, an optimal diaphragm thickness of 0.8 mm was determined, while for a FAC with an air path length of 100 mm, a value of 1 mm was determined. This shows that the optimal dimension for a cylindrical diaphragm is dependent on other design aspects of the FAC. The observed steeper decrease of k_{dia} for thicknesses greater than 0.8 mm for a FAC with an air path length of 40 mm can be attributed to the fact that this air path length is insufficient to prevent electrons produced in the diaphragm by the incident photons from reaching the collecting volume [8].

Burns and Büermann [5] also stated that a diaphragm thickness of 1 mm is sufficient to prevent transmission through the diaphragm body for a 50 kV x-ray beam. However, they did not address that increasing the diaphragm thickness beyond 1 mm can lead to a higher diaphragm correction. McEwan [4] reported that diaphragm scatter is independent of diaphragm thickness. In contrast, Burns and Kessler [6] observed discrepancies between their findings and those of McEwan, attributing these differences to variations in diaphragm thickness.

4.2. Aperture shape

Diaphragms with different aperture geometries were introduced to reduce the transmission and scattering of x-rays [5]. According to the analytic calculation method of Simons [2], the diaphragm transmission should be lower for an aperture with conical downstream edge. Burns and Kessler [6] did not find any substantial differences in k_{dia} when they altered the orientation of a diaphragm (cylindrical aperture with a conical downstream edge) in their measurements and simulations. Burns and Büermann [5] also concluded that there is no benefit in using a geometry other than the simple cylindrical aperture.

The results presented in section 3.2. and discussed in the following are valid for a FAC with 60 mm of air path length. Figure 4 shows that conical apertures with opening angles greater than 0.3° are unsuitable. The opening angle creates a sharp corner on the upstream side of the diaphragm, where the material thickness becomes thin and allows photon transmission. The larger the aperture angle, the more pronounced this issue, leading to diaphragm corrections exceeding 1% for apertures with opening angles greater than 15°.

It was found that the required diaphragm correction can be reduced with an opening angle of 0.3° compared to a cylindrical aperture. However, the observed reduction depends on the thickness of the diaphragm. When using a 10 mm diaphragm, 0.4% less diaphragm effects need to be corrected. With a 1 mm thick diaphragm, the reduction is less than 0.1%.

For opening angles of 0.3°, diaphragms with hybrid apertures require greater diaphragm correction than those with 0.3°-conical apertures of equivalent diaphragm thickness. As the aperture correction factor remains constant for larger opening angles than 0.3° with hybrid aperture shapes, they are nevertheless preferable to conical apertures. However, compared to a 1 mm diaphragm with cylindrical aperture the diaphragm correction for hybrid apertures is the same or even increased.

The improvement with a 0.3° aperture opening angle results from the x-ray beam having an incidence angle of about 0.3° at the aperture in the described setup. This minimizes the interactions with the diaphragm when the x-ray beam passes through the aperture. Changing the distance between the x-ray source and the FAC alters the beam incidence angle, making 0.3° opening angle no longer optimal.

It has been shown that angled aperture shapes can result in a marginal reduction in the diaphragm correction compared to a diaphragm with cylindrical aperture. However, these reductions are negligible given the significantly increased manufacturing complexity for precise small taper angles in tungsten plates. Resulting mechanical inaccuracies increase the uncertainty associated with k_{dia}. Moreover, the positive effect of angled apertures is limited to a certain distance from the x-ray tube. Therefore, it is not generally applicable, making the measurements less robust for variable experimental setups.

5. Conclusion

Regular dosimeter calibration ensures consistency and comparability of dosimeter measurements through traceability to a primary standard. The first step in the

development of the new PTB low-energy x-ray primary standard is the design of its geometry.

This study systematically investigated the optimal diaphragm geometry to minimize the diaphragm correction factor k_{dia} for a low-energy x-ray FAC used as primary standard for the realization of the unit of the air kerma. Monte Carlo simulations were employed to calculate the diaphragm correction factor k_{dia} for various diaphragm geometries. It was observed that k_{dia} depends on the diaphragm thickness and the aperture shape. The optimal thickness for a tungsten diaphragm is between 0.8 mm and 1 mm, depending on the air path length of the FAC. The present results clearly show that there is no reason to prefer a diaphragm geometry with a more complex aperture shape over a simple 1 mm thick diaphragm with a cylindrical aperture. Consequently, the new PTB primary standard, a FAC with an air path length of 60 mm, employs a 1 mm tungsten diaphragm with cylindrical aperture.

References

1. *Fundamental Quantities and Units for Ionizing Radiation (Revised)*, Rep. 85, ICRU, Bethesda (MD), USA, 2011.
2. H. A. B. Simons, "The Calculation of Gamma Ray Penetration of the Walls of Cylindrical and Conical Collimating Holes," *Phys. Med. Biol.*, vol. 6, no. 4, pp. 561 – 576, Apr. 1962.
   DOI: 10.1088/0031-9155/6/4/305
   PMid: 13913179
3. M. Boutillon, W. H. Henry, P. J. Lamperti, "Comparison of Exposure Standards in the 10–50 kV X-Ray Region," *Metrologia*, vol. 5, no. 1, pp. 1 – 10, Jan. 1969.
   DOI: 10.1088/0026-1394/5/1/002
4. A. C. McEwan, "Corrections for scattered photons in free-air ionisation chambers," *Phys. Med. Biol.*, vol. 27, no. 3, pp. 375 – 386, Mar. 1982.
   DOI: 10.1088/0031-9155/27/3/004
   PMid: 7071149
5. D. T. Burns, L. Büermann, "Free-air ionization chambers," *Metrologia*, vol. 46, no. 2, pp. S9 – S23, Apr. 2009.
   DOI: 10.1088/0026-1394/46/2/S02
6. D. T. Burns, C. Kessler, "Diaphragm correction factors for free-air chamber standards for air kerma in x-rays," *Phys. Med. Biol.*, vol. 54, no. 9, pp. 2737 – 2745, May 2009.
   DOI: 10.1088/0031-9155/54/9/009
   PMid: 19351980
7. T. Kurosawa, N. Takata, N. Saito, "Effect of the diaphragm of free-air ionisation chamber for X-ray air-kerma measurements," *Radiat. Prot. Dosim.*, vol. 146, no. 1 – 3, pp. 195 – 197, Jul. 2011.
   DOI: 10.1093/rpd/ncr146
   PMid: 21498414
8. J. Gschweng, S. Pojtinger, "Free-air ionization chambers for the measurement of air kerma in low-energy x-rays – optimum air path length and the limitations of averaging monoenergetic correction factors," *Metrologia*, vol. 62, no. 2, 025013, Apr. 2025.
   DOI: 10.1088/1681-7575/adc39d
9. I. Kawrakow, D. W. O. Rogers, *The EGSnrc Code System: Monte Carlo Simulation of Electron and Photon Transport*, Rep. PIRS-701, NRCC, Ottawa, Canada, 2000.
   Retrieved from: https://nrc-cnrc.github.io/EGSnrc/doc/pirs701-egsnrc.pdf
   Retrieved on: Apr. 04, 2025
10. E. Mainegra-Hing, N. Reynaert, I. Kawrakow, "Novel approach for the Monte Carlo calculation of free-air chamber correction factors," *Med. Phys.*, vol. 35, no. 8, pp. 3650 – 3660, Aug. 2008.
    DOI: 10.1118/1.2955551
    PMid: 18777925
11. I. Sechopoulos et al., "RECORDS: improved Reporting of montE CarlO RaDiation transport Studies: Report of the AAPM Research Committee Task Group 268," *Med. Phys.*, vol. 45, no. 1, pp. e1 – e5, Jan. 2018.
    DOI: 10.1002/mp.12702
    PMid: 29178605
12. I. Kawrakow, M. Fippel, "Investigation of variance reduction techniques for Monte Carlo photon dose calculation using XVMC," *Phys. Med. Biol.*, vol. 45, no. 8, pp. 2163 – 2183, Aug. 2000.
    DOI: 10.1088/0031-9155/45/8/308
    PMid: 10958187
13. L. Büermann, *The PTB free-air ionization chambers*, Physikalisch-Technische Bundesanstalt, Braunschweig, Germany, 2021.
    DOI: 10.7795/120.20220324
14. C. Kessler, D. T. Burns, P. Roger, *Establishment of reference radiation qualities for mammography*, Rep. 2010/01, BIPM, Paris, France, 2010.
    Retrieved from: https://www.bipm.org/documents/20126/27085544/bipm+publication-ID-2090.pdf/246a5298-8b17-cbb1-bd96-38da3bc7da2a?version=1.3&download=false
    Retrieved on: Apr. 04, 2025

Eidesstattliche Erklärung

Ich erkläre: Ich habe die vorgelegte Dissertation selbstständig und ohne unerlaubte fremde Hilfe und nur mit den Hilfen angefertigt, die ich in der Dissertation angegeben habe. Alle Textstellen, die wörtlich oder sinngemäß aus veröffentlichten Schriften entnommen sind, und alle Angaben, die auf mündlichen Auskünften beruhen, sind als solche kenntlich gemacht. Ich stimme einer evtl. Überprüfung meiner Dissertation durch eine Antiplagiat-Software zu. Bei den von mir durchgeführten und in der Dissertation erwähnten Untersuchungen habe ich die Grundsätze guter wissenschaftlicher Praxis, wie sie in der entsprechenden Satzung der federführenden Hochschule niedergelegt sind und die mir ausgehändigt wurde, eingehalten.

X 

Jessica Gschweng